Controlling the distribution and the structural properties of positioned quantum dots

Zur Erlangung des akademischen Grades eines
DOKTORS DER NATURWISSENSCHAFTEN
von der Fakultät für Physik des Karlsruher Instituts für Technologie

genehmigte

DISSERTATION

von

Dipl.-Phys. Mathieu Frédéric Helfrich
aus Kirchheimbolanden

Tag der mündlichen Prüfung: 13.07.2012

Referent:	Prof. Dr. Heinz Kalt
Korreferent:	Prof. Dr. Daniel M. Schaadt

Publications

Parts of this work have been published, have been accepted for publication or have been submitted for publication:

Refereed journal articles

1. **Growth and characterization of site-selective quantum dots**
   M. Helfrich, P. Schroth, D. Grigoriev, S. Lazarev, T. Slobodskyy, T. Baumbach, D. M. Schaadt
   Submitted to *Phys. Status Solidi A*

   Invited feature article (topical review)

2. **Controlling structural properties of positioned quantum dots**
   M. Helfrich, B. Terhalle, Y. Ekinci, D. M. Schaadt
   Submitted to *J. Cryst. Growth*

3. **Growth and annealing of InAs quantum dots on pre-structured GaAs substrates**
   M. Helfrich, D. Z. Hu, J. Hendrickson, M. Gehl, D. Rülke, R. Gröger, D. Litvinov, S. Linden, M. Wegener, D. Gerthsen, T. Schimmel, M. Hetterich, H. Kalt, G. Khitrova, H. M. Gibbs, and D. M. Schaadt
   J. Cryst. Growth **323**, 187 (2011)

4. **Investigation of pre-structured GaAs surface for subsequent site-selective InAs QD growth**
   M. Helfrich, R. Gröger, A. Förste, D. Litvinov, D. Gerthsen, T. Schimmel, and D. M. Schaadt
   Nanoscale Res. Lett. **6**, 211 (2011)

5. **InAs quantum dot site selective growth on GaAs substrates**
   J. Hendrickson, M. Helfrich, M. Gehl, D. Z. Hu, D. Schaadt, S. Linden, M. Wegener, B. Richards, H. Gibbs, and G. Khitrova
   Phys. Status Solidi C **8(4)**, 1242 (2011)

Non-refereed articles

1. **Thermal annealing of InAs quantum dots on patterned GaAs substrates**
   M. Helfrich, J. Hendrickson, D. Rülke, H. Kalt, M. Hetterich, G. Khitrova, H. Gibbs, S. Linden, M. Wegener, D. Z. Hu, and D. M. Schaadt
   AIP Conf. Proc. **1399**, 217 (2011)

Presentations at conferences and workshops

1. **Growth and characterization of site-selective quantum dots**
   M. Helfrich, P. Schroth, S. Lazarev, D. Grigoriev, T. Slobodskyy, T. Baumbach, D.

M. Schaadt
Frühjahrstagung der DPG, Berlin (Germany), **HL 14.2**, March 2012

Invited, Focus session "Site-selective Growth of single Quantum Dots"

2. **Annealing effects on site-selective InAs quantum dots**
M. Helfrich, J. Hendrickson, M. Gehl, D. Rülke, D. Z. Hu, M. Hetterich, S. Linden, M. Wegener, H. Kalt, G. Khitrova, H. M. Gibbs, and D. M. Schaadt
Euro-MBE 2011, L'Alpe d'Huez (France), March 2011

3. **Effects of in-situ annealing on site-selective InAs quantum dots grown on pre-structured GaAs substrates**
M. Helfrich, D. Rülke, J. Hendrickson, M. Gehl, D. Z. Hu, M. Hetterich, S. Linden, M. Wegener, G. Khitrova, H. M. Gibbs, H. Kalt, and D. M. Schaadt
Frühjahrstagung der DPG, Dresden (Germany), **HL 86.1**, March 2011

4. **Growth and annealing of InAs quantum dots on pre-structured GaAs substrates**
M. Helfrich, D. Z. Hu, J. Hendrickson, M. Gehl, D. Rülke, R. Gröger, D. Litvinov, S. Linden, M. Wegener, D. Gerthsen, T. Schimmel, M. Hetterich, H. Kalt, G. Khitrova, H. M. Gibbs, and D. M. Schaadt
16th International Conference on Molecular Beam Epitaxy (MBE 2010), Berlin (Germany), August 2010

5. **InAs quantum dot site selective growth on GaAs substrates**
J. Hendrickson, M. Gehl, M. Helfrich, D. Z. Hu, D. M. Schaadt, S. Linden, M. Wegener, H. M. Gibbs, and G. Khitrova
10th International Workshop on Nonlinear Optics and Excitation Kinetics in Semiconductors (NOEKS 10), Paderborn (Germany), August 2010

6. **Thermal annealing of InAs quantum dots on patterned GaAs substrates**
M. Helfrich, J. Hendrickson, D. Rülke, H. Kalt, M. Hetterich, G. Khitrova, H. Gibbs, S. Linden, M. Wegener, D. Z. Hu, and D. M. Schaadt
30th International Conference on the Physics of Semiconductors (ICPS 2010), Seoul (South Korea), July 2010

7. **Investigation of pre-structured GaAs surface for subsequent site-selective InAs QD growth**
M. Helfrich, R. Gröger, A. Förste, D. Litvinov, D. Gerthsen, T. Schimmel, and D. M. Schaadt
International Conference on Superlattices, Nanostructures and Nanodevices (ICSNN-2010), Beijing (China), July 2010

8. **Site-selective molecular beam epitaxial growth of InAs quantum dots on pre-patterned GaAs substrates**
M. Helfrich, D. Z. Hu, J. Hendrickson, D. Rülke, P. Aßhoff, H. Kalt, M. Hetterich, G. Khitrova, H. M. Gibbs, and D. M. Schaadt
Quantum Dot 2010, Nottingham (United Kingdom), April 2010

9. **Site-selective molecular beam epitaxial growth of InAs quantum dots on pre-patterned GaAs substrates**
M. Helfrich, D. Z. Hu, J. Hendrickson, D. Rülke, P. Aßhoff, H. Kalt, M. Hetterich,

G. Khitrova, H. M. Gibbs, and D. M. Schaadt
Frühjahrstagung der DPG, Regensburg (Germany), **HL 52.10**, March 2010

List of Abbreviations

AFM	Atomic force microscopy
As	Arsenic
Au	Gold
BEP	Beam equivalent pressure
BL	Buffer layer
CCD	Charge coupled device
CL	Capping layer
DE	Dry etching
DUV	Deep ultraviolet
EUV	Extreme ultraviolet
FT	*Fourier* transformation
FWHM	Full width at half maximum
Ga	Gallium
GaAs	Gallium arsenide
GID	Grazing incidence diffraction
GISAXS	Grazing incidence small angle X-ray scattering
GR	Growth rate
H	Atomic hydrogen
HCl	Hydrochloric acid
He	Helium
HRTEM	High resolution transmission electron microscopy
HRXRD	High resolution X-ray diffraction
ICP	Inductively coupled plasma
In	Indium
InAs	Indium arsenide
IPA	Isopropyl alcohol

LFM	Lateral force mode
LN2	Liquid nitrogen
MA	Methacrylic acid
MBE	Molecular beam epitaxy
Mo	Molybdenum
NJP	Nano-jet probe
NMP	N-methyl-2-pyrroldione
O_2	Molecular oxygen
O_3	Ozone
pBN	Pyrolytic boron nitride
PID	Partial-integral-derivative
PL	Photoluminescence
PMMA	Polymethyl methacrylate
RF	Radio frequency
RHEED	Reflection high energy electron diffraction
RIE	Reactive ion etching
RMS	Root mean square
RTA	Rapid thermal annealing
SAE	Selective area epitaxy
SAG	Selective area growth
SEM	Scanning electron microscope
TCE	Trichlorethylene
TEM	Transmission electron microscopy
Ti	Titanium
TMP	Turbo molecular pump
UHV	Ultra high vacuum
UV	Ultraviolet
WCE	Wet chemical etching

Contents

1 Introduction

Semiconductor devices form the basis for the technological progress of our information society. Modern information and telecommunication technologies have gained fundamental importance in daily life. The continuous demand for increased performance of data storage and transfer is reflected by the exponential law that *Gordon Moore* formulated in 1965, according to which the number of components in an integrated circuit would double every year [1]. In order to pursue this development, the size of the components was continuously decreased. Hence, the unique success story of semiconductor physics and technology relies on the ability to highly integrate micro- and nanometer sized functional units on a single chip [2].

The development predicted by *Moore* endures until today but growth in performance has slowed down, since functional units approach sizes in the nanometer range which impose a physical limit on the functionality. In order to bypass these limitations novel semiconductor structures were investigated, with the aim to exploit the quantum mechanical effects that arise at the nanometer scale.

The advent of a new class of materials, namely semiconductor nanostructures, was related to studies of *Cho* and *Arthur* in the late 1960s. They demonstrated the ability to control the fabrication process of crystalline materials on atomic scale when they first successfully used a molecular-beam apparatus to crystallize and investigate thin GaAs layers [3]. In the following years, the realization of quantum wells (2D), in which the free motion of charge carriers is restricted to two of the three spatial dimensions, marked the beginning of a new era of research on low dimensional electronic structures [4]. In 1982, *Arakawa* and *Sakaaki* suggested that a further reduction in the dimensionality caused by structuring the active medium in quantum wires (1D) or in quantum dots (0D) would generate a new technological breakthrough [5]. This insight led to intensive research in the field of semiconductor nanostructures and quantum dots soon received increased attention because of their unique properties.

In semiconductor quantum dots (QDs), electrons and holes are three-dimensionally confined into nanometer-scale semiconductor crystals, hence the term zero-dimensional [6]. As a result, the electronic density of states becomes delta-function-like, which means that QDs exhibit discrete energy levels like atoms. Semiconductor QDs can be fabricated by epitaxial techniques such as molecular beam epitaxy (MBE) by embedding nanometer sized islands of a low bandgap semiconductor material in a host matrix of a higher bandgap semiconductor material. Epitaxial QDs have several advantages compared to atoms. Unlike in atoms, the emission properties of QDs can be adjusted by changing their structure [7]. Since the position of the QDs is fixed in the host matrix, the matrix including the QD can be further processed and functionalized. This has allowed to turn QDs into functional units in devices like light emitting diodes [8, 9] or lasers [8, 10]. Further QD properties have been investigated in the last decade with respect to device applications with novel functionalities. QDs can, for example, confine electrons and holes for some time which makes them promising candidates for storage devices [11]. The QD's ability to emit single photons makes it a non-classical light source [12]. Single photon emission from a QD can be triggered electrically and optically. QDs were also shown to generate entangled photon pairs which might be of interest for secure quantum communication [13]. The possibility to fabricate resonator systems such as micro-pillar cavities [14] or photonic crystal cavities [15] around the QDs allowed for the study of cavity quantum electrodynamical effects. The weak and strong coupling of optical resonator modes to excitonic states of the QD were progressively investigated [16, 15, 17, 18, 19]. Thus, the potential of QDs for quantum information applications is well described.

Different material systems have been investigated among which In(Ga)As/GaAs, where In(Ga)As QDs are grown on a GaAs substrate, has been most widely studied. Due to its wide range of emission wavelengths this system is a promising candidate for telecommunication applications with the important wavelengths of zero dispersion and lowest absorption in optical fibers, i.e. 1.3 µm and 1.55 µm, being accessible [20].

A fundamental problem with respect to functionalization of QDs for applications is related to their fabrication. The formation of epitaxial QDs in MBE is based on the finite lattice mismatch between the QD material and the host material. Islands will form on the host substrate when the amount of the deposited QD material exceeds a critical thickness. Covering these islands with the host material finally completes the QD structure. This self-assembly process is random in nature so that the position of individual QDs cannot be controlled. But then, a key requirement for device integration is a deterministic positioning of QDs. This problem has been addressed during the last decade and different techniques have been employed to guide the nucleation of epitaxial QDs.

Self-alignment mechanisms such as growth on vicinal surfaces have been used to create ordered QD structures [21]. However, ordering mainly occurs on a short range and control of absolute QD position is thus limited. As a consequence, methods to align QDs through external forces have been developed. The most versatile and therefore most advanced approach uses lithographically defined holes to guide the nucleation of QDs. Electron beam lithography (EBL) is routinely used to fabricate nanometer sized holes on the substrate surface [22, 23]. The holes alter the surface chemical potential and lead to a locally increased growth rate which then allows for selective QD nucleation [24]. Size, depth and shape of the holes can be varied over a wide range, thus offering the possibility to control some of the QD properties as well as their distribution. For instance the number of QDs per hole increases with the size of the hole [25].

In general, obtaining the right conditions for a particular set of QDs is a rather tedious work. The influence of different growth parameters and geometrical features of the holes and the pattern on the QD formation process were not completely revealed. Furthermore, the possibility to control and adjust QD properties such as size, shape or site occupation on a given pattern after growth was not emphasized. It is known that at lower temperatures QDs tend to ripen whereas they dissolve at higher temperatures [26, 27]. *In situ* annealing experiments with self-assembled QDs have confirmed the power of this technique to alter properties such as QD size, shape and ordering [28, 29, 30]. The fact that QDs undergo morphological changes during annealing remained, however, unattended with respect to positioned QDs.

The aim of this work was to establish a reproducible process for the fabrication of site-selective QDs, to identify and investigate influential factors in the formation of positioned QDs, to investigate the structural properties of positioned QDs and to find possible mechanisms to control these properties as well as the QD distribution.

Outline

This thesis is divided into five main parts. Chapter 2 is concerned with approaches to QD positioning and starts off with an introduction to the basic properties of QDs. This is followed by a description of the particular InAs/GaAs system in use and the mechanism that leads to the formation of InAs islands on GaAs substrates. Different mechanisms to guide the QD formation are introduced and the role of surface deformation in a local increase of the growth rate is explained from a theoretical point of view.

General aspects of the sample preparation process are emphasized in chapter 3. The principle of electron beam lithography is explained and the most important exposure parameters are given. The limitations of wet chemical etching are demonstrated and an alternative way to increase the structural anisotropy of the final structure is proposed. Finally, the growth of InAs islands by molecular beam epitaxy and the relevant growth parameters are discussed at the end of this chapter.

During the course of this work the role of the sample cleaning after definition of the nanometer sized holes was revealed with respect to the attempt to deterministically position QDs. This important aspect is addressed in chapter 4. An improved cleaning procedure by using a UV/ozone process is suggested and tested. Furthermore, the deoxidation process and its consequences for the site-selective QD growth are highlighted.

Chapter 5 focuses on the site-selective growth of QDs. General features of site-selective QDs are described and a statistical investigation of the optical properties is presented. The influence of the hole structure and the growth parameters on the structural properties and the distribution of positioned QDs is analyzed and discussed.

The prospect of *in situ* annealing to control various parameters in site-selective growth is considered in chapter 6. A qualitative description of the evolution of positioned QDs during *in situ* annealing is followed by a quantitative analysis of the changes in QD distribution and size. Finally, the assessment of large ordered QD arrays by X-ray diffraction measurements is examined.

To conclude this work, a summary of the major results is given in chapter 7 and based on the experimental findings, a possible path to proceed with this research is proposed in the outlook.

2 Approaches to quantum dot positioning

The desire to fabricate semiconductor quantum dots with known positions has been motivated in the first chapter. After the fabrication of quantum dots has been mastered, research moved on to control their location. This chapter is devoted to these two main aspects, i.e., the growth of quantum dots and their positioning. A short introduction to the electronic properties of quantum dots is given in section 2.1, outlining their unique properties. Then, the formation of quantum dots based on the InAs/GaAs system is described in section 2.2. Finally, different approaches to guide the nucleation of quantum dots and therefore determine their position are introduced and discussed in section 2.3.

2.1 Definition of a quantum dot in terms of electronic properties

The term "quantum dot" (QD) refers to the nature of systems whose physical properties are governed by quantum mechanical effects. This is the case when the size of a physical object is decreased below a certain limit, usually ranging about 100 nm. Second, the number of spatial dimensions in which the size is decreased plays an important role. This is reflected by the meaning of "dot" which, mathematically speaking, is a zero-dimensional object. Hence, the size must be reduced in all three spatial dimensions below the quantum limit in order for the object to be called a quantum dot.

Conceptually, the above definition is related to the electronic properties of a nm sized object (nano object). Electrons are point like particles but a characteristic wavelength λ can be attributed to them, the so called *de Broglie* wavelength which emerges from the wave-particle duality in quantum mechanics. It is given by

$$\lambda_{\text{de Broglie}} = \frac{h}{p} = \frac{h}{\sqrt{3m^* k_{\mathrm{B}} T}} \quad , \tag{2.1}$$

where h denotes the *Planck* constant, p the momentum, m^* the effective mass, k_{B} the *Boltzmann* constant and T the temperature. If the electron resides inside a potential well whose size is of the same order as $\lambda_{\text{de Broglie}}$, quantization effects will occur because the degrees of freedom of the electron's momentum are reduced. Most prominently, its energy eigenvalues will be discrete. This situation is illustrated in figure 2.1 (a) in one dimension with the confinement potential being created by using two materials of different bandgap. The degree of quantization is directly related to the number of spatial dimensions which are reduced to the electron's "size". Thus, electrons in zero-dimensional QDs experience fully quantized energy eigenvalues. This is analogous to the known quantum mechanical textbook problem of a "particle in a box" [31]. For electrons in a semiconductor QD, the quasi continuous energy levels of the conduction band collapse into discrete energy levels due to the three-dimensional confinement - which is why QDs are also called artificial atoms. A similar derivation can be applied for holes in the valence band if the corresponding effective hole mass is used. This leads to discrete energy levels as for the electron in the conduction band. In general, the energy eigenvalues are

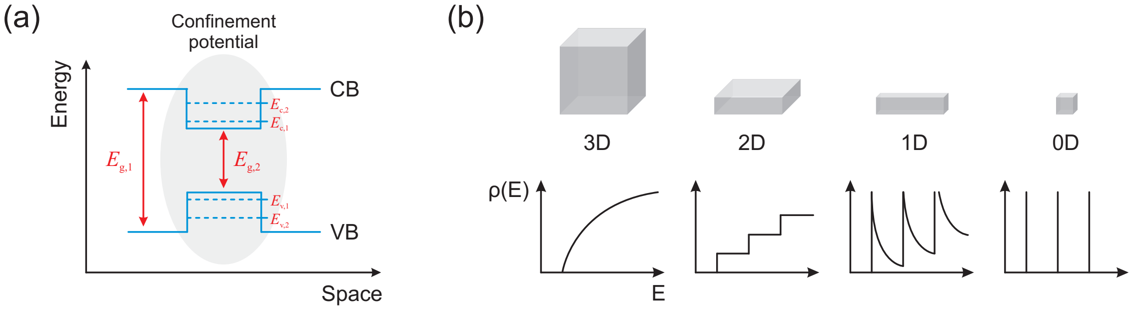

Figure 2.1 (a) Formation of a confinement potential (gray region) in one dimension by placing a lower bandgap material inside a higher bandgap material, i.e. $E_{\mathrm{g},1} > E_{\mathrm{g},2}$. Discrete energy levels ($E_{\mathrm{c},1}, E_{\mathrm{v},1}, \cdots$) emerge if the confinement region is smaller than the electron *de Broglie* wavelength. (b) Illustration of the density of states $\rho(E)$ for a bulk semiconductor (3D), a quantum well (2D), a quantum wire (1D) and a quantum dot (0D).

$$E_{n_x,n_y,n_z} = \frac{\hbar^2}{2m^*}\left(k_x^2 + k_y^2 + k_z^2\right) \tag{2.2}$$

$$k_x = \frac{2\pi n_x}{l_x} \quad ; \quad k_y = \frac{2\pi n_y}{l_y} \quad ; \quad k_z = \frac{2\pi n_z}{l_z}$$

with l_x, l_y, l_z being the lengths of the QD in the respective dimensions and n_x, n_y, n_z being positive integers. The effective mass m^* depends on the kind of particle (electron or hole) that is considered. Since a free electron gas is assumed, the energy dispersion relation is parabolic which is true for electrons (holes) in the conduction band (valence band) near the Γ-point. Most energy eigenstates are degenerate. Because of discrete energy eigenvalues, the density of states is then expressed as

$$\frac{\mathrm{d}N}{\mathrm{d}E} = \rho(E) = 2 \sum_{n_x,n_y,n_z} \delta(E - E_{n_x,n_y,n_z}) \quad . \tag{2.3}$$

The factor of two arises from spin degeneracy. Figure 2.1 (b) illustrates the density of states of a QD and of higher dimensional nanostructures. The number of states that a QD can develop depends on its size. If the dot gets smaller, i.e. the potential well is squeezed, the spacing between emerging energy levels increases. Therefore, larger QDs will contain more energy levels than smaller ones, see figure 2.2. The minimum diameter for a QD to include at least one energy level for a confined electron can be calculated from

$$d_{\min} = \frac{\pi\hbar}{\sqrt{2m^*\Delta E_\mathrm{c}}} \tag{2.4}$$

where ΔE_c denotes the conduction band offset.
Hole states in the valence band differ from electron states in the current band. The valence band of a semiconductor is formed by p-type atomic orbitals in contrast to the s-type character of the conduction band, see figure 2.3 (a). Therefore, an angular momentum with quantum number $\ell = 1$ can be associated to the valence band states. Since the angular momentum is quantized, the projection ℓ_z of the corresponding vector operator $\boldsymbol{\ell}$ onto a given axis (here z-axis) yields the eigenvalues $+\hbar$, 0, $-\hbar$ which are represented by the magnetic quantum number $m_\ell = +1, 0, -1$. If a charge carrier possessing a spin is

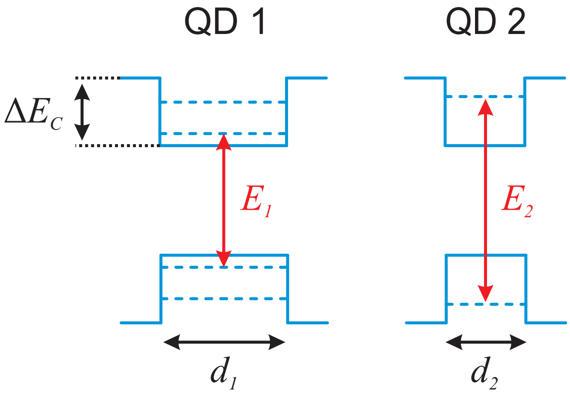

Figure 2.2 Dependence of energy levels on QD size. Larger QDs ($d_1 > d_2$) contain more energy levels with smaller spacings. Therefore, the difference between energy levels is higher in smaller QDs ($E_2 > E_1$).

found in such a state it experiences spin-orbit coupling, a self-interaction of the magnetic field (caused by charge and angular momentum) with the spin. Angular momenta are additive and thus, the total angular momentum is given by $\boldsymbol{j} = \boldsymbol{\ell} + \boldsymbol{s}$. The orientation of $\boldsymbol{\ell}$ and $\boldsymbol{s}$, or rather their projection onto a given axis, can be either parallel or anti-parallel. This leads to a fine-structure splitting of the energy states. The total angular momentum therefore takes the values $j = 3/2$ or $1/2$, resulting in six possible states of which three are energetically different (two opposite spin orientations per state). As a result the valence band splits into three subbands which are identified as heavy hole (hh), light hole (lh) and spin-orbit split-off band (so), see figure 2.3 (b). The states and their corresponding subbands are listed below.

$\lvert \boldsymbol{j}, j_z\rangle = \left\lvert \frac{3}{2}, \pm\frac{3}{2}\right\rangle$	heavy hole (hh) subband
$\lvert \boldsymbol{j}, j_z\rangle = \left\lvert \frac{3}{2}, \pm\frac{1}{2}\right\rangle$	light hole (hh) subband
$\lvert \boldsymbol{j}, j_z\rangle = \left\lvert \frac{1}{2}, \pm\frac{1}{2}\right\rangle$	spin-orbit split-off (so) subband

The terms "light" and "heavy" refer to the effective mass of holes in these subbands which have a different curvature. In general, the (lh) and (hh) subbands are degenerate around the Γ-point. However, this degeneracy is lifted for strained semiconductors. The (so) subband is offset by the split-off energy Δ_{so}.

If an electron and a hole are both confined in a QD they can create a bound state called exciton (X^0). Such a bound state is similar to the hydrogen atom with the proton being replaced by the valence band hole. Therefore, the binding energy can easily be calculated as

$$E_{\mathrm{bind}} = -\frac{\mu^*}{\epsilon_{\mathrm{r}}^2 m_{\mathrm{e}}}\mathrm{Ry} \tag{2.5}$$

with μ^* being the reduced effective mass of the electron and hole ($1/\mu^* = 1/m_{\mathrm{e}}^* + 1/m_{\mathrm{h}}^*$), ϵ_{r} being the static dielectric constant, m_{e} being the electron rest mass and Ry ($= 13.6\,\mathrm{eV}$) being the *Rydberg* energy. As for the hydrogen atom, an excitonic *Bohr* radius can be defined as $a_{\mathrm{X}^0} = a_0 \cdot \epsilon_{\mathrm{r}} m_{\mathrm{e}}/\mu^*$ with the *Bohr* radius a_0 ($= 0.053\,\mathrm{nm}$).

After a limited lifetime τ, excitons recombine and radiate a photon if this is allowed by angular momentum conservation. The recombination energy is lower than the energy

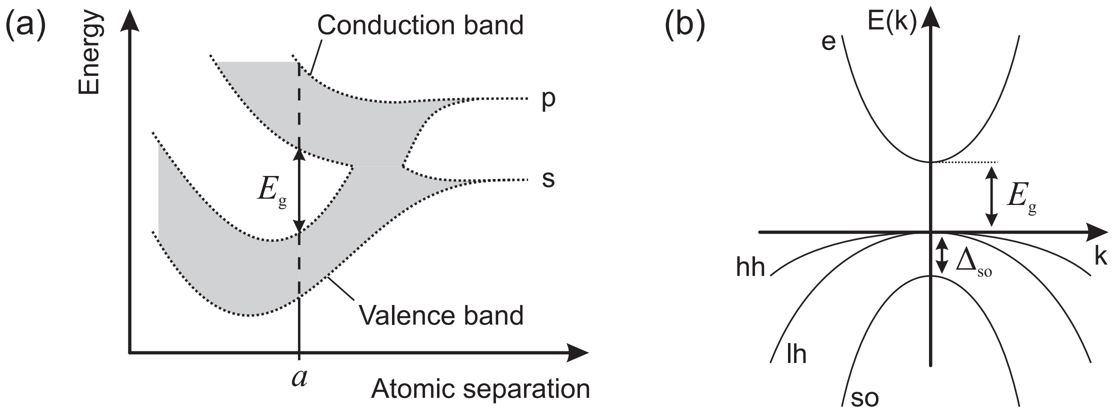

Figure 2.3 (a) Illustration of transition from discrete atomic energy levels (s- and p-level) into continuous energy bands in a semiconductor crystal of zincblende type. An energy gap E_g is formed at the lattice constant a. (b) Band structure for a direct bandgap semiconductor with the four most important bands - from top: conduction (e), heavy hole (hh), light hole (lh) and spin-orbit split-off (so) band.

difference of the unbound charge carriers in the QD due to the exciton binding energy. In a simple approximation, the recombination energy for the first electron and hole levels ($n_x = n_y = n_z = 1$) of a symmetric QD ($l_x = l_y = l_z = l$) can be expressed as

$$\begin{aligned} E_{\mathrm{X}^0} &= E_\mathrm{g} + E_\mathrm{conf} + E_\mathrm{bind} \\ &= E_\mathrm{g} + \frac{6\pi^2\hbar^2}{l^2}\left(\frac{1}{m_\mathrm{e}^*} + \frac{1}{m_\mathrm{h}^*}\right) - \frac{\mu^*}{\epsilon_\mathrm{r}^2 m_\mathrm{e}}\mathrm{Ry} \end{aligned} \tag{2.6}$$

where E_g denotes the band gap energy.

Excitons can be generated by photon absorption. If the photon energy $\hbar\omega$ is larger than $E_\mathrm{g}+E_\mathrm{conf}$ of the QD, an electron from a valence band state can be excited into a state in the conduction band leaving behind a hole in the valence band. Due to the local confinement in the QD it is very likely that the hole and the electron bind to form an exciton. In such a case the radiative excitonic recombination is called photoluminescence (PL) due to the photoexcitation process. If all QDs were of the same size, the PL of the QDs would be a single sharp peak only broadened by the natural linewidth which is related to the uncertainty principle $\Delta E \Delta\tau \geq \hbar$ where ΔE represents the linewidth and $\Delta\tau$ the lifetime. Such a peak would exhibit a *Lorentz*ian profile. This is an ideal case and in reality a distribution of QD sizes is found. Therefore, the luminescence of a QD ensemble will experience inhomogeneous broadening expressed by a *Gauss*ian profile of the form

$$P_n(E, E_n, \sigma_n) = \frac{1}{\sigma_n\sqrt{2\pi}} \exp\left[-\frac{(E-E_n)^2}{2\sigma_n^2}\right] \tag{2.7}$$

where σ_n is the full width at half maximum (FWHM) of the n-th QD excitonic recombination and E_n is the transition energy between the energy levels [32]. As it is desired to obtain QDs with little broadening this work aims at finding ways to reduce the size distribution of QDs as much as possible.

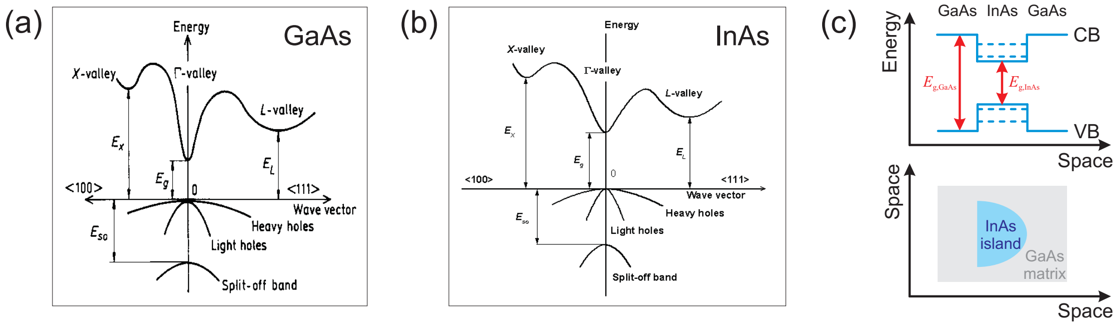

Figure 2.4 Band structure of GaAs (a) and InAs (b) at the Γ-point [33]. Type 1 band alignment for InAs islands in a GaAs matrix (c).

2.2 Indium arsenide islands as quantum dots

There are, in general, two ways to realize a three-dimensional confinement potential in this context. This can either be achieved by placing a cluster of low bandgap material inside a higher bandgap material or by using adequate gates on top of a semiconductor to define a local electrostatic confinement potential. In this work, quantum dots will be referred to as being formed according to the first method.

2.2.1 Basic electronic properties

The QDs are realized by the formation of nm sized InAs islands[1] on a GaAs substrate through a self-organization process which will be described in more detail in section 2.2.2. These islands can then be covered with GaAs to fully enclose them in a GaAs matrix. The compound semiconductors InAs and GaAs have different direct bandgaps (at the Γ-point) and the bands align in a type 1 heterojunction, as illustrated in figure 2.4. This way of alignment then allows for charge carriers, both holes and electrons, to be confined in the region of lower bandgap. The conduction band offset for InAs/GaAs QDs is $E_c = 340 \pm 30\,\mathrm{meV}$ [34].
Some basic structural and electronic parameters of GaAs and InAs are summarized in table 2.1. With these it is possible to estimate the diameter of an InAs QD which contains at least one electron energy level. Using equation (2.4) and taking into account the conduction band offset, the minimum diameter is $d_{\mathrm{min}} = 6.9 \pm 0.3\,\mathrm{nm}$. This is a lower limit for the size of InAs QDs to confine electrons. Equation (2.5) is used to calculate the exciton binding energy in an InAs QD and yields $E_{\mathrm{bind}} = 1.4\,\mathrm{meV}$. This value is rather low compared to the excitonic recombination energy which is expected between $E_{\mathrm{g,InAs}}$ and $E_{\mathrm{g,GaAs}}$. Short exciton lifetimes in InAs QDs of about 1 ns are in agreement with the weak binding energy [37]. Not only the size of the InAs island will finally determine the energy of the discrete states but also its composition. The InAs island is embedded in a GaAs matrix so that interdiffussion of the metal atoms between island and matrix is assumed. This is justified by the fact that the fabrication process of the InAs islands takes place at high temperatures. The interdiffusion of In and Ga atoms leads to a continuous band transition at the island matrix interface in contrast to the idealized sharp band alignment of the sketch in figure 2.4. Depending on the degree of interdiffusion the value of the InAs bandgap will change towards the GaAs bandgap. It is also possible to intentionally

---

[1] Please note that the terms “quantum dot” and “island” will be used interchangeably throughout this work. The islands considered are small enough to ensure quantum confinement.

Parameter	Symbol	Unit	GaAs	InAs
Crystal structure			Zinc blende	Zinc blende
Lattice constant	a	Å	5.653	6.058
Elastic constants	C_{11}	10^{11} dyn/cm^2	11.9	8.34
	C_{12}	10^{11} dyn/cm^2	5.34	4.54
	C_{44}	10^{11} dyn/cm^2	5.96	3.95
Atomic volume	Ω	cm^3/mol	11.8 (Ga)	15.7 (In)
Surface energy, (100) α(2x4)	γ	meV/Å^2	65	48
Bandgap at Γ-point (300 K)	E_g	eV	1.42	0.35
(10 K)		eV	1.52	0.41
Spin-orbit splitting	Δ_{so}	eV	0.34	0.41
Effective mass	m_e^*	m_e	0.063	0.023
	m_hh^*	m_e	0.51	0.41
	m_lh^*	m_e	0.082	0.026
	m_so^*	m_e	0.15	0.16
Electron *de Broglie* wavelength	λ_e	nm	24	40
Dielectric constant (static)	ϵ_r		12.9	15.2
Electron-hole reduced mass	μ^*	m_e	0.056	0.022
Exciton binding energy	E_bind	meV	4.6	1.3
Excitonic *Bohr* radius	a_{X^0}	nm	12.2	36.9

Table 2.1 Basic structural and electronic parameters of GaAs and InAs. If not otherwise stated the values are given at $T = 300\,\mathrm{K}$. The masses are given in multiples of the electron rest mass $m_\mathrm{e} = 9.11 \times 10^{-31}$ kg. The data is taken from [33, 35, 36].

enlarge the InAs bandgap by providing Ga atoms during island fabrication which results in $\mathrm{In_{1\text{-}x}Ga_xAs}$ islands that act as QDs. Thus, the amount x of added Ga can be used to tune the optical properties of the QD. A continuous transition between the InAs and GaAs bandgaps is possible, as depicted in figure 2.5. As a reference, AlAs is also included in the diagram since it is often found in combination with the given compound semiconductors in devices. The empirical *Vegard*'s law is used to calculate the bandgap transitions between the three materials [38]. Looking at the diagram it is apparent that AlAs and GaAs have almost the same lattice constant, whereas the lattice constants of GaAs and InAs differ quite a lot. That is the key feature in the island formation mechanism which will be described in the following section.

2.2.2 Lattice mismatch and island formation

So far it was shown that QDs can be realized by InAs clusters (or better islands) inside a GaAs matrix because of the different bandgaps and the proper band alignment. The way in which InAs islands can be formed inside the GaAs matrix is considered next. GaAs and InAs both crystallize in the zinc blende structure. This is important for the epitaxial connection between the GaAs substrate and the InAs island, which is essential for a proper band alignment. Epitaxy is referred to as growth of crystalline layers on monocrystalline bulk material where the grown layer takes over the crystal structure of the material underneath. Therefore, it should be possible to deposit InAs on GaAs while maintaining the crystal zinc blende structure. In general, special techniques are required in order to obtain high quality crystal structures. In this work, all structures were grown by a physical vapor deposition (PVD) technique called molecular beam epitaxy (MBE).

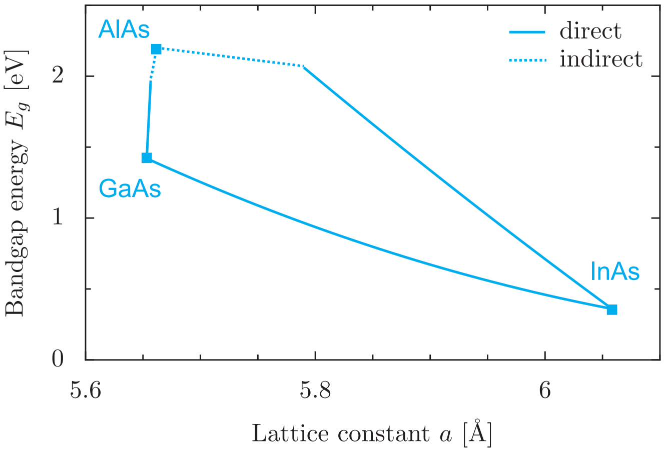

Figure 2.5 Bandgap transition between InAs, GaAs and AlAs according to *Vegard*'s law. The bandgaps are plotted as a function of the lattice constants. The diagram is taken from [39].

MBE allows for the deposition of thin semiconductor films with high precision and atomic flatness. The working principle of MBE and its application to grow high quality InAs islands for this work will be described in more detail in section 3.3.

The first criterion for high quality InAs islands on GaAs is fulfilled with both materials having the same crystal structure. The second criterion is the lattice constant. According to table 2.1 the lattice constants of InAs and GaAs differ by

$$f = \frac{a_{\mathrm{InAs}} - a_{\mathrm{GaAs}}}{a_{\mathrm{GaAs}}} \approx 7\% \tag{2.8}$$

which leads to a misfit between the two lattices. As a consequence, the deposited InAs with its larger lattice constant tries to adapt to the GaAs lattice during growth which leads to a deformation of the free InAs lattice. The InAs lattice is compressed in the surface plane and elongated perpendicular to it, or, in other words, compressive strain is accommodated in plane and tensile strain in the vertical direction, as illustrated by figure 2.6. The crystal symmetry has therefore changed from cubic to tetragonal. The deformation of the lattice can be described using the strain tensor which relates the free lattice to the deformed lattice by

$$\boldsymbol{x}' = [\mathbb{1} + \varepsilon]\boldsymbol{x} = \left[\mathbb{1} + \begin{pmatrix} \varepsilon_{xx} & \varepsilon_{xy} & \varepsilon_{xz} \\ \varepsilon_{yx} & \varepsilon_{yy} & \varepsilon_{yz} \\ \varepsilon_{zx} & \varepsilon_{zy} & \varepsilon_{zz} \end{pmatrix}\right] \boldsymbol{x} \quad . \tag{2.9}$$

The lattice distortion implies that elastic energy E_{el} is stored inside the thin film. The elastic energy is related to the deformation by $E_{\mathrm{el}} = 1/2 C_{\mathrm{ijkl}} \varepsilon_{\mathrm{ij}} \varepsilon_{\mathrm{kl}}$. C_{ijkl} is the elasticity tensor which relates stress and strain by *Hooke*'s law $\sigma_{\mathrm{ij}} = C_{\mathrm{ijkl}} \varepsilon_{\mathrm{kl}}$. The degree of strain and therefore the amount of energy per unit area stored in the film (E_{f}) depends on the difference in lattice constants but also on the film thickness h. For a cubic lattice and a $\{1\,0\,0\}$ type surface the in-plane strain is simply $\varepsilon_{\mathrm{xx}} = \varepsilon_{\mathrm{yy}} = f$ and the energy stored in the film is hence given by

$$E_{\mathrm{f}} = E_{\mathrm{el}}(f) \cdot h \quad . \tag{2.10}$$

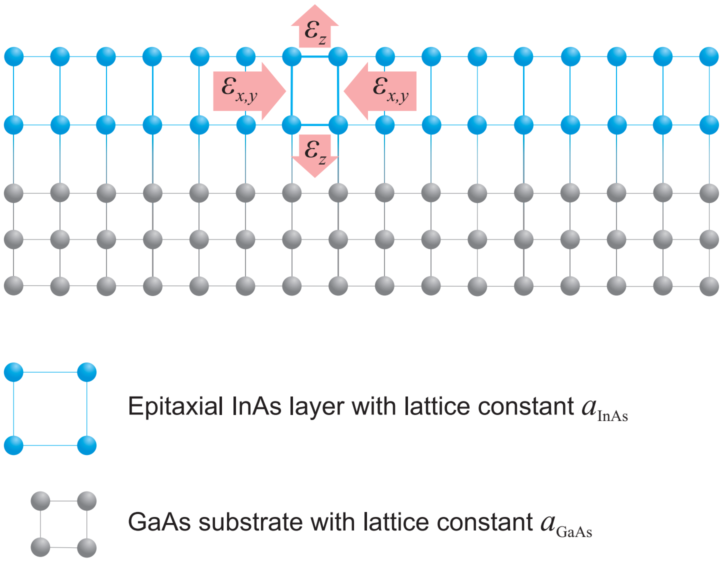

Figure 2.6 The InAs and GaAs lattices do not exactly match due to the larger InAs lattice constant. The mismatch amounts to 7%. As a result, the InAs film adapts to the GaAs lattice and therefore becomes strained.

With increasing film thickness, the accumulated strain energy E_f is eventually relieved at a critical thickness h_c. There are two mechanisms in heteroepitaxy which can contribute to strain relaxation. Either defects such as misfit dislocations can be created or the surface of the film starts to buckle which both aids relaxing the strained lattice. In the first case, the surface of the thin film remains flat but the number of dislocations increases if growth is continued. Furthermore, dislocations are dynamic and can propagate inside the film, possibly joining each other and forming dense networks. In the second case, the surface becomes rough as small InAs islands start to form through which the strain is relaxed. These islands then act as QDs.

The two mechanisms do not exclude one another and strongly depend on the growth conditions in the InAs/GaAs system. Indium rich growth conditions will favor the creation of defects whereas InAs islands will be obtained in arsenic rich conditions. Common to both mechanisms is the fact that the formation of both defects or islands costs energy. This energy has to be compared to the elastic energy stored in the film. If E_f becomes larger than the formation energy for defects or islands, strain will be relieved through these mechanisms. The critical thickness h_c defined above is different for the formation of defects and islands. At this point it is important to notice that the formation of InAs islands is a self-organization process that is driven by strain relaxation. It can be quantified by considering the energy balance for lattice deformation and island formation. With regard to applications it is important to grow defect free InAs islands since defects degrade the optical and electronic properties of the QDs.

2.3 Mechanisms to guide quantum dot nucleation

The formation of InAs islands through strain relaxation has been outlined and the basic properties of InAs QDs have been described. The inherent problem of the self-organized QD formation is its randomness with respect to QD location. So far, the InAs islands randomly nucleate on the sample surface. Although such QDs are considered as reference and exhibit very good optical properties with narrow luminescence linewidth, this approach alone cannot be used for applications which rely on a precise positioning of QDs, possibly on a large scale. This is the reason why research has lately focused on developing methods to fabricate QDs at desired locations.

2.3.1 Self-alignment and forced alignment

Although the nucleation of InAs islands on GaAs being random, there must be a factor that causes the island formation at a specific location. The substrate surface is never 100% flat since at least atomic steps are present and the atomic surface condition cannot be known to absolute precision. The local environment must play a role in the nucleation of islands which is influenced by the nature of the surface. The mechanisms that have been developed to guide the nucleation of QDs try to exploit this fact. The idea is to manipulate and control the surface in such a way that sites are created where islands will predominantly nucleate.

The mechanisms guiding the QD nucleation can be divided into two categories, lateral self-alignment and forced alignment. In the first case, self-alignment is realized by choosing appropriate growth conditions and special substrate surfaces [2]. One example is the growth on vicinal substrates in the Si/Ge system in which island formation underlies the same principles as in the InAs/GaAs system. Self-organized QD ordering is observed in a single layer of SiGe grown on a Si substrate tilted by 2° with respect to the Si(0 0 1) plane. Step bunching occurs during growth of a Si buffer layer. The resulting periodic ripple structure then guides the formation of islands during the subsequent deposition of SiGe with an alignment in straight chains [21]. Another example is the growht of QD stacks in the Ge/Si system. Several layers of randomly self-assembled SiGe islands are separated by a Si spacer layer. An enhancement of lateral ordering as well as shape and size homogeneity is observed when increasing the number of layers [40, 41]. This effect is attributed to the strain field which is exerted by the underlying islands. Common to these approaches is the fact that ordering occurs on a short range and is not applicable for absolute QD positioning.

In the second case, the surface is altered in order to force the nucleation of QDs at defined positions on a large scale. A very straightforward approach uses a mask which is placed on the GaAs substrate and which contains small holes. If InAs is then deposited islands will only form inside the apertures where a connection to the GaAs substrate is possible. The InAs deposited around the apertures on the mask material might be amorphous. After growth the mask is removed with adequate methods, e.g., selective etching of the mask material, eventually revealing islands at defined positions. This method is known as selective area epitaxy (SAE) or growth (SAG) [42, 43]. However, SAE has not yet produced coherent QDs of high optical quality for different reasons. The fabrication and removal of the mask includes steps which possibly degrade the GaAs surface which is later overgrown with InAs. Furthermore, the growth kinetics is changed due to the mask material outside the apertures.

In a different approach, indium metal droplets are deposited on a GaAs substrate through a nano-jet probe (NJP) which essentially consists of an atomic force microscopy cantilever with pyramidal tip containing an indium reservoir [44, 45]. The probe is moved to a desired location and a small metal droplet is released through an aperture at the tip apex. Afterwards, the In droplet is recrystallized to InAs by providing sufficient As. This is also referred to as droplet epitaxy. One major drawback of this technique is its low speed. Good structural and optical properties of recrystallized QDs have only partly been confirmed

recently [46, 47].
The most common approach to direct and control the self-assembly of QDs makes use of intentional deformation of the substrate surface by creating small holes. The holes can be created by various means (see chapter 5) and act as preferential sites for QD formation. In this case, the deformation of the surface is the driving force for localized island nucleation. The underlying mechanism is explained in the following.

2.3.2 Local growth rate enhancement by surface deformation

After depositing In atoms on the GaAs surface, the adatoms are not built into the crystal lattice of the underlying film right away because they are subject to diffusion and so they migrate to preferential nucleation sites [48]. The process of adatom migration on the GaAs surface is governed by the chemical potential of the surface. Altering the surface leads to a change in the chemical potential and therefore allows to influence the adatom migration and eventually the island nucleation. In this work, a modification of the surface chemical potential is achieved by creating small holes on the GaAs surface resulting in a curved surface instead of a flat film. Modeling the growth of strained films on a curved surface is very complex which is why only one-dimensional models are employed to describe the fundamental effects of surface curvature on subsequent growth. *Wang et al.* analyzed the stability of strained thin films on wavy substrates based on a model of *Srolovitz* [49]. They conclude that a critical wavelength of surface waviness exists, above which the growth of a strained film is unstable, resulting in increased undulation [2, 50]. However, this critical wavelength increases linearly with film thickness at the initial stage of growth so that initially unstable growth can turn into stable growth after some time [50]. Here, kinetics is governed by adatom diffusion and is mainly influenced by strain and surface curvature. A more refined model is presented by *Yang et al.*. The surface chemical potential is given as

$$\mu(x) = \mu_0 + \gamma\Omega\kappa(x) + \Omega E_\mathrm{s} \quad , \tag{2.11}$$

where μ_0 denotes the surface chemical potential of the flat film, γ is the surface free energy per unit area, Ω is the atomic volume, $\kappa(x)$ is the surface curvature and E_s is the local strain-relaxation energy relative to a flat film. The topographical evolution of the film during growth is controlled by the chemical potential. Adatoms will diffuse from regions of high chemical potential to regions of lower chemical potential. The second term in the equation contains the curvature contribution to this process. Thus, considering the first two terms, on a curved surface adatoms will diffuse from convex regions (positive curvature, i.e. higher chemical potential) to concave regions (negative curvature, i.e. lower chemical potential). This surface energy consideration alone suggests that QDs should only nucleate in dimples/holes and not on mounds. Since QD nucleation on mounds was experimentally observed, the third term is added to the chemical potential to account for the strain contributions. Convex regions are prone to strain relaxation which makes them attractive for island nucleation. Hence, the second and third term of equation 2.11 oppose each other and the concrete shape of the surface will determine favorable QD nucleation sites. The mismatched thin film is treated as a bent film in order to derive the strain on the surface which is $\epsilon(z_s) = \kappa(z_\mathrm{s} - z_0)$, where κ is the curvature, z_s is the position of the top surface and z_0 is the position of the neutral plane of the bent film [51]. The strain relaxation energy is then given by

$$E_\mathrm{s} = -\frac{C}{2}\left(\frac{\kappa}{|\kappa|}\left[\kappa(z_\mathrm{s} - z_0)\right]^2 - f^2\right) \quad . \tag{2.12}$$

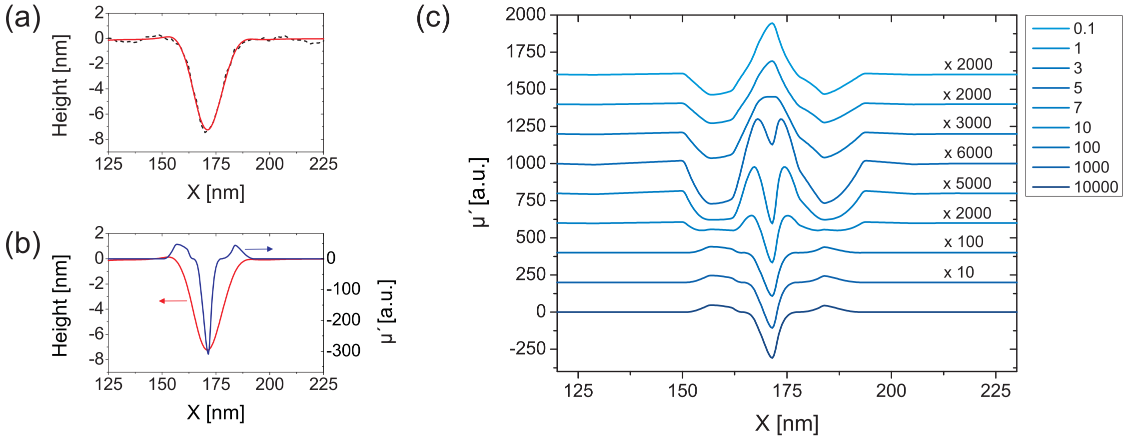

Figure 2.7 Construction of the chemical potential μ' from original AFM data. A hole profile (dotted black) was interpolated by cubic B-splines (solid red), (a). The chemical potential μ' (blue) is shown on top of the interpolated hole profile (red), (b). The parameter in equation 2.13 was set to $b = 1000$. The chemical potential exhibits a minimum at the bottom of the hole. Chemical potentials calculated for different values of b ranging from 0.1 to 10000, (c). For all cases potential minima are found so that adatoms will accumulate inside the holes.

C is an elastic constant and f is the misfit strain as defined in equation 2.8. Since the shape of the chemical potential is of interest here and not the absolute value inserting equation 2.12 in 2.11 and rearranging the chemical potential yields

$$\begin{aligned} \underbrace{(\mu(x)-\mu_0)\cdot\frac{1}{\gamma\Omega}-\frac{Cf^2}{2\gamma\Omega}} &= \kappa(x) - \underbrace{\frac{C(z_\mathrm{s}-z_0)^2}{2\gamma\Omega}}\cdot\operatorname{sgn}(\kappa(x))\kappa^2(x) \\ \mu'(x) &= \kappa(x) - b\cdot\operatorname{sgn}(\kappa(x))\kappa^2(x)\quad . \end{aligned} \tag{2.13}$$

Equation 2.13 can then be applied to any curve in order to obtain the chemical potential. The parameter b finally determines the shape of the chemical potential. For a qualitative understanding, the chemical potential is modeled for a single hole and depicted in figure 2.7. A hole profile was extracted from AFM data and the height points were interpolated using cubic B-Splines, see figure 2.7 (a). The resulting curve was then used to construct the chemical potential μ' in figure 2.7 (b). The parameters entering factor b are not all precisely known and approximated by using the values of table 2.1. In the end, it is the ratio between $(z_\mathrm{s}-z_0)^2$ and $C/2\gamma\Omega$ that determines the shape of μ'. Taking $b = 1000$ (which corresponds to $(z_\mathrm{s}-z_0)^2 = 64\,\mathrm{nm}^2$) results in a chemical potential which exhibits a minimum at the center of the hole so that adatoms will accumulate at this position. The situation changes if b is decreased, with the central minimum eventually disappearing at the occurrence of two minima which are found closer to the edge of the hole, see figure 2.7 (c). However, in all cases it is found that the curvature resulting from the given hole profile leads to chemical potential minima inside the hole. The detailed investigation of island nucleation inside holes by *Kutka and Kouris* provides further insights on nucleation sites depending on the growth rate and the amount of deposited material and will be taken up in chapter 5 [24]. The attractive force of a chemical potential minimum on adatoms is further illustrated by considering the adatom direction of diffusion which is described by

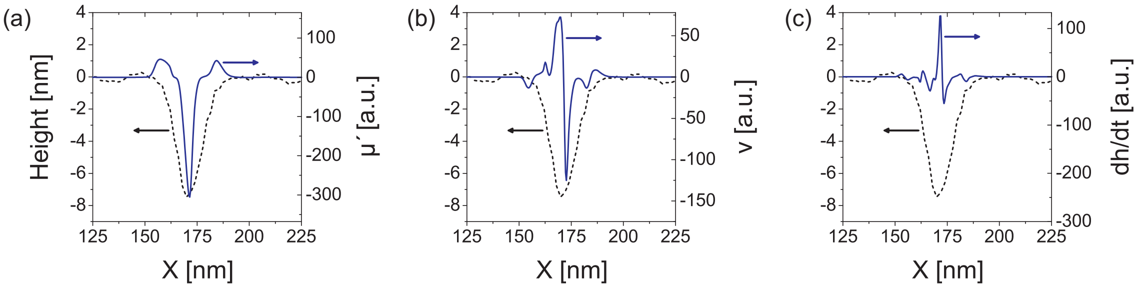

Figure 2.8 Calculation of the chemical potential μ' (a), the adatom diffusion velocity v (b) and the local change in surface profile $\partial h/\partial t$ (c) for $b = 1000$ (solid blue). The hole profile is shown as reference (dotted black). A local growth rate enhancement is observed at the bottom of the hole so that QDs will nucleate at this position earlier than on the flat surface.

the velocity along the surface as

$$v = -\frac{D_\mathrm{s}}{k_\mathrm{B}T}\frac{\partial\mu'}{\partial x} \quad . \tag{2.14}$$

This formulation is based on the *Nernst-Einstein* relation, with D_s being the surface diffusivity, $k_\mathrm{B}T$ is the thermal energy and the derivative with respect to x is taken along the surface [49]. The net flux of adatoms towards chemical potential minima leads to a local increase in growth rate at these locations. This is obvious when looking at the temporal change in surface profile

$$\frac{\partial h}{\partial t} = \frac{D_\mathrm{s}\Omega\delta}{k_\mathrm{B}T}\frac{\partial^2\mu'}{\partial x^2} \tag{2.15}$$

where δ denotes the number of atoms per unit area [49]. Figure 2.8 depicts the chemical potential derived for the given hole (a), the adatom velocity v (b) and the change in surface profile $\partial h/\partial t$ (c). Since the derivatives of equations 2.14 and 2.15 determine the evolution of the corresponding quantities along the surface, the prefactors in the respective equations were neglected in the calculations for simplicity. Furthermore, the chemical potential μ' was interpolated using cubic B-splines because the second order derivative of μ' is needed. The reason for that is, that μ' itself was constructed using second order derivatives (contained in the curvature κ) of interpolated AFM data whose higher order derivatives would vanish because of the cubic character of the B-splines. The strong increase in adatom diffusion around the hole bottom leads to the described local growth rate enhancement at the hole bottom, as clearly seen from the peak in (c). Due to this increased growth rate the critical thickness for island formation is reached earlier inside the hole than on the flat surface. Therefore, QDs will nucleate at locations defined by the holes. By properly designing the holes and choosing the right growth conditions, it should hence be possible to obtain well positioned QDs while avoiding random QD nucleation.

Summary

It was shown that nm sized islands of InAs incorporated in a GaAs matrix can be described as QDs. The formation of InAs islands on a GaAs substrate is governed by the lattice mismatch between the two semiconductors. The larger InAs lattice is strained while adopting the GaAs lattice size. Therefore, elastic energy is stored inside the deposited InAs film which increases during growth. If the elastic energy becomes as large as the energy to form a coherent island, the strain will relax by forming nm sized islands. This situation is characterized by a critical thickness. Such islands are randomly distributed on the surface. By altering the shape of the surface and therefore changing the surface chemical potential it is, however, possible to enforce the nucleation of QDs at desired locations. Small holes on the surface can act as nucleation sites due to local growth rate enhancement at the bottom of the holes. It turned out that design and shape of nucleation sites influence the site-selective growth of QDs. General aspects of sample preparation will be discussed in the following chapter.

3 General aspects of sample preparation

The mechanisms to guide quantum dot growth have been introduced in the previous chapter. It was shown that quantum dot nucleation can be enforced by manipulating the surface chemical potential. Small holes act as potential well for adatoms which will accumulate inside of these and subsequently form islands. Defining nucleation sites by creating small holes on the substrate surface is hence a critical task which influences the subsequent quantum dot formation. For this reason, general aspects of sample preparation will be considered in this chapter. The sample preparation comprises two main tasks which are the creation of the hole pattern on the substrate surface and the growth of quantum dots on top of that patterned surface. Lithographic techniques combined with wet chemical etching are used to define and create a hole pattern. The basic principles of this top down approach will be presented in section 3.1. Increased structural control of the hole shape can be achieved by employing dry chemical etching, as will be shown in section 3.2. The growth of InAs quantum dots on patterned GaAs substrates by molecular beam epitaxy is then described in section 3.3. Detailed process parameters of the sample preparation are summarized in appendix A.

3.1 Lithography and wet chemical etching

Lithography is the process of printing patterns onto a thin film called a resist, using a localized interaction between this layer and an engraving micro-tool or particle beam [52]. Optical lithography as a conventional lithographic technique is most common in fabrication of microelectronic devices. In this case, a photo-sensitive resist is exposed to light of appropriate wavelength (down to the UV range) through a mask so that the pattern of the mask is projected onto the resist. Due to its parallel character optical lithography allows for high throughput. However, the essential drawback of this technique is the resolution which is limited by diffraction of the incident light at the edges of the mask. Furthermore, the large wavelength of the light adds to the disadvantages. The *Rayleigh* criterion sets a lower limit of resolution

$$l_{\min} = \frac{k\lambda}{\mathrm{NA}} \tag{3.1}$$

where k is a technical parameter depending on the lithography setup (usually < 1), λ is the wavelength of the used light and NA is the numerical aperture. Its value ranges between 0 and 1 and is given by $\mathrm{NA} = n \sin\alpha$ with the refractive index n and the half-angle α of the maximum cone from which light is gathered. Structures smaller than $l_{\min}$ cannot be resolved and therefore not transferred from the mask into the resist. Developments using deep ultraviolet (DUV) and extreme ultraviolet (EUV) light could push the resolution limit down to 50 nm and possibly below. However, if smaller structures are desired a different technique has to be applied. The same holds for the fabrication of the masks which contain the small features.

3.1.1 Principles of electron beam lithography

In order to obtain a beam with very small wavelengths it is reasonable to use massive particles instead of light. Electrons are the particles of choice since they are easily generated in a cathode and accelerated by electric fields. The *de Broglie* wavelength was already introduced earlier but in this case the kinetic energy is provided through the electric potential drop such that

$$\lambda_{\text{de Broglie}} = \frac{h}{p} = \frac{hc}{\sqrt{E^2 - m_\mathrm{e}^2 c^4}} = \frac{hc}{\sqrt{E_\mathrm{kin}^2 + 2E_\mathrm{kin} m_\mathrm{e} c^2}} \tag{3.2}$$

$$= \frac{hc}{\sqrt{E_\mathrm{el}^2 + 2E_\mathrm{el} m_\mathrm{e} c^2}} \tag{3.3}$$

where h is the *Planck* constant, p is the electron's momentum, m_e is the rest mass of the electron, c is the speed of light, E is the relativistic energy of the electron, E_kin is the kinetic energy and E_el is the electric field energy. The relativistic energy-momentum relation was used to replace the momentum by the total energy. Electrons being accelerated by a voltage of 10 kV acquire a kinetic energy of $E_\mathrm{kin} = E_\mathrm{el} = eU = 10\,\mathrm{keV}$ which leads to a wavelength of $\lambda_{\text{de Broglie}} = 0.01\,\mathrm{nm}$. Inserting this value in equation 3.1 yields a theoretical resolution far below 1 Å which is not observed in real systems. Process parameters as well as technical and environmental limitations increase the resolution limit to a few nm which is still far below the limit for the light sources. Electron beam lithography is a very versatile technique since no masks are required and lithography parameters can thus be optimized and adapted very easily.

The basic principle of EBL is simple. A focused electron beam reproduces a defined pattern by scanning a substrate which is covered with an electron sensitive resist. The electrons locally interact with the resist material and alter its chemical composition. Chemical solutions called developers are thereafter used to remove the exposed or unexposed parts of the resist, depending on the type of resist in use. Afterwards, the pattern in the resist is transferred into the underlying substrate by chemical etching with the resist acting as etch mask.

As a first step before the exposure the GaAs substrate (full wafer or piece of GaAs) needs to be coated with the resist. For this purpose, the substrate is covered with a resist solution and then rotated at high speed in a designated device. This process is referred to as spin-coating. The high speed rotation leads to evaporation of the solvent so that only a thin film of resist remains on the wafer and it further ensures a uniform coverage of the wafer. The film thickness h is determined by the speed of rotation through the relation

$$h = \frac{k}{\omega^\alpha} \tag{3.4}$$

in which ω is the angular frequency and k and α (> 0) are empirical constants which include physical properties of the polymer, polymer/solvent and solution/substrate interactions [53]. Thus, thin resist films which are required for high resolution lithography are obtained by high rotation speeds. After coating the resist is baked in an oven or on a hot plate in order to remove residual solvent and harden the film for the subsequent exposure.

Two types of resist can be distinguished: positive type and negative type. In a positive resist, parts exposed by the electron beam will be removed in the subsequent development step. In contrast, parts exposed by the electron beam in a negative resist will remain on

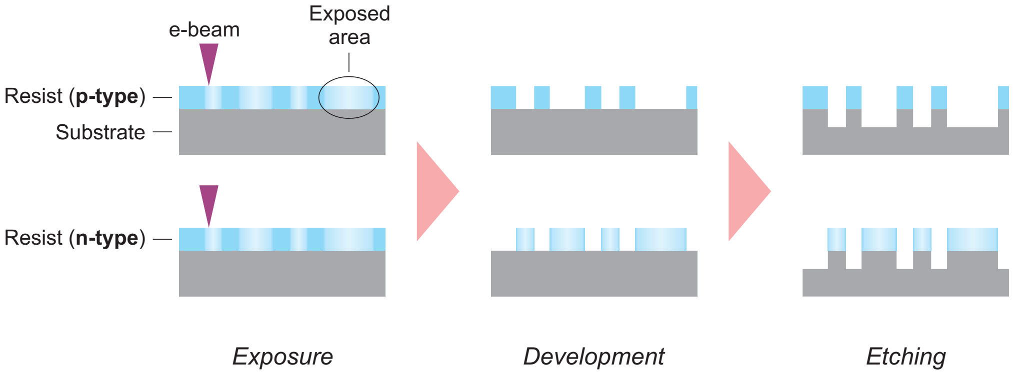

Figure 3.1 Illustration of electron beam lithography with two different resist types. The depicted steps include exposure of the resist, development of the exposed structures and pattern transfer by etching. Structures exposed in a positive (p-type) resist will be removed during development while they remain in a negative (n-type) resist.

the substrate during development while unexposed parts will be dissolved. The difference is illustrated in figure 3.1. The choice of resist thus depends on the needs of patterning. Both types of resists have been used throughout this work. In order to fabricate small holes on the substrate surface for guided QD growth a positive co-polymer resist is used. It consists of polymer chains of polymethyl methacrylate (PMMA) and methacrylic acid (MA) and is solved in 1-methoxy-2-propanol. PMMA/MA exhibits a 3- to 4-fold increase in sensitivity and contrast compared to standard PMMA, a widely used resist in EBL. The contrast describes the transition between exposed and unexposed parts at the edge of exposed areas. The transition region extends from fully exposed to completely unexposed resist. A high contrast hence corresponds to a very narrow transition region with the theoretical limit of a sharp transition between exposed and unexposed resist. During exposure the incoming electrons interact with the resist in such a way that the main polymer chains are broken. The scission is induced by ester side group elimination [54]. As a consequence, the molecular weight is reduced and the exposed parts of the positive resist are washed out in the development step, leaving the unexposed areas unchanged. The result is a mask with holes according to a defined pattern which can subsequently be transferred into the substrate by chemical etching. In order to fabricate mesa structures a resist based on novolac (phenol-formaldehyde resin) is used. Such a negative resist is not completely polymerized before exposure. The interaction with the incoming electrons leads to a completion of the polymerization so that the exposed parts of the resist become less soluble during development.

3.1.2 Relevant exposure parameters

In this work, a conventional scanning electron microscope (SEM) is used for exposure of the resist. In order to expose arbitrary patterns a few systems are attached to the SEM comprising a beam blanker to turn the beam on and off, a control unit that guides the beam in order to only “write” the defined structures and a pattern generator to define the desired structures and patterns. The pattern generator is a computer aided design (CAD) tool that converts the structures into a format suitable to the control unit.

The electron source together with the electron optics are referred to as the column of the SEM. The electrons for the beam are extracted from a tungsten tip through field emission. An electric field distorts the *Coulomb* potential of the tungsten atoms at the tip so that tunneling through the barrier becomes probable. The emitted electrons are then accelerated to an anode up to the desired energy set by the voltage U according to $E = eU$. The number of electrons in the beam, hence the beam current I, can be adjusted by placing an aperture in the beam path. The aperture consists of a hole in a nonmagnetic metal (e.g. gold, silver, etc.) plate. The beam is wider than the hole and therefore a certain fraction of electrons cannot pass the aperture. Hence, the size of the hole controls the beam current for a given acceleration voltage. Different apertures are present in the SEM and can be addressed by electromagnetically shifting the beam, thus allowing for beam currents from a few pC up to several nC. After the aperture, the electron beam is brought into the right shape and size in an electromagnetic lens system by axial magnetic fields and focused to a spot on the sample. Finally, the focused electron beam is deflected by two perpendicular scanning coils and is either used to scan a sample for imaging or to expose a specific area on a resist coated sample for lithography.

The exposure of readily coated GaAs samples takes place in a vacuum environment in order to avoid interaction of the beam electrons with surrounding gas atoms which would degrade the beam properties. The acceleration voltage U and hence the beam energy is one of the main parameters that strongly affects the results of high resolution lithography since the beam energy has an influence on the resolution limit, as will be described later. The number of deposited electrons is termed dose. Three dose types can be distinguished according to the type of structure that is exposed:

Structure type	Dimension	Dose type	Unit
Polygon	2D	D_{area}	μC/cm^2
Line	1D	D_{line}	nC/cm
Dot	0D	D_{dot}	pC

Table 3.1 Different structures in electron beam exposure.

In order to fully expose a structure in the resist a certain amount of electrons is required to allow for the complete scission of the polymer chains. The full exposure can hence be characterized by a minimum dose D_{min}. The value of this minimum dose depends on the characteristics of the resist but also on the beam energy. According to the *Rutherford* formula, which is appropriate for non-relativistic electrons and therefore a limit of the relativistic *Mott* formula, the cross section for elastic scattering processes is inversely proportional to the square of the incident electron energy. The electron resist interaction should follow a similar law. A lower cross section requires a higher dose to fully expose the structures. Hence, the minimum dose is inversely proportional to the cross section and therefore depends on the beam energy E_{inc} as

$$D_{\text{min}} \propto \frac{1}{\mathrm{d}\sigma/\mathrm{d}\Omega} \propto E_{\text{inc}}^2 \tag{3.5}$$

where $\mathrm{d}\sigma/\mathrm{d}\Omega$ denotes the differential scattering cross section. This behavior was verified in the work of *Mayer* by analyzing the minimum dose depending on the beam energy [55], as illustrated in figure 3.2. A parabola was fitted to the data yielding good correspondence to the expected square-like dependence on the incident beam energy. The function of the fit curve is also given in the diagram. The values of D_{min} were obtained from area exposures, i.e. exposure of two-dimensional structures. In this case, the absolute number of deposited electrons might differ from dot exposures where electrons are only deposited at a single spot. Exposure of areal structures such as polygons is obtained by subsequent deposition

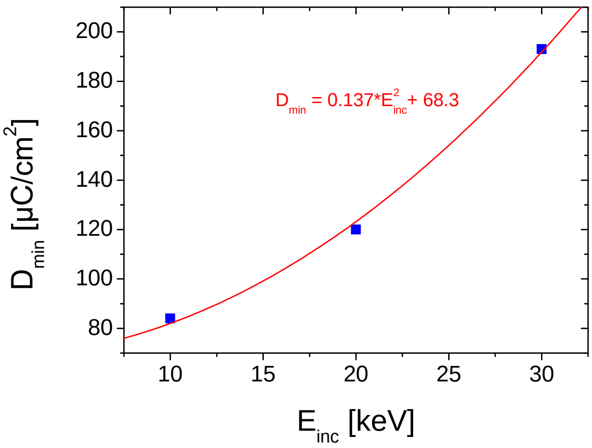

Figure 3.2 The minimum dose to fully expose two-dimensional structures is shown as a function of incident beam energy. Due to the lower cross section the electron-resist interaction is reduced for higher beam energies. The minimum dose is roughly proportional to the square of the incident beam energy, as verified by the fitted parabola. The data is taken from [55].

of electrons at individual regularly spaced spots which fill up the structure. The same is true for line exposures with the difference that the exposure spots are spaced along a line. The spacing between these individual exposure spots is called step size. The step size s is another important parameter in electron beam lithography as it influences the lithographic result. It is clear that the step size should be much smaller than the two- or one-dimensional structures, otherwise a closed structure is not possible. Furthermore, smooth edges are only obtained if the consecutive exposure spots are close enough to each other. Since the exposure of each individual spot leads to a round shaped structure a too large separation of the spots would lead to a rough edge. The correct step size is thus essential because only a continuous overlap of all the exposure spots will result in a defined two- or one-dimensional structure of high quality. That is the reason why the step size should be as small as possible for the exposure of nanostructures.

Due to technical limitations the step size cannot be made arbitrarily small. The digital pattern generator of the lithography system used in this work is based on a 16 bit system. The writefield defining the maximum area in which structures can be defined is thus divided into 2^{16} pixels. The distance between each pixel then defines a lower limit for the step size such that

$$s \geq \frac{d_{\mathrm{wf}}}{2^{16}} \tag{3.6}$$

where d_{wf} denotes the writefield size in µm. By selecting the smallest available writefield size of 50 µm it is hence possible to reduce the step size to $s = 1\,\mathrm{nm}$.

The beam current depends on the acceleration voltage U and the aperture size d_{ap} and is therefore written as $I(U, d_{\mathrm{ap}})$. Using the step size it is possible to relate the beam current

Parameter	Symbol	Limit		Depends on
Acceleration voltage	U	$30\,\mathrm{kV}$	max	
Aperture size	d_{ap}	$7.5\,\mathrm{\mu m}$	min	
Beam current	I	$16\,\mathrm{pA}$	min	U, d_{ap}
Dose	D_{area}	$200\,\mathrm{\mu m/cm^2}$	min	U
	D_{line}	n.a.	min	U
	D_{dot}	$6\,\mathrm{fC}$	min	U
Writefield size	d_{wf}	$50\,\mathrm{\mu m}$	min	
Step size	s	$1\,\mathrm{nm}$	min	d_{wf}
Dwelltime	t_{d}	ns	min	I, s, D_{x}

Table 3.2 Important exposure parameters for high resolution electron beam lithography and their technical limits using the RAITH Elphy Plus/Zeiss SUPRA lithography system. The minimum dose is given for a 80 nm thick PMMA/MA resist.

to other exposure parameters for different structures:

$$I(U, d_{\mathrm{ap}}) = \frac{Q}{t} = \frac{n \cdot \mathrm{e}}{t} = \begin{cases} \dfrac{s^2 \cdot D_{\mathrm{area}}}{t_{\mathrm{d}}} & \text{(2D)} \\ \dfrac{s \cdot D_{\mathrm{line}}}{t_{\mathrm{d}}} & \text{(1D)} \\ \dfrac{D_{\mathrm{dot}}}{t_{\mathrm{d}}} & \text{(0D)} \end{cases} \tag{3.7}$$

The number of electrons which are deposited at each individual exposure spot is denoted as n and t_{d} is the so called dwelltime, i.e. the time that is needed to expose the structure. It is now possible to compare the exposure of structures depending on their dimension by rearranging equation 3.7 to $n = s^{\mathrm{dim}} \cdot D_{\mathrm{dim}}/\mathrm{e}$, where dim stands for the dimensionality of the structure. The minimum dose to fully expose a two-dimensional structure using an energy of 30 keV is roughly $200\,\mathrm{\mu C/cm^2}$ which yields $n = 12.5$ for a step size of $s = 1\,\mathrm{nm}$. The minimum dose in a dot exposure under similar conditions amounts to about $D_{\mathrm{dot}} = 6\,\mathrm{fC}$ which yields $n = 37000$. This illustrates the difference in exposure of structures of different dimensionality. One reason why single exposure spots of two-dimensional structures require much less electrons is given in the following section.

The main exposure parameters for electron beam lithography have been introduced and their values have been continuously improved throughout the works of *Helfrich* [39] and *Mayer* [55] and in this work. The optimized values are given in the appendix and the main parameters are summarized in table 3.2 for an overview.

3.1.3 Limitations of electron beam lithography

As mentioned before, the beam size and therefore the real resolution is mainly limited by technical facts. Spherical and chromatic aberration are the two main causes which cannot be completely avoided. In general, the SEM is designed in a way that aberration effects are minimized but not completely eliminated. Spherical aberration describes the fact that peripheral electrons far away from the beam center are less deflected than electrons in the center due to an increased field near the windings of the electromagnetic lens. This produces at the beam focus a beam broadened to a disk rather than a point. The spherical aberration d_{sph} is related to the accelerating voltage U and the aperture angle α by

$$d_{\text{sph}} \propto \frac{\alpha^3}{U^2} \tag{3.8}$$

with the aperture angle being defined by $\text{NA} = n \sin\alpha \approx d_{\text{ap}}/2f_{\text{foc}}$ where d_{ap} is the diameter of the aperture and f_{foc} is the focal length. One way to reduce the spherical aberration is to use the aperture with the smallest diameter d_{ap}. Chromatic aberration describes the deflection of electrons depending on their wavelength and thus kinetic energy. In opposition to light, electrons with smaller wavelength (corresponding to larger energy) will be less deflected. Since the emission of electrons from the source is a statistical process an inherent spread in electron energies will always be found. Furthermore, the fields used to accelerate the electrons are subject to tiny fluctuations which cannot be avoided. Therefore, chromatic aberration is always present and its extent depends on the technological efforts to reduce the described fluctuations. The diameter of the disk which results from chromatic aberration is given by

$$d_{\text{cro}} \propto \frac{\Delta E}{E}\alpha \tag{3.9}$$

where $\Delta E/E$ is the fractional energy spread for a given acceleration voltage. Again, taking the smallest aperture helps in reducing the chromatic aberration and, as a consequence, to decrease the spot size. A further reduction of the spot size on the sample can be achieved by decreasing the working distance, i.e. the distance between sample and SEM column. Astigmatism is a third effect that limits the resolution. It occurs when the cross section of the beam is not perfectly circular but rather elliptical. One reason might be non-symmetrical fields in the electron optics. Electrons from the short axis of the ellipse are less deflected so that two focal points appear. Unlike aberration effects, astigmatism can be corrected manually by superimposing an asymmetric field in order to cancel the original asymmetry. The correction of astigmatism prior to electron beam exposure is required for good lithographic results.

After describing the technical factors limiting the resolution, constraints due to other lithographic parameters are presented. Despite a beam size in the focus of around 2 nm this does not automatically enable the lithographic creation of structures with sizes of the same order. First of all, the primary electrons (PE) of the beam penetrating into the resist are subject to scattering processes. Especially forward scattering will lead to divergence of the beam during its way through the thin resist film and thus decrease the resolution. While this scattering process is elastic secondary electrons (SE) are generated by inelastic scattering leading to undesired exposure. Once the beam penetrates the GaAs substrate the primary electrons can be scattered from the crystal back (BSE) into the resist resulting in a broad rearward exposure of the resist. The exposed area is thus increased by these mechanisms. The degree of additional exposure mainly depends on the beam energy. As described above, the cross section for elastic scattering is inversely proportional to the squared kinetic energy so that electrons of higher energy experience less forward scattering. Though, such electrons will penetrate deeper into the substrate and thereby increase the probability for back scattering. Hence, forward scattering and back scattering act in a complementary way since higher (lower) beam energies lead to less (increased) forward but increased (less) back scattering. Still, higher electron energies are advantageous since the back scattered electrons distribute over a larger area, thus reducing the intensity of rearward exposure. These processes are schematically shown in figure 3.3. Other products of electron substrate interaction such as *Auger* electrons (AE) or X-rays do not contribute to the resist exposure.

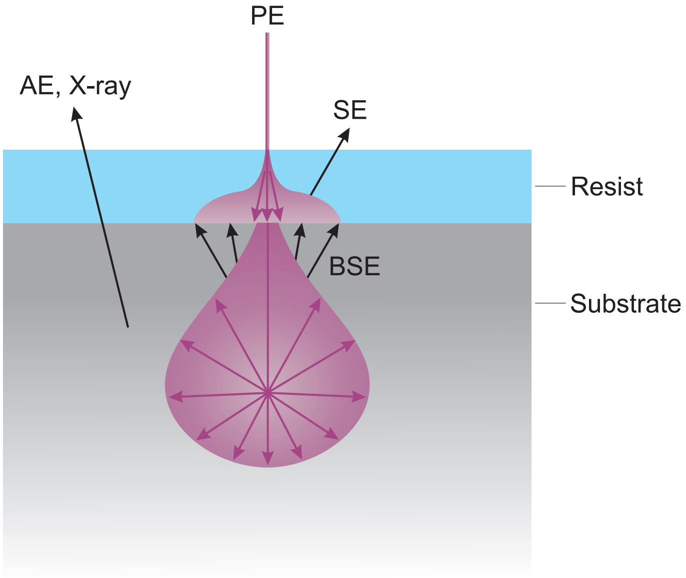

Figure 3.3 Illustration of electron interactions in the resist and substrate. Primary electrons (PE) experience mainly forward scattering in the resist but secondary electrons (SE) are generated through inelastic processes. Back scattered electrons (BSE) originate from electron scattering in the crystalline substrate. *Auger* electrons (AE) and X-rays do not contribute to the exposure.

Monte Carlo simulations including the interaction of electrons with the resist and the substrate can be carried out in order to visualize the broadening of the penetrating beam and the undesired exposure in the resist. The energy of the incident electrons was varied as well as the resist thickness. The original beam contains 2,000 primary electrons. The simulations were done using the free software “Casino” which simulates electron trajectories in solids [56]. Figure 3.4 shows three simulations with different values for the beam energy and the resist thickness. Beam energies of 10 keV and 30 keV and resist thicknesses of 80 nm and 300 nm were used. The blue trajectories correspond to forward scattered electrons, red trajectories to back scattered electrons. The simulation uses the Mott cross section as a model for scattering. The figures (b), (d), (f) are magnifications of figures (a), (c), (e), respectively. Comparing figures (a) and (c) it is obvious that electrons of higher energy penetrate deeper into the substrate. This in turn leads to back scattering from a larger volume and therefore wider field of rearward exposure. For lower energy, undesired exposure is confined to a smaller area. Comparing the figures (b) and (d) a reduced broadening of the higher energy beam is observed due to the lower cross section of faster electrons. This is beneficial if small structures are to be defined in the resist. Despite the rearward scattering into a larger area the density of electron trajectories is less than in the lower energy case so that polymer chain breaking becomes less pronounced. Taking a thicker resist does not significantly change the volume into which electrons are scattered, as seen from figure (e). However, the density of electron trajectories and hence possible exposure is further reduced in the resist, as illustrated by figure (f). At the same time, the exposed area increases with resist thickness because of the forward scattered electrons. This effect becomes more dramatic since a larger amount of electrons is necessary to fully expose the resist. Altogether, it is therefore advantageous to use thin resists and high electron energies in order to define nanostructures in the resist precisely. The rearward exposure forms a background which becomes more uniform and less pronounced with

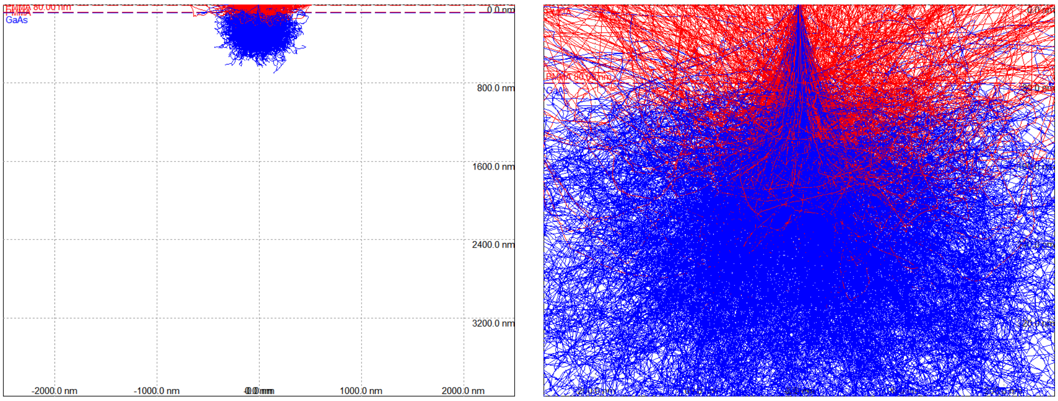

(a) 80 nm PMMA, 10 keV, 5000 × 4000 nm^2 (b) 80 nm PMMA, 10 keV, 500 × 400 nm^2

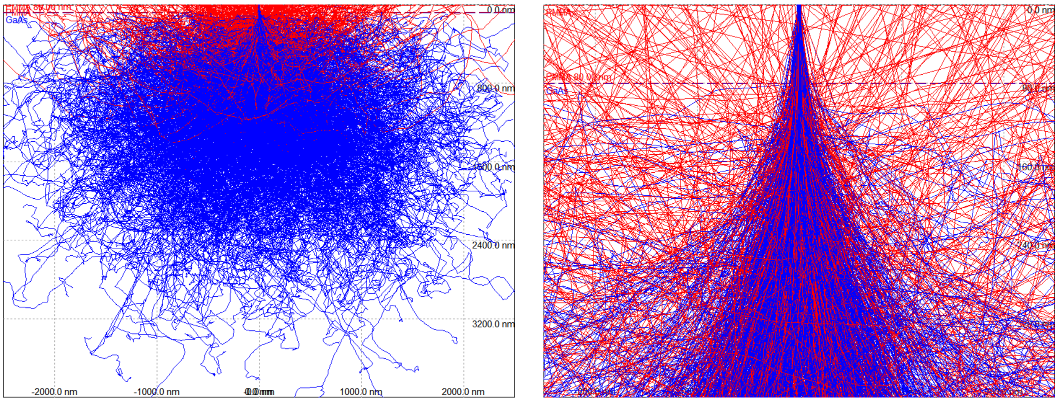

(c) 80 nm PMMA, 30 keV, 5000 × 4000 nm^2 (d) 80 nm PMMA, 30 keV, 500 × 400 nm^2

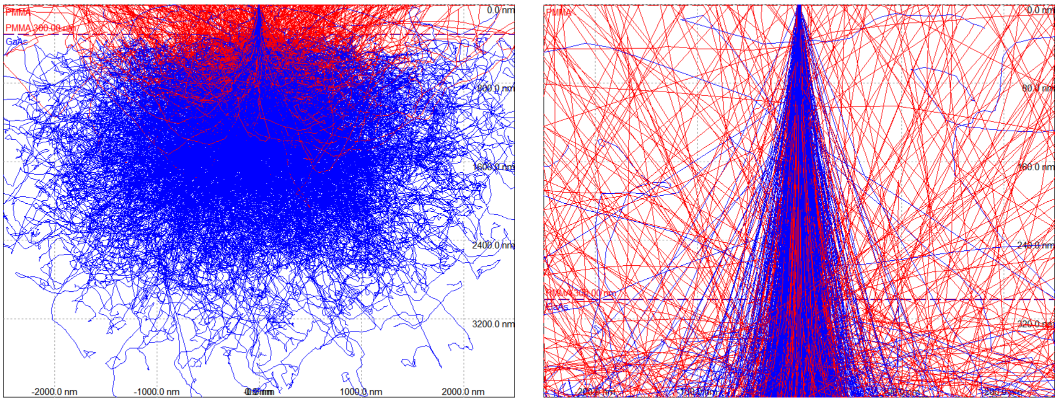

(e) 300 nm PMMA, 30 keV, 5000 × 4000 nm^2 (f) 300 nm PMMA, 30 keV, 500 × 400 nm^2

Figure 3.4 Monte Carlo simulations of electron trajectories in a sample consisting of a thin PMMA film on top of a GaAs substrate. The profiles of the trajectories in the sample are shown. Blue trajectories correspond to forward scattered electrons, red trajectories to back scattered electrons. The red dotted line in the upper part of the figures marks the interface between resist and substrate. Resist thickness, beam energy and figure size are given in the respective figure captions. Figures (b), (d), (f) are magnifications of figures (a), (c), (e), respectively.

higher beam energies.

Depending on the arrangement of the structures rearward exposure can still cause some

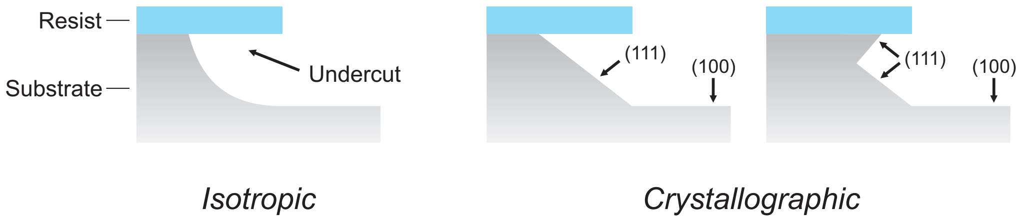

Figure 3.5 Illustration of wet chemical etching which can either be isotropic or crystallographic, depending on the type of etch solution used and its concentration. In both cases lateral etching leads to an undercut of the etch mask.

trouble. Two cases can be distinguished. If several nanostructures are found in proximity to each other the exposure of one structure can affect the exposure of neighboring structures through rearward exposure. This will possibly lead to overexposure and therefore the structures might become larger than defined. The intensity of mutual exposure increases with decreasing spacing between the structures. This effect is called inter proximity effect. A similar mechanism applies to structures of different width. A minimum dose is required to fully expose the resist. As described above, the exposure of two-dimensional structures is obtained from subsequent exposure of single spots, filling the area of the defined structure. Hence, rearward exposure is expected from neighboring exposure spots. In this case, however, the intensity of mutual exposure is reduced with decreasing structure width. The effective dose deposited in the resist thus depends on the structure size and gets smaller with decreasing structure size. As a result, small two-dimensional structures might be underexposed while larger ones are correctly exposed. This effect is known as intra proximity effect. It is one reason why individual exposure spots in the exposure of two-dimensional structures require much less electrons compared to dot exposure. These proximity effects are less pronounced in the lithographic structures of this work since mainly dot exposure is used to define large regular arrays of nanometer sized holes. However, a small effect is still expected at the edges of the hole arrays as less neighboring exposure spots are located here and therefore a reduced background is found.

3.1.4 Principles of wet chemical etching

After nanostructures have been defined in the resist by electron beam exposure they need to be transferred into the underlying GaAs substrate. First, the exposed structures are developed in a developer bath for a sufficient amount of time so that the features fully emerge in the resist. Thereafter, the structures in the resist are transferred into the substrate by etching. The developed resist acts as an etch mask so that the etchant removes the substrate material where it is not covered with resist. Finally, the resist mask is removed from the substrate and the surface is cleaned resulting in a surface structured with small dips in the nanometer range. The pattern transfer was already illustrated earlier in figure 3.1. Using wet chemical etching (WCE) for the pattern transfer has several advantages. First of all, this etching method is simple to implement as it requires only benchtop glassware and no special equipment. Secondly, WCE causes virtually no electronic damage on the substrate surface. Thirdly, small etch rates are available which allows for a very precise control of the etch depth in the nanometer range.

In general, two mechanisms can be distinguished when etching crystalline materials such as the GaAs substrate. The etching can be either isotropic or crystallographic and will result in different etch profiles. In the first case, lateral and vertical etch rates are the same whereas in the latter case, the etch rate depends on the exposed crystallographic

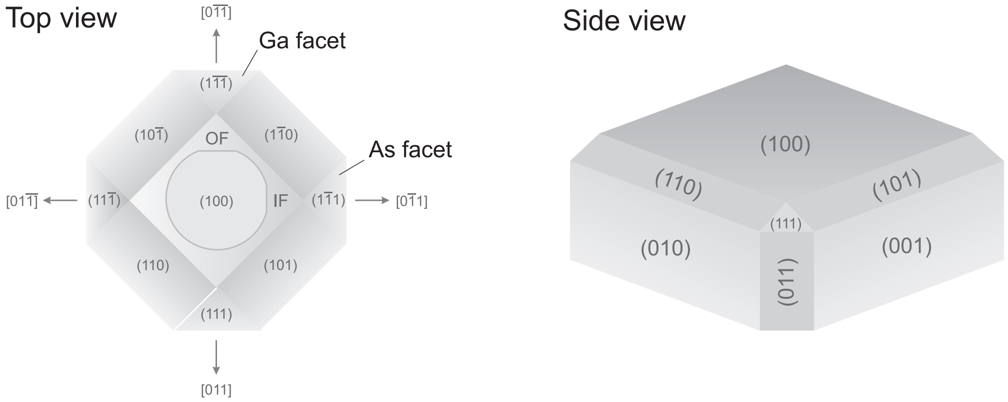

Figure 3.6 Facets of the GaAs crystal with a (1 0 0) surface plane. Ga- and As-terminated {1 1 1} facets are marked accordingly. The orientation of a real wafer with its two flats (OF and IF) is shown for reference.

plane resulting in selective etching [57]. Etch profiles obtained by the two mechanisms are depicted in figure 3.5. In both cases lateral etching is observed so that the etch mask will be undercut and the final structures will be larger than defined in the resist. The type of etch solution and its concentration will finally determine whether etching is isotropic or crystallographic.

In wet chemical etching the samples are immersed into an etch solution for a specific amount of time and then dipped into water in order to stop the etch reaction. The chemical mechanism of wet etching of GaAs is the oxidation of the surface to form Ga and As oxides, followed by the dissolution of these oxides by chemical attack with acids or bases [57]. Oxide complexes are formed by adding an oxidizer such as hydrogen peroxide (H_2O_2) to the etch solution. Thus, an etch solution consists of an oxidizer, an etchant (base or acid) and water to adjust the concentration. The rate of etching, i.e. the amount of material removed from the bulk per time, depends on two processes: oxidation and dissolution. The strength of each process can be described by a rate equation. The oxidation and dissolution rates r_{ox} and r_{diss} are given by

$$\begin{aligned} r_{\mathrm{ox}} &\propto [\mathrm{H_2O_2}]^m \cdot \{\mathrm{GaAs}\} \cdot \exp\left(-\frac{E_{\mathrm{ox}}}{k_{\mathrm{B}}T}\right) \\ r_{\mathrm{diss}} &\propto [\mathrm{a|b}]^n \cdot \{\text{oxide complexes}\} \cdot \exp\left(-\frac{E_{\mathrm{diss}}}{k_{\mathrm{B}}T}\right) \end{aligned} \tag{3.10}$$

where $[H_2O_2]$ and [a|b] are the concentrations of the oxidizer and the acid or base, respectively, m is related to the number of oxidizer molecules involved in the oxidation of one Ga and one As atom, n is related to the number of H^+ or OH^- molecules involved in the dissolution. The effective surface concentrations of exposed Ga and As atoms as well as their respective oxide complexes are given by {GaAs} and {oxide complexes}. The activation energies for the respective processes are denoted as E_{ox} and E_{diss}, k_{B} is *Boltzmann*'s constant and T is the temperature. The oxidation rate controls the overall etch rate and the dissolution rate is usually used to characterize the created profiles. It is assumed that sufficient oxidizer is provided. If the dissolution rate is then limited by the supply of etchant the etching is called diffusion-controlled. This eventually leads to strong undercutting and isotropic profiles. If the dissolution rate is limited by the dissolution energy E_{diss} it is called reaction rate-limited which results in crystallographic profiles. The etch rate in

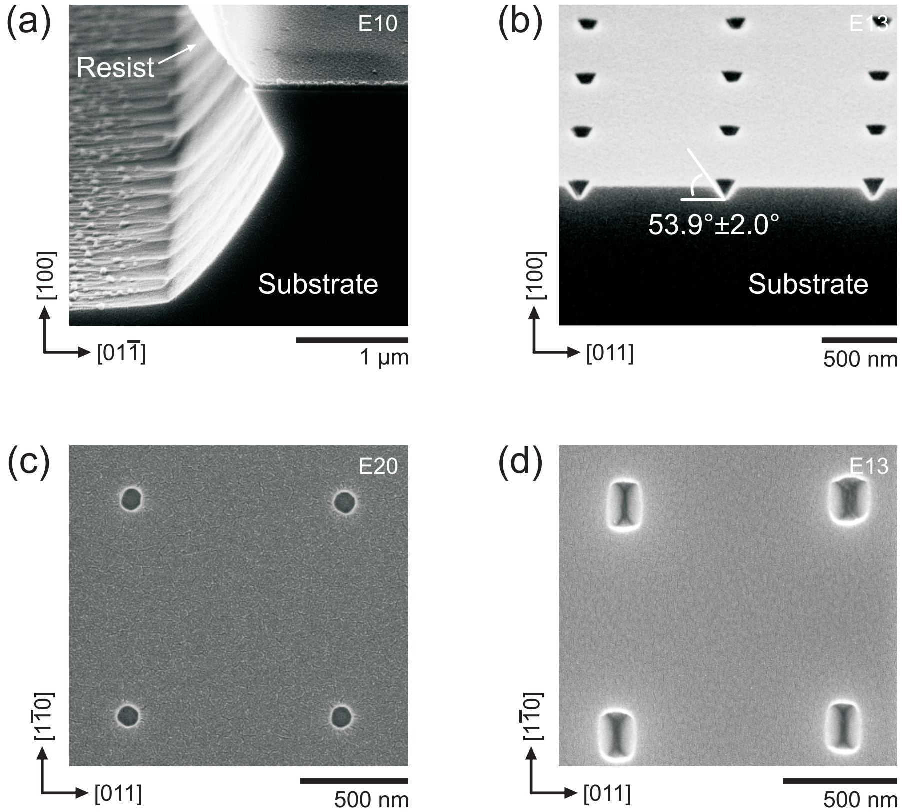

Figure 3.7 Etched samples using a H_2SO_4 based etch solution. A crystallographic profile due to reaction-rate limited etching is observed in (a). Lateral etching leads to undercut of the etch mask (the resist is still on the sample surface, bending upwards). A hole array etched into the GaAs substrate is displayed in (b). The resist has been removed. The average sidewall angle of the holes is given. Circular holes in the resist (c) transform into elongated rectangular dips in the GaAs substrate during etching (d). The samples in (c) and (d) are different. The resist was removed in (d) after etching.

diffusion controlled etches possibly decreases with etch time since the diffusion of etchant to the etched surface might be hindered as the structures get deeper. The dissolution rate is then governed by the term $[\mathrm{a}|\mathrm{b}]^n \cdot \{\text{oxide complexes}\}$ and is insensitive to temperature variation. However, agitation can influence the diffusion and therefore alter the etch rate. By diluting the etch solution the etching shifts to reaction rate-limited since the exponential term $\exp\left(-E_{\mathrm{diss}}/k_{\mathrm{B}}T\right)$ becomes dominant in the dissolution rate. In the course of this work, the latter case is favored as it allows for precise etching on the nanometer scale due to the high dilution and the subsequent small etch rate. Furthermore, the etching is not sensitive to agitation but temperature variations must be avoided.

The type of etchant used in WCE is of major importance as it determines the success of the etch process. Ammonia hydroxide (NH_4OH) was used as etchant in a preceding work [39]. Despite a low etch rate and highly controllable etch depth the results were not satisfying as the etched nanostructures exhibited frayed edges. The reason for that was the incompatibility of the basic etchant with the resist used for electron beam exposure. The NH_4OH attacks the PMMA/MA during etching and leads to non-uniform results. Switching to an acidic etch solution based on sulfuric acid (H_2SO_4) could solve this problem and hence allowed for regular structures with smooth edges.

When etching GaAs it is important to notice that this semiconductor is a compound of two atomic species. Ga and As faces have different activation energies and therefore the reaction rate-limited etching is sensitive to the crystal alignment. Figure 3.6 displays the crystal facets of GaAs for better understanding. The diluted H_2SO_4 based etch preferentially etches $\{1\,1\,1\}$ facets of the GaAs crystal. However, the etch rates in orthogonal crystal directions are not equal. Ga rich faces, i.e. $(1\,1\,1)$A type facets, usually etch two to five times slower than As rich faces, i.e. $(1\,1\,1)$B type facets [57]. This is observed in figure 3.7 where crystallographic etch profiles are obtained. In (a) a large trench was etched about 2 µm deep with a high etch rate of 7 nm/s. The surface is still covered with resist which bends upwards to reduce its surface energy. The undercut of the etch mask is well observed. In (b) a hole array was etched about 100 nm deep with a smaller etch rate of about 1 nm/s. The resist was removed afterwards. The measured average sidewall angle of $53.9 \pm 2.0°$ compares very well with the theoretical value for the angle between the $(1\,0\,0)$ and the $(1\,1\,1)$ planes which is 54.7°. The originally circular holes defined in the resist as in (c) transform into rectangular dips on the GaAs surface due to preferential etching of $\{1\,1\,1\}$ facets, see (d). Furthermore, the dips are elongated in the $[0\,\bar{1}\,1]$ direction because of the different etch rates for Ga- and As-terminated faces.

3.2 Using reactive ion etching to increase structural anisotropy

Although wet chemical etching provides good control of etch depth and conserves damage free surfaces the disadvantages in terms of structural control were demonstrated. Since christallographic facets are etched it is not possible to avoid undercutting of the etch mask with the given etchant and crystal orientation. The final structures in the substrate are therefore larger than originally defined in the resist. Furthermore, the structures exhibit structural asymmetry. In order to avoid these constraints dry etching (DE) methods have to be employed. Dry etching allows for conservation of the structure profile in the resist during pattern transfer into the substrate. Sidewall angles of up to 90° can be obtained for the etched structures with virtually no undercutting, i.e. the lateral size of the structure is as defined. In addition, the whole process is faster compared to WCE. However, dry etching methods require advanced and expensive equipment and might degrade the electronic properties of the etched surface.

Inert or reactive gases are used in dry etching. Depending on the etching process ions or gas molecules are directed onto the substrate surface where an interaction takes place. Two processes can be distinguished, namely physical etching and chemical etching. While only the latter is observed in chemical dry etching, in most other dry etching techniques both processes will contribute to the etching. The physical component relates to ions bombarding the surface like in sputtering. The ions bombarding the surface will mechanically knock out atoms at the surface of the substrate. In contrast, the chemical component is based on a chemical reaction like in wet chemical etching with the difference that the etchant is provided in a gaseous phase. While physical contributions will increase the anisotropy an increase in surface roughness might be observed. In contrast, chemical contributions lead to rather isotropic profiles and usually enhance the growth rate while producing less damage to the surface. In general, the balance between chemical and physical contributions to the etching for each type of process will largely determine these characteristics [57]. In the current work, a trade off between low etch rates, smooth surfaces and high anisotropy was sought after.

Reactive ion etching (RIE) has long been the standard dry process where reactive radicals and ions are formed and the ions are accelerated into the wafer at energies $> 50\,\mathrm{eV}$ to produce a mechanism that combines both chemical etching and physical sputtering [57].

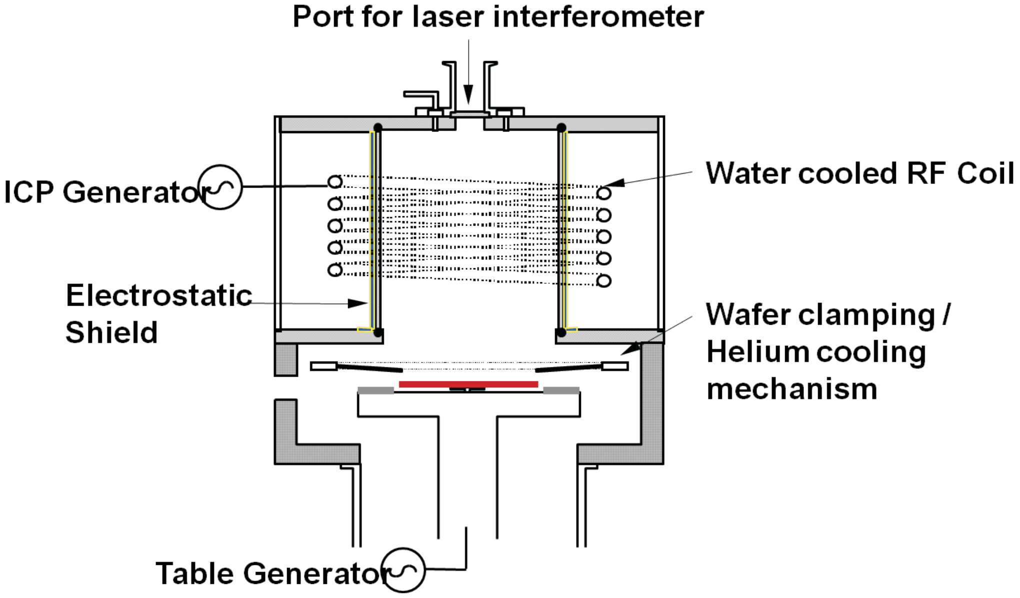

Figure 3.8 Schematic setup of the ICP-RIE reactor chamber with the main components. The substrate is colored in red. Taken from [59].

Only one radio frequency (RF) power supply is used to generate the plasma and to accelerate the ions to the wafer. This limits the control of the etch process and rather high etch rates and isotropic profiles are obtained with the gases conventionally employed for GaAs etching. This can be avoided by using two separate power supplies. The first generates the plasma and the second provides the RF power for the acceleration of the ions. Efficient dissociation of the source gases can be achieved by applying an alternating magnetic field that inductively creates the needed electric field [58]. The generated plasma is then termed as inductively coupled plasma (ICP). Hence, ICP-RIE provides semi-independent control of the plasma chemical species, both ions and neutrals, and the energy with which the ions hit the wafer surface.

The schematic setup of the ICP-RIE reactor used for DE is shown in figure 3.8 [59]. The substrate is put on a plate to which the RF signal is applied to accelerate the ions from the plasma towards the substrate surface. The plasma is generated in the inductively coupled field above the substrate. The RF power supply is operated at a frequency of 13.56 MHz and that of the ICP generator at a frequency of 2 MHz. The maximum available powers are 300 W for the RF generator and 1200 W for the ICP generator. Before supply of the gases and ignition of the plasma the chamber is pumped to high vacuum. Due to the gas supply the pressure can range between 1-100 mTorr during operation. ICP-RIE allows for lower etch rates compared to conventional RIE in which the pressure is higher during operation. The backside of the substrate can be cooled with He in order to reduce the heat impact during the etch process. Although the electrostatic shield reduces possible contamination of the chamber, cleaning of the chamber prior to each etch process is recommended. Halogen based gases are conventionally used in ICP-RIE of GaAs [57]. While Cl_2 and $SiCl_4$ were both available in the system in use, the latter is favored as it generally produces better surface morphologies, greater anisotropy and less change in surface stoichiometry than the analogous Cl_2-based etches [57]. Care must be taken of the fact that Si is a dopant for GaAs. However, ion implantation of Si at the near surface is only effective for accelerating voltages above 250 V. The RE powers applied in this work are so low that the resulting

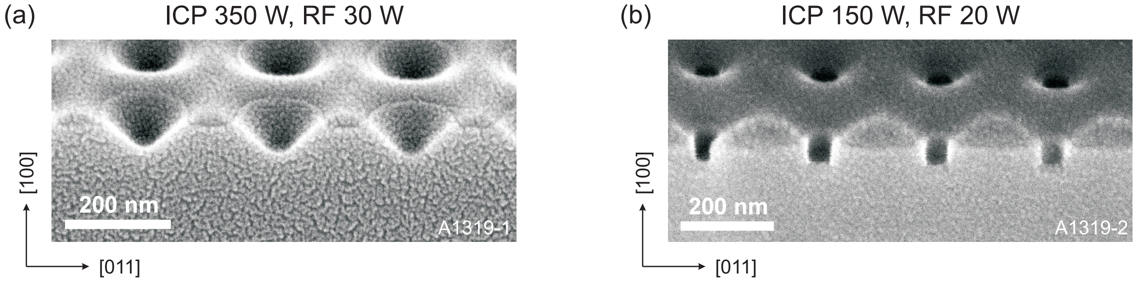

Figure 3.9 SEM images of hole profiles after dry etching using ICP-RIE. Higher powers for ICP and RF generator lead to a strong chemical contribution in the etching. Sloped sidewalls are the result, as in WCE, (a). A reduction of the etch rate and a higher degree of anisotropy was achieved by reducing both powers. Holes with vertical sidewalls and little lateral etching were obtained, (b).

DC biases are far below this limit. The $SiCl_4$ is dissociated to provide Cl atoms that react with the GaAs to form $GaCl_x$ and As_x compounds. The simultaneous bombardment with ions facilitates the removal of the etch products. Therefore, Ar atoms are added to the $SiCl_4$ in order to produce anisotropic profiles. The final etch rates, etch profiles and surface roughness will depend on process parameters such as the etch chemistry, the chamber pressure, the DC bias, the ICP power and the substrate temperature.

The DE process was optimized with respect to the needs of the site-selective growth in the work of *Mayer* [55]. Small etch rates and low lateral etching were desired. In order to demonstrate the power of ICP-RIE and the influence of the process parameters, two SEM images of hole profiles obtained in different etch runs are shown in figure 3.9. In (a) both ICP power and RF power were rather high so that the chemical contribution in the etch process is very dominant, as observed from the sloped sidewalls which are similar to those obtained in WCE. When decreasing the ICP power, thus decreasing the density of reactive species, the physical contribution becomes dominant and almost vertical sidewalls are obtained, as seen in (b). The etch rate could be reduced by decreasing the RF power and hence the acceleration voltage (DC bias).

3.3 Molecular beam epitaxial growth of InAs islands

Molecular beam epitaxy (MBE) is used in this work to grow InAs islands on pre-structured GaAs substrates. MBE is a material deposition technique in which a beam of atoms or molecules is directed onto a substrate where the species are deposited in order to form an overlayer, possibly adopting the crystal structure of the underlying substrate. It is mainly applied in the fabrication of thin semiconductor films. The case when substrate and overlayer are of the same material is defined as homoepitaxy, else the deposition is referred to as heteroepitaxy. If two or more different materials are deposited at the same time, e.g. gallium (Ga) and arsenic (As), these will form a compound under proper growth conditions, gallium arsenide (GaAs) in this example. In this way, a huge variety of material compositions can be obtained by providing the corresponding species with a desired ratio. The composition of the deposited layer can thereby be controlled with very high precision. The source material is usually contained in a crucible which is heated in order to evaporate the material. Evaporation occurs from a melt as in the case of Ga and indium (In) or from a solid as for As. The source materials need to be of high purity (usually on the order of 99.9999% or better) in order to allow for the growth of defect free layers.

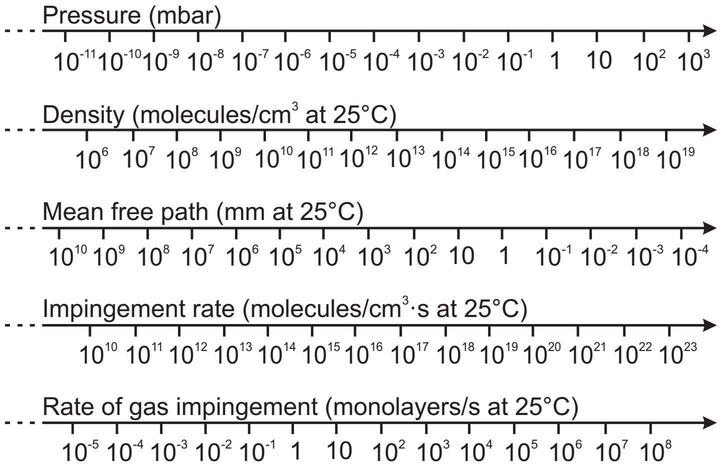

Figure 3.10 Relationship between fundamental quantities of vacuum technology derived from the kinetic theory of gases [60].

Another key requirement for high crystal quality of the fabricated layers is the ultra high vacuum (UHV) environment in which MBE is performed. First, reducing the pressure down to the UHV regime means decreasing the amount of residual gases (e.g. CO, CO_2, CH_4) which provide atoms that are potentially incorporated as defects or dopands in the grown layers (e.g. C is a dopand for GaAs). Second, the mean free path of atoms and molecules is drastically increased so that the species in the molecular beam do not undergo any reaction on their way from the source to the substrate. Using the kinetic theory of gases the relationship between fundamental quantities such as gas pressure and mean free path can be derived, as shown in figure 3.10. The unit monolayer (ML) is a useful quantity for growth processes as it describes the coverage of a flat surface by one atomic layer. As a flat crystalline surface contains between 10^{14} and 10^{15} atoms per cm^2 a pressure of 10^{-6} mbar corresponds to an impingement rate that leads to the deposition of 1 ML per second, if all incident species adsorbed on the substrate. The strong vacuum requirements intrinsically define the characteristics of the MBE process. Slow growth rates (GRs) are found which is appropriate for the growth of thin films and which allows for atomically flat interfaces between layers of different materials. MBE is thus a powerful research tool but not suitable for mass production. For the latter case, other deposition techniques like metal organic chemical vapor deposition (MOCVD) or hydride vapor phase epitaxy (HVPE) have to be employed.

Allowing for *in situ* monitoring of the growth process and characterization of the sample is another advantage of the UHV environment. Reflection high energy electron diffraction (RHEED) is a technique commonly used in MBE to retrieve information on the state of the sample surface. An electron beam of high energy up to 20 keV is directed onto the sample surface under a small angle of incidence (about 5°) leading to diffraction on the surface. The diffraction pattern is displayed on a fluorescent screen, where information of the crystal quality, growth mode and surface reconstructions can be extracted [61]. In addition, RHEED can be used to calibrate growth rates of arsenic compound semiconductors.

All samples in this work were grown with a Riber Compact 21T molecular beam epitaxy system. The basic setup of the system is depicted in figure 3.11. It consists of three UHV chambers of different size, namely the growth chamber, the buffer chamber and the loading chamber, which are connected through plate valves. Further equipment is attached

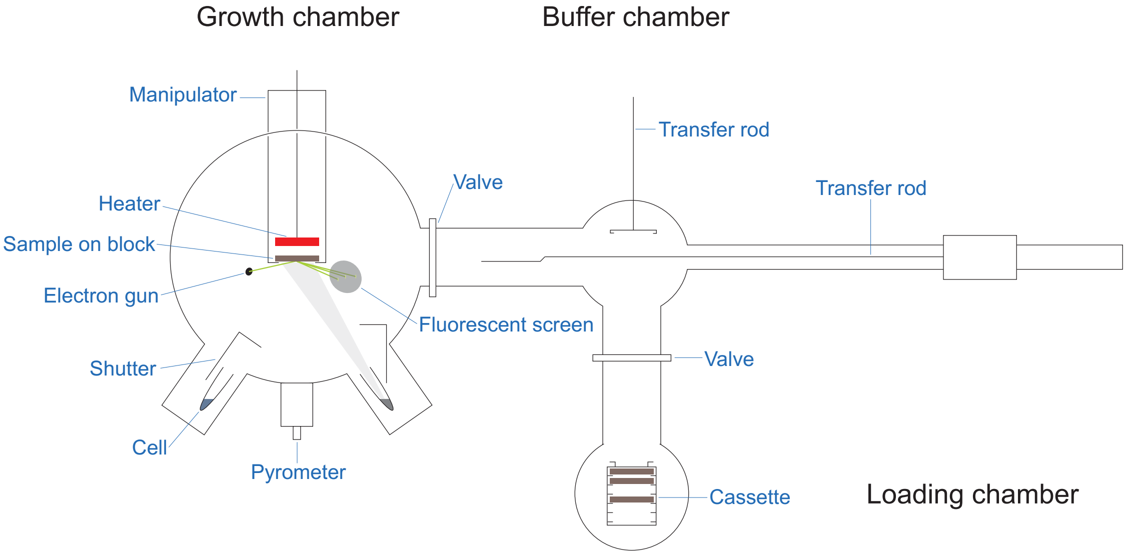

Figure 3.11 Schematic setup of a molecular beam epitaxy system including some key components.

to the chambers in order to ensure proper operation. The growth chamber as well as the buffer chamber are constantly kept at UHV condition whereas the loading chamber is vented when samples are loaded into or taken out of the MBE system. Separating the loading chamber from the growth chamber and opening only one valve at a time reduces the possibility of contaminants entering the growth chamber.

The growth chamber is the heart of the MBE system where the materials are deposited on the substrate. It is connected to an ion getter pump, a titanium (Ti) sublimation pump and a helium (He) cryogenic pump operating at 11 K to keep the chamber under UHV. The latter is however not used during growth. The inner side of the chamber is surrounded by a cryoshroud which is permanently fed with liquid nitrogen (LN2) from a phase separator through vacuum jacketed pipes. Besides the pumps the cryoshroud is an important component of the MBE system as it helps maintaining UHV condition inside the chamber. Residual gases in the chamber condense on the cold surface of the cryoshroud so that the background pressure is reduced. A hot-cathode ionization gauge is fixed inside the chamber in order to measure the pressure. A mass spectrometer is also connected to the growth chamber in order to identify the species of residual gas molecules and atoms. The cells with the heated crucibles containing the source material are mounted on flanges at the bottom of the chamber. During the operation of the MBE system a constant As background will be present in the growth chamber due to excess As covering the walls of the chamber and As evaporating from the As cell, constituting a background pressure in the lower 10^{-8} Torr range[1]. The deposition of materials on the substrate is regulated by shutters which are moved into and out of the beam very quickly so that the composition of the deposited materials or the interfaces of layers can be precisely controlled. The main shutter additionally protects the sample surface from unintended growth. It is especially useful during the measurement of the beam flux. The beam flux is directly related to the gas impingement rate and therefore allows for adjustment of material compositions. The beam equivalent pressure (BEP) can be measured by inserting a movable ionization gauge into the growth chamber right in front of the sample surface, which is protected

---

[1] Torr is an old unit commonly used in MBE, with 1 Torr = 1.33 mbar.

from exposure to the material beam by the main shutter. The samples are placed on molybdenum (Mo) blocks which can easily be transferred inside the vacuum system without breaking the brittle samples. The Mo blocks sit on the substrate manipulator which can be rotated. Since perfect flux uniformity cannot be achieved it is useful to rotate the substrate in order to reduce gradients of film thickness. In this way, homogeneous and uniform epitaxial layers can be obtained. In addition, a heater is fixed above the substrate and can be lifted in order to insert and remove the samples. For the growth process it is essential to properly adjust the sample temperature. Therefore, a thermocouple element placed on the heater can be used but will only give an upper limit of the real temperature on the sample surface since the sample is heated from the backside and the heater is at a few millimeters from the sample backside. A more accurate measurement is offered by a pyrometer which detects the thermal radiation from the sample surface. The temperature of the substrate heater and that of the cells is controlled through partial-integral-derivative (PID) controllers. Finally, the equipment for RHEED measurements comprises an electron gun providing the electron beam and a fluorescent screen onto which the diffracted electron beam is projected. The MBE control software is used to set heater and cell temperatures and to operate the shutters.

The buffer chamber allows to store samples under UHV conditions which are better than in the growth chamber with pressures down to the lower 10^{-10} Torr range. In addition, it hinders the contamination of the laboratory environment with As. The buffer chamber is pumped by an ion getter pump and a Ti sublimation pump and the pressure is monitored using an ionization gauge. Two transfer rods are mounted inside the chamber. The horizontal rod is operated through an external magnet and the vertical one is mechanically connected to a stepper motor.

The loading chamber is used to load and bake samples. It is equipped with a turbo molecular pump (TMP) whose exhaust is connected to a scroll pump. The pressure is measured using a cold cathode ionization gauge (Penning type). Since the loading chamber is frequently vented and then pumped again its size is reduced to a minimum in order to keep the pumping time as small as possible. To keep the chamber as clean as possible it is vented with nitrogen from an external supply. The chamber is further equipped with halogen lamps which are controlled by PID-controllers and which can heat the chamber inside above 100°C.

Different cell types are employed depending on the source material used. Common to all is that evaporation of material from the source is based on the *Knudsen* technique, where evaporation occurs as effusion from a thermal enclosure (crucible) through a small orifice [3]. The crucibles are made of pyrolytic boron nitride (pBN) which is a compound of high thermal stability and high purity. In case of Ga and In the crucible is heated by two filaments, one around the body of the cell and a second at the tip of the cell. The first lets the source material melt, the second hinders the formation of metal droplets at the tip of the cell which likely influences the flux rate. The As cell contains only one filament to heat the body but an additional cracker zone is available to decompose tetramers into dimers, if desired. The cracker is heated with a separate filament. The flux from the As cell is controlled by a needle valve which is connected to a step motor which can be operated from the MBE control software. It is the cell temperature that defines the material flux and therefore the growth rate at a given substrate temperature. The flux is time stable and strongly decreases once the source material is almost consumed. Assuming a round shaped orifice the beam flux density F (molecules/cm^2·s) from a cell is given by

$$F = 2.653 \times 10^{23} \frac{pA_{\mathrm{or}}}{L^2\sqrt{MT}} \times f(\theta, \phi) \tag{3.11}$$

with p being the pressure in the cell, A_{or} the area of the orifice, L the distance between orifice and substrate, M the molecular weight and T the temperature. The angular flux distribution is contained in the function $f(\theta, \phi)$ and depends on the geometry of the cell in the chamber. Conical effusion cells are commonly used nowadays since they produce better flux homogeneity at the substrate surface compared to cylindrical cells.

The first step in the reaction path for crystal growth is the adsorption of atoms and molecules from the vapor phase on the substrate surface. Until adsorbed species are built into the crystal as atoms further processes can be observed on the surface including desorption, surface diffusion, island nucleation, attachment to and detachment from islands and steps. Describing these phenomena by conventional equilibrium models, e.g. *Langmuir* model [62], is not suitable as they fail to characterize growth as a kinetic process where a net deposition is possible. Thus, the entire system, i.e. substrate surface with total adsorption and desorption rates, is far from equilibrium. It is however possible to define a spatially localized equilibrium that allows to use the conventional rate theory on a time scale relevant to the system [63, 3]. The probability of adsorption strongly depends on the local configuration of the substrate surface, e.g. number of nearest neighbors or surface roughness. Following *Venables et al.* [64] and *Jackson* [62] the rate of adsorption R_{ad} (molecules/cm^2·s) can be written as

$$R_{\mathrm{ad}} = F \cdot f(x,t) \tag{3.12}$$

where F denotes the flux density and $f(x,t)$ accounts for the local configuration of the substrate surface. The latter is time-dependent since the growth process alters the surface. The desorption rate R_{de} in turn is conventionally defined as

$$R_{\mathrm{de}} = n_1 \nu_{\mathrm{de}} \exp\left(-\frac{E_{\mathrm{de}}}{k_{\mathrm{B}}T}\right) \tag{3.13}$$

with n_1 being the population of adatoms, ν_{de} the attempt frequency and E_{de} the desorption energy. The areal density of adatoms n_1 can be seen as the number of adatoms divided by the number available growth sites. Both values change with time during growth and hence does n_1. The desorption energy is the energy necessary for the adatom to desorb and is equal to the energy lost through adsorption E_{ad}. The attempt frequency is usually on the order of 1-10 THz. At sufficiently high temperatures, the adatoms will only stay on the surface for a short while before they desorp. The residence time during which they can migrate on the surface is given by $\tau_{\mathrm{res}}^{-1} = R_{\mathrm{de}}/n_1$. Diffusion controls the motion of adatoms on the surface and the maximum distance (diffusion length) which they will sample during τ_{res} is $r_{\mathrm{max}} = \sqrt{D\tau_{\mathrm{res}}}$, with D being the diffusion constant. In case of two-dimensional surface diffusion the diffusion constant can be calculated from

$$D = \frac{b^2 \nu_{\mathrm{dif}}}{4} \exp\left(-\frac{E_{\mathrm{dif}}}{k_{\mathrm{B}}T}\right) \tag{3.14}$$

if the activation energy for surface diffusion E_{dif} is known. The attempt frequency ν_{dif} is typically somewhat less than ν_{de} and the average jump distance b is on the order of surface atomic spacing [64].

Growth of a thin film will only occur if the adatoms on the substrate surface can interact with each other to form clusters or islands that eventually coalesce when their density increases. Clusters will form once adatoms meet before they desorp. Provided that $\Delta t = F^{-1}$ is the average time interval between arrival of atoms per cm^2 and $r = \sqrt{D\Delta t}$ being the range of individual excursions, actual configurations of a given number of adatoms can only be sampled if the condition $\Delta t < \tau_{res}$ is fulfilled. This is a requirement for nucleation

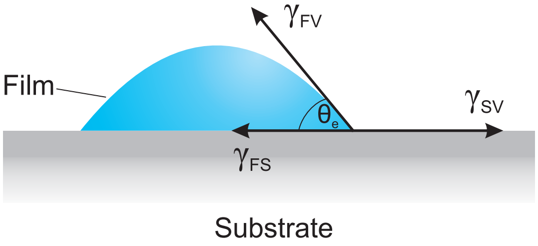

Figure 3.12 Schematic illustration of the *Young*-relation which describes an equilibrium between the surface and interfacial energies.

to start. The physical reason for that process is an attractive force between atoms when they come close to each other. The evolution of adatoms on the surface can be formulated in coupled differential rate equations which can only be solved numerically. Including surface features such as kinks and steps results in very complex models. Such models have been proposed in literature and result in a more precise formulation of kinetic processes on a substrate surface, revealing that the surface structure is of great influence on the growth process itself [62].

The above considerations provide a measure for the real growth of samples. The flux of incoming species (or BEP) and the growth temperature are the two main factors determining the growth characteristics. The temperature will in general define the adsorption and desorption rates as well as the diffusion length and the flux will influence the growth rate. Thus, MBE growth can be controlled by adjusting these quantities. In the case of GaAs growth on GaAs the growth rate is only determined by the incoming flux and not by the growth temperature (for $T_{\mathrm{growth}} < 600°\mathrm{C}$). This infers that the growth is not limited by desorption but rather by the flux of incoming atoms and molecules. Arsenic starts desorbing from the GaAs substrate surface above 350°C and is thus unstable compared to Ga which will not effectively desorb below 750°C [27]. The growth of As-compounds in this work is therefore performed under As-overpressure, meaning a high As-BEP in order to obtain a local equilibrium of desorption and adsorption for As species. The GaAs-GR is then limited by the Ga-flux (or Ga-BEP). The situation is different for the growth of InAs on GaAs. Above 450°C the InAs-GR not only depends on the In-flux but also on the growth temperature since In desorption becomes dominant. At the same time In adatoms can still diffuse on the surface which opens a new possibility to control the material distribution once InAs islands have already formed. In order to investigate such mechanisms it is important to separate the nucleation of islands from diffusion processes which favors higher InAs growth rates, as will be explained in chapter 6.

After having introduced the mechanism of island formation through strain relaxation as well as the kinetic processes occurring during MBE growth it is fruitful to categorize the evolution of a layer during growth from a general point of view. The mode of nucleation and initial growth strongly depend on the bonding between the substrate and the deposited film [65]. Classically, three different growth modes are defined to describe the initial phase of film formation. The classification is based on the balance of surface and interfacial free energy. The energy balance is illustrated in figure 3.12. To start with, it is assumed that the deposited material forms a droplet with a contact angle θ_{e}. At equilibrium, the surface and interfacial energies are balanced so that the droplet is stable. The relation (*Young*-relation) between these energies is defined by

$$\gamma_{\mathrm{sv}} = \gamma_{\mathrm{fs}} + \gamma_{\mathrm{fv}} \cos\theta_{\mathrm{e}} \tag{3.15}$$

Growth mode		Spreading parameter		Layer dimension
Frank-van der Merwe	FM		$\Delta\gamma < 0$	2D
Volmer-Weber	VW		$\Delta\gamma > 0$	3D
Stranski-Krastanov	SK	$d < d_c$:	$\Delta\gamma < 0$	2D
		$d > d_c$:	$\Delta\gamma > 0$	3D

Table 3.3 The three classical growth modes and their characteristics. The FM mode results in layer-by-layer growth, the VW mode in 3D island growth and in the SK mode a change from two-dimensional growth to island growth is observed at the critical thickness d_c. The growth can be characterized by the spreading parameter $\Delta\gamma$.

where γ_{sv} denotes the energy of the substrate-vapor interface, γ_{fs} that of the film-substrate interface and γ_{fv} that of the film-vapor interface. The contact angle then reveals if the film completely wets the surface ($\theta_e = 0$), partially wets the surface ($0 < \theta_e < 180$) or completely dewets the surface ($\theta_e = 180$). At non-equilibrium such as during growth it is rather useful to define a spreading parameter $\Delta\gamma$ in oder to characterize the growth. It is given by

$$\Delta\gamma = (\gamma_{fs} + \gamma_{fv}) - \gamma'_{sv} \tag{3.16}$$

where γ'_{sv} denotes the substrate-vapor interface of a dry surface. This is justified by the fact that adatoms are continuously built into the substrate crystal so that the surface is not at equilibrium with the vapor. $\Delta\gamma$ then determines whether it is energetically more favorable to create a large film-substrate interface combined with a large free film surface or to create a large substrate-vapor interface. Three different growth modes can be identified by analyzing $\Delta\gamma$.

- ***Frank-van der Merwe* mode** ($\Delta\gamma < 0$) Wetting of the substrate as atoms bond to the surface more strongly than to each other. The epitaxial film grows layer by layer like in the growth of GaAs on a GaAs substrate.

- ***Volmer-Weber* mode** ($\Delta\gamma > 0$) Opposite situation where atoms bond more strongly to each other than to the substrate. Once the deposition of atoms on the surface has started, small clusters directly nucleate on the substrate surface. With continuing growth, these clusters grow into islands [3]. These islands eventually coalesce if enough material is deposited.

- ***Stranski-Krastanov* mode** (transition from $\Delta\gamma < 0$ to $\Delta\gamma > 0$) Initially, a thin wetting layer grows in a layer-by-layer mode. After a few monolayers the sign of $\Delta\gamma$ switches from negative to positive, implying that it becomes energetically more favorable to increase the substrate-vapor interface by forming islands. This situation is encountered in the growth of InAs on (1 0 0) GaAs substrates.

The change of the growth behavior in the *Stranski-Krastanov* mode can be characterized by the critical thickness d_c upon which islands start to form. The value of d_c depends on the growth temperature and is found to be about 1.7 ML at 500°C. The introduced lattice-mismatch combined with an increase of strain energy during growth are the driving forces for QD formation in the InAs/GaAs system used in this work. The main characteristics of the three growth modes are summarized in table 3.3 and illustrated in figure 3.13.
The 2D→3D transition in the SK mode is accompanied by a change in the surface morphology. Since RHEED is very surface sensitive it is possible to observe the transition

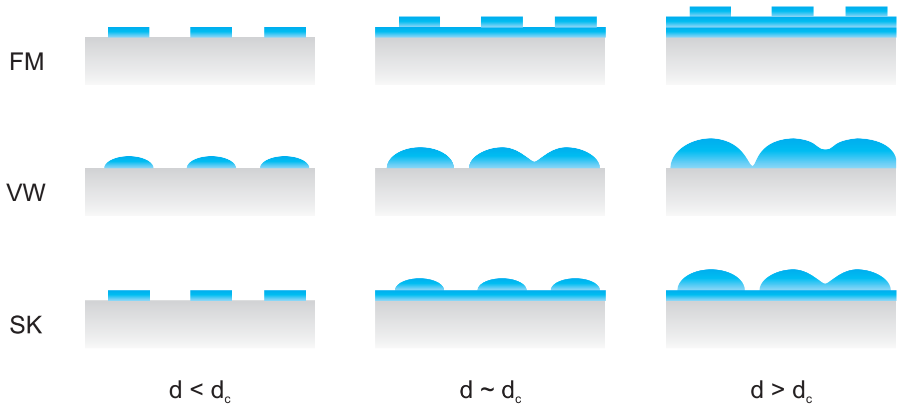

Figure 3.13 Illustration of the three classical growth modes depending on the film thickness. Islands start to form above the critical thickness d_c in the SK mode. If sufficient material is deposited islands eventually coalesce in the VW and in the SK mode.

from flat film to island growth and therefore allows to control the growth process in general. The diffraction pattern of the reflected electron beam strongly depends on the atomic surface configuration on the one side and on the overall surface morphology on the other side. The atomic surface configuration is guided by the fact that atoms at the surface have less partners to bind with. Their dangling bonds are energetically not favorable. Thus, in order to minimize the energy of the near-surface region of the crystal, the group III and group V atoms rearrange themselves in a regular fashion which exhibits long range order. Each ordered arrangement of the near-surface region is known as a surface reconstruction [60]. The outer few planes can uniformly relax towards the bulk with only slight distortions of the bond lengths or the surface structure can change. In the second case there can also be a symmetry change, though the surface will always have lower symmetry than the bulk [61]. The reconstructed surface is tested in RHEED where a specific periodicity will lead to a related streak pattern. Streaks are observed in contrast to a 3D crystal where spots are found as diffraction results from reflection on a 2D structure. This streak pattern is then modulated with the surface morphology. In case of a flat film, the streak pattern is expected to be very clear and pronounced. The surface reconstruction initially depends on the growth plane and varies with the substrate temperature and the surface termination (As or Ga). In the latter case, growth conditions such as As- and Ga-fluxes influence the resulting surface structure. The growth conditions used in this work lead to the relevant (2×4) reconstruction on the $(1\,0\,0)$ GaAs surface. The reason is the formation of arsenic dimers through pairing of dangling bonds while the 4-fold symmetry is related to a regular dimer vacancy [66]. A clear diffraction is only observed when the incident electron beam is parallel to one of the two periodic alignments. The 2-fold and 4-fold periodicities of the reconstructed $(1\,0\,0)$ GaAs surface are alternately sampled by successively rotating the sample by 90°. The corresponding diffraction patterns are shown in figure 3.14. They were recorded using a CCD (charge coupled device) camera. The integral-order maxima are separated by fractional-order maxima whose number depend on the symmetry. An n-fold symmetry in the given direction gives rise to $n-1$ fractional-order maxima. A slightly rough surface modulates the pattern and would make the streaks appear fuzzy. In the case of InAs islands, the diffraction pattern is modified since the islands act as a 3D scattering volume. This will, as for a bulk crystal, lead to a spotty diffraction pattern. However, the islands do not fully cover the surface and hence the InAs wetting layer contributes to

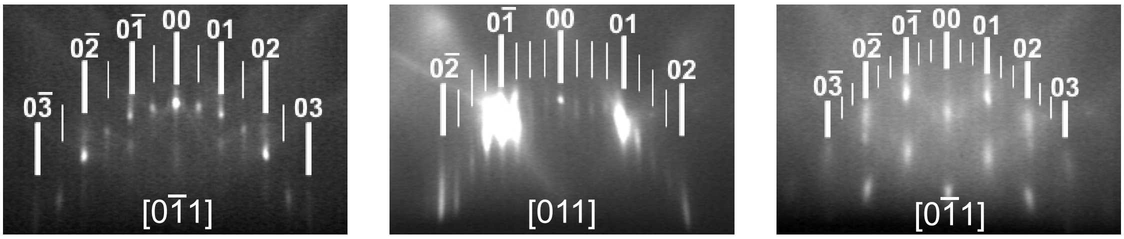

(a) (b) (c)

Figure 3.14 Diffraction pattern of the reconstructed (1 0 0) GaAs surface. A streaky pattern is observed implying a smooth surface. The 2-fold and 4-fold symmetries of the (2 × 4) reconstruction are observed in (a) and (b), respectively. The diffraction pattern after InAs island formation on a (1 0 0) GaAs surface is shown in (c). The spots indicate the occurrence of the islands whereas the faint 3-fold symmetry results from the reconstruction of the (1 0 0) InAs wetting layer.

the diffraction by superimposing streaks from reconstruction. Besides the spots the 3-fold symmetry is observed in figure 3.14 (c).
It is possible to explore the growth dynamics of MBE by monitoring temporal variations in the intensity of various features in the RHEED pattern [61]. In a layer-by-layer growth mode, as for GaAs growth on a (1 0 0) GaAs substrate, investigating the intensity of the specular beam will show a variation of its intensity depending on the coverage of the substrate surface. This allows for the calibration of the GaAs growth rate. The InAs growth cannot directly be calibrated in the same way since the formation of islands starts at a coverage of around 1.7 ML so that intensity oscillations over several monolayers cannot be observed. The 2D→3D transition of the growth can be monitored by RHEED because it gives rise to a change in the diffraction pattern from streaky to spotty but it only gives a lower limit of the InAs GR. The reason is, that the transition is not as sharp as to be able to predict a precise growth rate. As a way out, GaInAs films can be grown on a GaAs substrate with the desired In-flux but a much higher Ga-flux so that layer-by-layer growth is maintained. In this case, the common RHEED intensity oscillations are present so that the InAs-GR can be deduced from the difference of the GaAs-GR to the GaInAs-GR.

Summary

The main aspects of sample fabrication relevant to this work have been introduced. It was shown in which way substrates can be patterned in order to provide defined nucleation sites useful for site-selective growth of InAs quantum dots. The patterning starts off with electron beam exposure in which nanostructures are defined in an electron sensitive resist. These structures are then transferred into the underlying GaAs substrate by controlled etching. While wet chemical etching produces crystallographic profiles, anisotropic hole profiles can be obtained by dry etching. The samples have to be thoroughly cleaned after lithography before they can be transferred into the MBE system. Molecular beam epitaxy is then used to grow InAs islands on top of a thin GaAs buffer layer in a controlled way. Many experimental parameters enter in lithography as well as in the growth process and needed to be constantly adjusted and optimized throughout this work. A comprehensive overview of the numerous steps in the sample fabrication process and their order is given in figure 3.15.

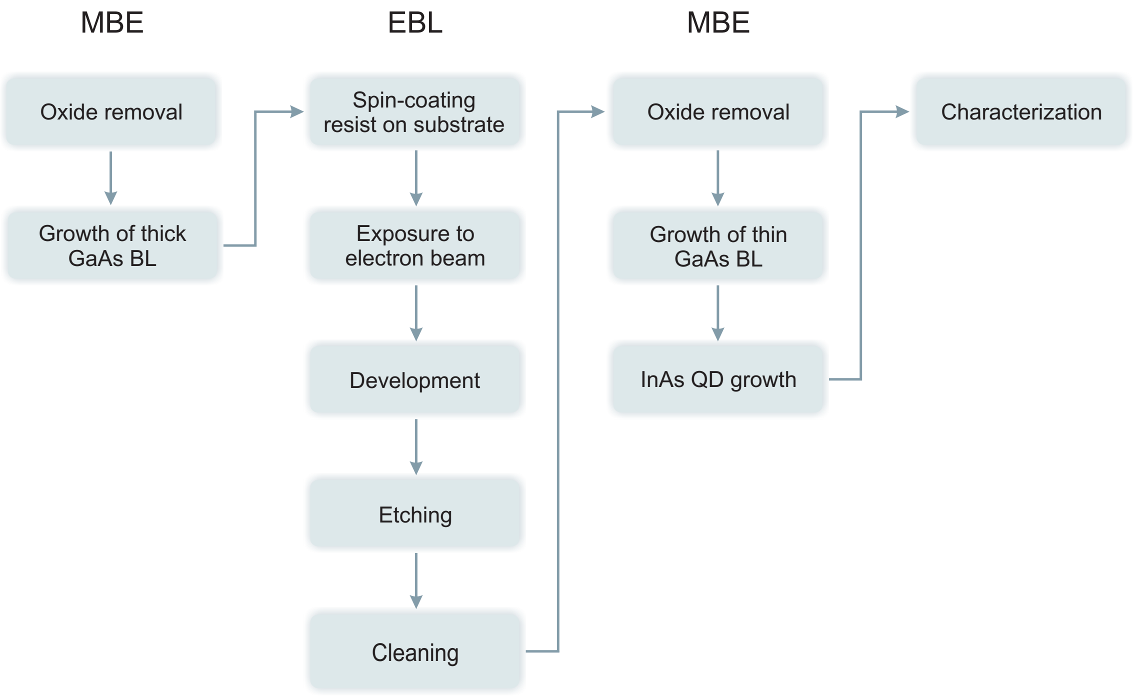

Figure 3.15 Process chain of sample fabrication including the main steps. The first part describes an MBE process, the second the EBL procedure and the third MBE growth of QDs. Afterwards, the samples are characterized with different methods.

4 Improving substrate preparation for site-selective growth

For a successful growth of positioned InAs quantum dots by molecular beam epitaxy it is essential to prepare clean and defect free sample surfaces. Two steps are crucial in this context, namely the cleaning of the samples prior to entry into the UHV of the MBE system and the oxide removal before QD growth. During the course of sample preparation by electron beam lithography the substrate surface is exposed to several materials such as the polymer resist, etch solutions or organic solvents. Residues of these chemical compounds will affect the growth process and possibly hinder the formation of an epitaxial layer. Effective and efficient measures to verify the surface quality before growth are not available so that a cleaning procedure has to be developed which reliably removes any contamination before transferring the samples into UHV. Unless special passivation techniques are used, a native oxide will readily form on the GaAs surface by exposure to air which has to be removed before an epitaxial match of the GaAs crystal of the substrate with the deposited material is possible. However, simply heating the patterned samples to a temperature of 580° or higher, as in conventional thermal deoxidation, harms the defined nanostructures which undergo structural transformation at elevated temperatures. Therefore, a low temperature deoxidation technique has to be found which preserves the shape of the sensitive nanostructures. These two aspects concerning the substrate preparation will be addressed in this chapter.

4.1 Surface treatment to reduce organic contamination

Positioning of QDs in a deterministic way relies on good control of the nucleation sites. These sites are defined by EBL. Small holes on the substrate surface locally increase the growth rate which leads to defined nucleation of QDs below the overall critical thickness for QD formation on a flat substrate. A successful demonstration of this mechanism is depicted in figure 4.1 where atomic force microscopy (AFM) images of an ordered QD array are shown. Figure (b) is a magnification of (a). A patterned substrate was overgrown with a 16 nm thin GaAs buffer layer (BL) on top of which 1.7 ML of InAs was deposited. The images reveal InAs QDs which are arranged on a square grid with a separation of 250 nm between individual sites. A predominant nucleation of double dots is found which is related to a change of the hole shape during BL growth. The QDs are aligned in the [1 1 0] direction. In addition to the ordered QD array a few QDs have also nucleated between the defined sites. These sample features will be analyzed in more detail in chapter 5. The focus is laid on defects which become apparent after the sample fabrication. The white circles in (a) indicate large areas where the GaAs BL is not closed. An increased number of QDs nucleating at the rim of these defect holes is observed. The additional defect holes were not defined during EBL and thus interfere with the attempt to deterministically position QDs. The origin of these defects was investigated and measures were taken in order avoid them.

The lower AFM profile shown in (b) indicates that the holes are less than 16 nm deep.

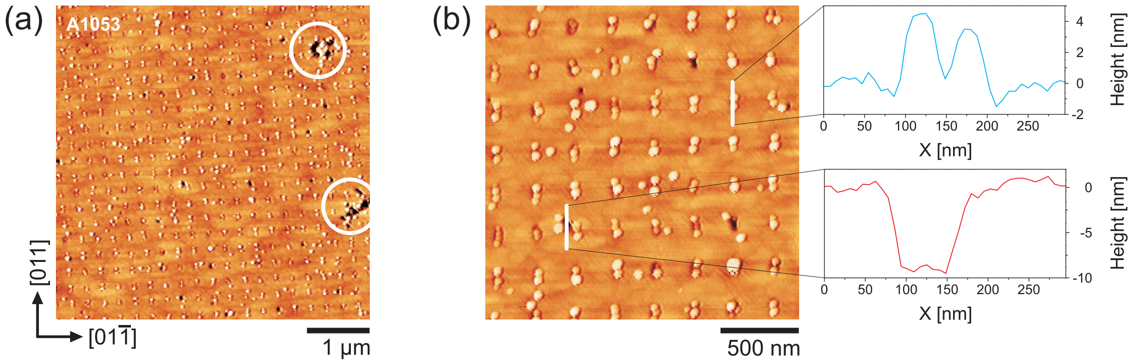

Figure 4.1 AFM images of an ordered InAs QD array. Figure (b) is a magnification of (a). The separation between defined sites is 250 nm. QDs predominantly nucleate as double dots, as suggest by the upper height profile. Besides the nucleation sites defined in EBL additional holes are observed, see white circles in (a) and lower height profile in (b). These interfere with the attempt of deterministic QD positioning. The z-scales of (a) and (b) are 19.9 nm and 17.2 nm, respectively.

This suggests that the origin of the defect holes seems to be at the regrowth interface. Further confirmation is given by a transmission electron microscopy (TEM) analysis of a similar sample which was additionally covered with a 90 nm thick GaAs capping layer (CL). The TEM image in figure 4.2 shows the profile of a defect hole which was found on this patterned sample. The different layers of the structure are visible and indicated, starting with the GaAs substrate and followed by the GaAs BL, the InAs layer and the final GaAs CL. The regrowth interface is clearly seen. The defect hole develops from the pre-structured surface upward in the GaAs BL. A local change on that surface inhibits the proper regrowth of GaAs. InAs, however, then nucleates inside the hole, which is finally covered by the final capping layer. The GaAs sidewalls of the defect hole exhibit a curved shape with increasing thickness of the GaAs BL at larger distances from the hole center. This implies that GaAs does not preferably nucleate in the vicinity of the defect hole, probably due to strain accumulated at the surface of the GaAs BL facing the site where nucleation of GaAs is hindered. In general, two factors can account for the occurrence of the described defect holes. First, insufficient surface cleaning after the lithography process could cause local organic contamination of the sample which also impacts the GaAs growth. Second, incomplete removal of the native oxide could leave residual oxide compounds on the surface which affect the proper GaAs regrowth. The latter possibility is not very likely since complete deoxidation is observed on un-patterned samples leading to closed epitaxial films. Nevertheless, it would be possible to test this hypothesis by further optimizing the oxide removal recipe to ensure complete deoxidation. The insufficient surface cleaning is more likely to be responsible for the occurrence of defect holes and was investigated in detail.

Cleaning samples after EBL comprises several steps. First, the resist needs to be removed which is done with an adequate remover. Thereafter, the sample is cleaned with different solvents (trichlorethylene (TCE) or n-methyl-2-pyrrolidone (NMP), acetone, isopropyl alcohol (IPA), methanol) in a heated bath. In order to aid the cleaning process an ultrasonic cleaner can be employed. Finally, the samples are rinsed with bi-distilled water. Organic contamination can therefore either stem from the chemicals or from the resist used in EBL as it contains organic compounds. Especially the high temperature during dry-baking of the resist results in a high stability of such compounds against solvents. Critical steps of

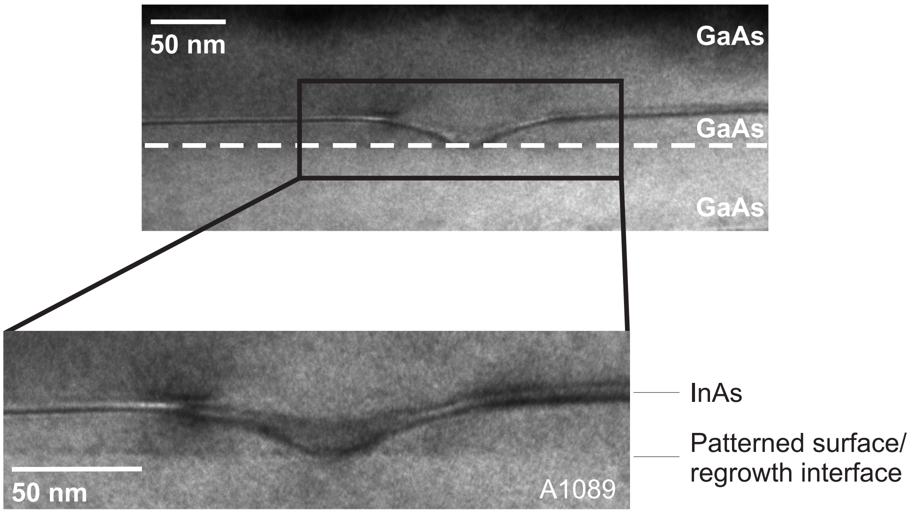

Figure 4.2 TEM images showing the profile of a hole emerging from the regrowth interface after sample processing. After EBL the sample was overgrown with a GaAs BL which is not closed in the center. Residual organic compounds from the resist could account for the creation of such a defect hole. InAs and a GaAs CL were grown on top of the BL. The different layers of the sample are marked.

the cleaning procedure are depicted in figure 4.3. The sample in (a) was cleaned according to the procedure described above but without ultrasonic bath. A lot of contamination (appearing as white particles) with larger and smaller particles is observed in the AFM image. If the samples are cleaned in a heated ultrasonic bath, the amount of contamination is reduced, as seen in (b). A few particles remaining on the surface are directly observed but more residues are still present on the surface, as the lateral force microscopy image in (c) reveals. The lateral force image was recorded in an AFM with lateral force mode (LFM) and displays the lateral force on the AFM tip when scanning a particular area. The friction of the tip, and hence the lateral force, depends on the material currently scanned so that different materials will lead to different forces. This allows to produce a material contrast. The image in (c) is a magnification of the area bound by the white square in (b) and exhibits gray, stain-like residues which are not seen in the height image, probably because they are only of ML height. A positive effect of ultrasonic cleaning is thus only observed for larger particles in the nanometer range but this alone is not successful in fully removing all contaminants. A more effective way has to be found which directly works on organic molecules.

The fact that ultraviolet (UV) light causes chemical changes has been generally known for a long time. Commonly known manifestations are the fading of fabric colors and changes in human skin pigmentation (i.e., sun tanning) upon exposure to sunlight [67]. In particular, its effect on organic compounds was demonstrated when *Bolon* and *Kunz* used UV light to depolarize various photoresist polymers [68]. Therefore, the power of a cleaning process involving UV radiation was investigated with respect to its efficiency in removing the remaining contaminants. It utilizes UV source that emits radiation at the wavelengths of 184.9 and 253.7 nm [69]. Molecular oxygen (O_2) absorbs the shorter wavelength and is dissociated. The resulting atomic oxygen can bond to surrounding oxygen molecules, subsequently forming ozone (O_3). Ozone is then again decomposed by the longer wavelength so that atomic oxygen is constantly produced. Atomic oxygen is a strong oxidizer. The 253.7 nm radiation dissociates or excites organic molecules. These

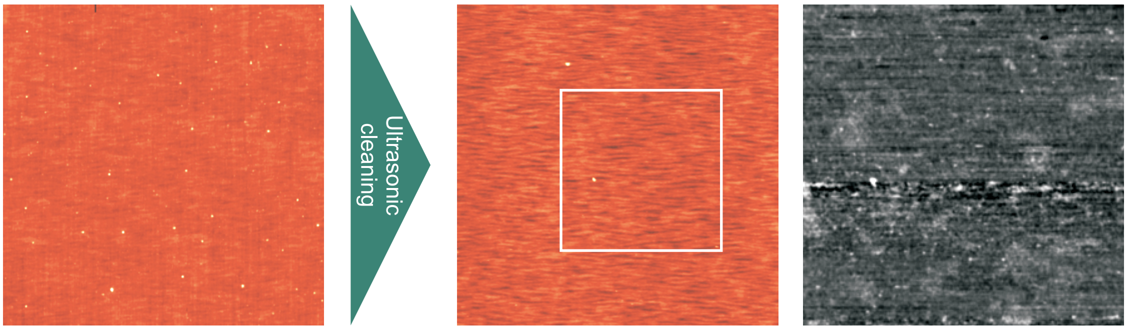

(a) (b) (c)

Figure 4.3 AFM image of samples after cleaning. A resist coated sample was cleaned after EBL using a remover and organic solvents. A lot of contamination remains on the substrate (white particles), as seen in (a). After performing the cleaning in an ultrasonic bath less particles are found, (b), but the lateral force image in (c) allowing for chemical contrast proves that residues, possibly of ML-height, are still present on the surface. The z-scale of the height images in (a) and (b) is 20 nm and 27 nm, respectively.

react with the atomic oxygen and form simpler, volatile compounds that desorb from the surface. The reaction of the atomic oxygen with excited or dissociated contaminant molecules is believed to be responsible for the cleaning action of UV/ozone [70].

The basic setup of a working UV/ozone cleaner is simple. It comprises a low-pressure mercury lamp that emits UV light at the two relevant wavelengths in an enclosure that contains the aggressive ozone. Additional oxygen can be supplied and the sample might be heated in order to amplify the reactions. Since commercial systems are quite expensive, a UV/ozone cleaner was designed and constructed by me with the help of a technician. The complete system is depicted in figure 4.4. The chamber in which the samples are exposed to UV light and O_3 is made of stainless steel. The chamber top is tightly fixed to the bottom by screws and can be taken off in order to insert the samples. O_3 is toxic and although it usually decomposes within one hour the possibility of exposure should be reduced to a minimum. The rubber gasket between top and bottom ensures that O_3 does not escape from the chamber into the ambient air during the cleaning process. The O_3 generating low-pressure mercury lamp emits UV light with strong intensity at the wavelengths 184.9 and 253.7 nm. A second UV lamp is built in for safety reasons. The setup of this lamp is similar to the first but the glass used to form the tube is different. While fused quartz glass (used in the first lamp) is transparent for both wavelengths, high-silica glass is opaque for the lower wavelength. As a result, the generation of ozone is inhibited. The longer wavelength, on the other side, decomposes ozone so that the second UV lamp can be used to destroy ozone remaining in the chamber after the cleaning step. The toggle switch is used to choose the UV lamp that is switched on by the main switch. Each cleaning procedure in which the first UV lamp generates ozone contains an ozone destruction step at the end in which the second UV lamp is used. In order to create reproducible cleaning conditions inside the chamber pure O_2 can be fed through the gas inlet on the right. The supply of O_2 increases the efficiency of the cleaning process since more ozone can be generated. The oxygen flow is manually controlled by a flow meter (maximum 1 l/min). Excess gas possibly containing ozone can leave the chamber through the outlet on the left which is connected to the exhaust air system of the laboratory. The samples are placed on a cylindrical stage in proximity to the ozone generating UV lamp. The height of the stage can be adjusted to optimize the cleaning since the efficiency of the

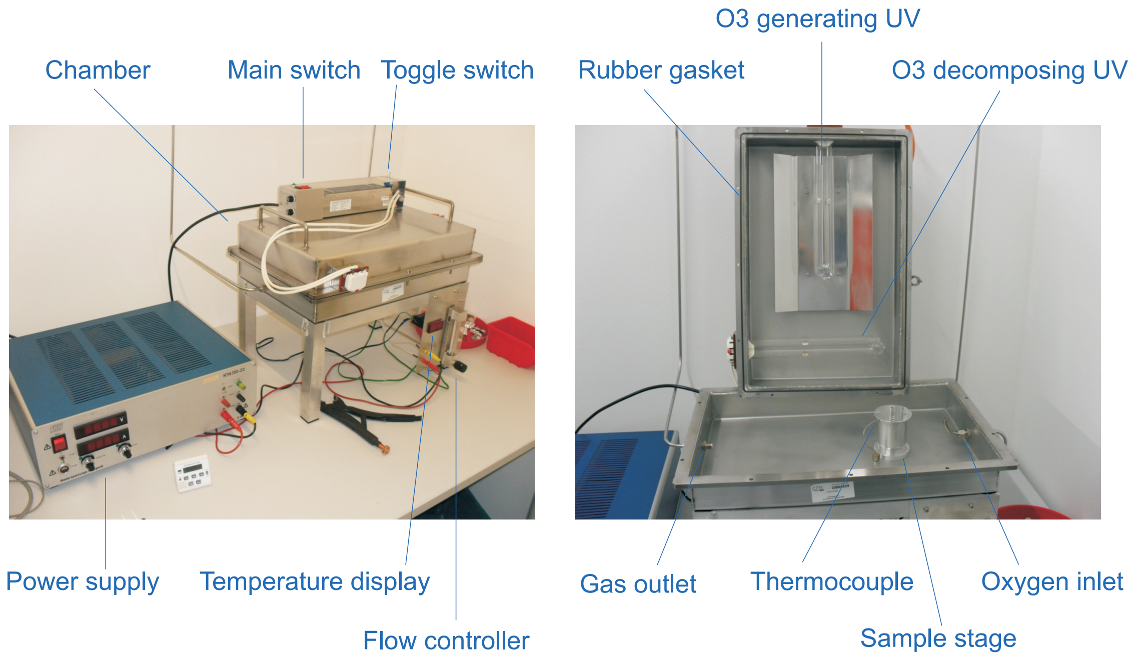

Figure 4.4 Self-built UV/ozone cleaner for the removal of organic residues from EBL. The left image shows the closed chamber, the right image the open chamber. The main components are labeled.

process depends on the distance between the sample and the ozone generating source [67]. The stage is hollow so that a halogen lamp can be placed below the sample in order to heat it. The temperature of the lamp is adjusted by setting current and voltage (maximum 12 V) at the power supply. A thermocouple element at the top of the stage measures the temperature whose value is shown on a digital display.

Each UV/ozone cleaning consists of three steps. In step one, the sample is heated to the desired temperature while the chamber is already supplied with molecular oxygen. In the second step, the ozone generating lamp is switched on so that the substrate surface is cleaned. At the end, the first UV lamp is switched off and the ozone destroying lamp is activated while oxygen is still supplied. Then, the sample can be removed and prepared for loading into the MBE system. The most important process parameter is the cleaning duration, but others, such as the substrate temperature, the oxygen flow or the distance between sample and UV lamp, have to be considered as well when optimizing the UV/ozone cleaning. The effect of UV/ozone cleaning is displayed in figure 4.5. Three samples of same initial conditions were patterned using EBL and subsequently cleaned for 30 s, 60 s and 600 s in the UV/ozone cleaner with continuous oxygen supply. A fourth sample, which was not cleaned, is shown as reference. Contamination appears in the AFM images as white particles between the pattern consisting of holes separated by 500 nm. A gradual reduction of residual particles is observed with increased cleaning time. Not only does the number of particles decrease but also does their height. A statistical analysis in which the surface roughness and maximum height amplitudes are extracted from the AFM height data confirms the effective cleaning. The results are summarized in table 4.1. The roughness of the surface between the holes was measured. The root mean square (RMS) roughness was calculated for the spaces between each two columns of holes and then between two each lines of holes (holes were excluded in both cases) and finally averaged. The height maxima which correspond to the biggest particles were extracted in the same

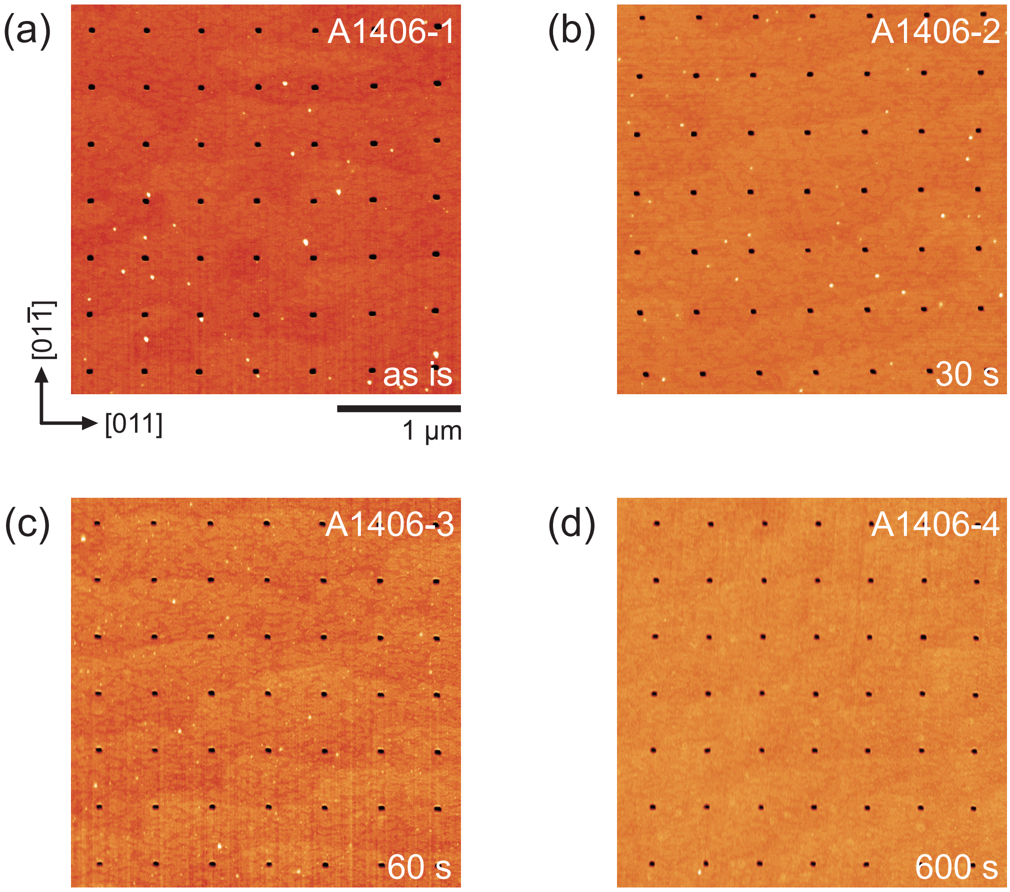

Figure 4.5 AFM images of samples after UV/ozone cleaning. All samples are of the same size and orientation, as exemplified in (a). Four similar structures were defined by EBL on sample A1406 which was divided into four pieces before UV/ozone cleaning. For reference, the sample in (a) was not cleaned. The samples in (b), (c) and (d) were cleaned for 30 s, 60 s and 600 s, respectively.

way. The roughness of the surface between the holes constantly decreases with cleaning time and so does the particle height. Essentially, all contamination has disappeared after long enough exposure to UV light and ozone. As a result, the number of defect holes should be drastically reduced resulting in a uniform and flat GaAs BL after regrowth.

One aspect that has been omitted so far is the effect of oxidation. Since atomic oxygen is a strong oxidizer it oxidizes the GaAs substrate on the surface. It has been found that the oxide formed during UV/ozone cleaning is usually not much thicker than a few ML [69]. This has to be considered for later MBE growth as the surface oxide has to be removed before the actual growth. In order to end up in a comparable situation the oxide layer of the samples (no matter how thick it actually is) can be etched away right before entering the samples into the MBE system.

An alternative method to remove residual organic contamination was applied at a later stage of this work as a new device, a so called plasma asher, became available. In this case, atomic oxygen is provided through the formation of an oxygen plasma. Plasma ashers are routinely used in semiconductor industry and require more complex design. Plasma ashing offers a cleaning efficiency which is comparable to the use of UV/ozone. The main reason to switch to the plasma asher was to optimize the process sequence of sample fabrication. The cleaning was tested and optimized as in the case of UV/ozone and lead to similar

Sample	Cleaning time [s]	RMS roughness [nm]	Height maximum [nm]
A1406-1	0 s	0.389±0.086	13.6±5.6
A1406-2	30 s	0.264±0.034	7.4±1.9
A1406-3	60 s	0.258±0.014	4.8±1.1
A1406-4	600 s	0.255±0.014	3.2±1.9

Table 4.1 Statistical analysis of the degree of contamination. The RMS roughness and the particle height maxima were extracted from the AFM images of figure 4.5 and listed with respect to the cleaning time. The sample labels correspond to those of the AFM images.

results. The oxidation effect during plasma ashing is stronger than during UV/ozone cleaning. Furthermore, the oxygen plasma contains oxygen ions which impinge on the surface. Their kinetic energy is rather low but their impact on the electronic properties of the final structure remains to be studied.

4.2 Structure sensitive oxide removal

Once the samples are cleaned and transferred into the MBE system the surface oxide has to be removed before the actual growth begins. Different deoxidation techniques are commonly used in MBE. The simplest is thermal deoxidation in which the samples are heated to about 580°C and kept at this temperature until all oxide compounds have desorbed from the surface. The most stable oxide compound is Ga_2O_3 which is decomposed at the given temperature into the more volatile Ga_2O through the reaction

$$\mathrm{Ga_2O_3} + 4\mathrm{GaAs(bulk)} \rightarrow 3\mathrm{Ga_2O} \uparrow +2\mathrm{As_2}\ (\text{or } \mathrm{As_4}) \uparrow \tag{4.1}$$

after which Ga_2O readily desorbs [71]. The GaAs in this reaction is consumed from the substrate which is problematic in the case of site-selective QD growth. Surface GaAs used to transform the stable oxide into the volatile compound locally changes the material distribution. As a consequence, pits can emerge which interfere with the lithographically defined holes at the attempt to guide the QD nucleation [72]. Besides this, another disadvantage arises in thermal deoxidation due to the high temperature. Fine nanostructures on the GaAs surface might undergo structural transformations at high temperatures because of material redistribution. This was observed for stripe patterns which were kept at elevated temperature, i.e., annealed for a certain amount of time [48]. The result is depicted in figure 4.6. Whereas the degradation of the pattern is not that strong at 500°C a severe structural change is observed for the stripes at 580°C. The trenches become much shallower and local mounds form at the bottom. Conventional thermal deoxidation is usually performed for 20 min or more so that even stronger degradation can be expected in this case. As shown in chapter 2, the shape of the hole and therefore its curvature has an influence on the QD nucleation. In order to contain the shape of the defined nanoholes it is therefore advisable to not heat the sample above 500°C for an extended amount of time.

As a consequence, structure sensitive deoxidation requires lower temperatures than necessary for thermal deoxidation. One possible mechanism is the conversion of stable Ga_2O_3 by exposure to an atomic hydrogen (H) flux at a substrate temperature between 400°C

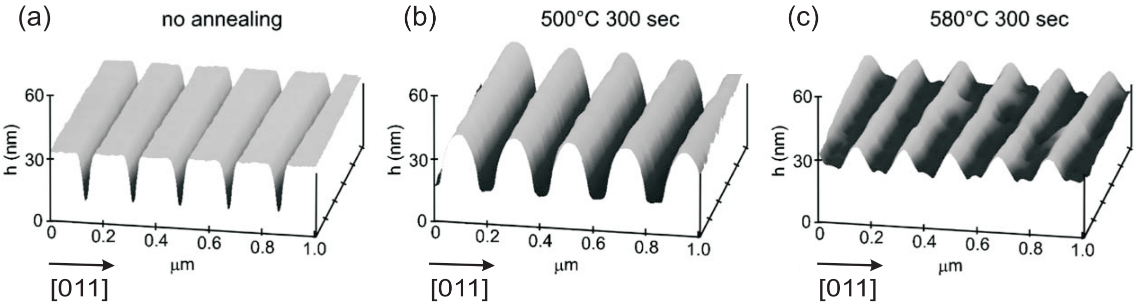

Figure 4.6 AFM images of GaAs stripe patterns after (a) no annealing, (b) annealing at 500°C and (c) annealing at 580°C for 300 s. This stripe pattern is sensitive on annealing and changes its shape depending on the temperature [48].

and 500°C. The stable surface oxide is reduced by the reaction

$$Ga_2O_3 + 4H \rightarrow Ga_2O \uparrow + 2H_2O \uparrow \tag{4.2}$$

leading to a clean, undamaged oxide-free surface [72]. Atomic hydrogen can be provided from a hydrogen cracker cell mounted to the MBE. Possible risks for the substrate surface result from contamination during the hydrogenation process and pattern degradation if the H dose is not carefully controlled. As the MBE system used in this work is not equipped with a hydrogen cracker cell this method of deoxidation could not be applied. Looking back at equation 4.1 it is evident that only Ga of the GaAs compound is required to convert the Ga_2O_3 into Ga_2O. Therefore, a different approach to initiate this conversion reaction at lower temperature is found in the exposure of the surface to a small Ga flux from a molecular beam. In this case, the above reaction would change into

$$Ga_2O_3 + 4Ga \rightarrow 3Ga_2O \uparrow \tag{4.3}$$

which was first proposed by *Asaoka et al.* in order to reduce surface pitting [71]. Ga-assisted deoxidation can be readily applied in the growth chamber of the MBE system since no special equipment is needed. At the absence of an As_4-background the sample is exposed to a low Ga-flux of about 1 ML/min in several cycles at a substrate temperature of 480°. Breaks of 30 s are introduced after each exposure of 30 s in order to let the newly formed Ga_2O desorb from the surface. The progress of deoxidation can be monitored by RHEED where a diffuse pattern from the oxide will effectively turn into a regular pattern from the reconstructed GaAs surface once all oxide is removed and provided that the original GaAs surface was flat. The amount of Ga provided during deoxidation depends on the thickness of Ga_2O_3. The thickness of the oxide, in turn, depends on the amount of time the sample is exposed to air as well as on the type of sample preparation prior to growth. The oxide of the GaAs surface being exposed to air at room temperature grows logarithmically with time as $d_{\mathrm{ox}}(t) \approx 6 + 6 \log t$ so that a 2 nm thick oxide layer is obtained after one hour at air [73, 72]. Additionally, oxide growth is observed during the sample cleaning by either UV/ozone or plasma ashing. To guarantee a defined and reproducible surface composition the samples can be etched wet chemically right before the transfer into the MBE system in order to remove all oxide compounds. Diluted hydrochloric acid (HCl) is used and the samples are quickly loaded into the loading chamber after etching and pumped to vacuum. Thus, the amount of Ga needed for the deoxidation should not vary too much. Insufficient supply of Ga results in remaining oxide compounds which disturb the proper overgrowth of a GaAs BL. Excess Ga will accumulate in Ga droplets on the

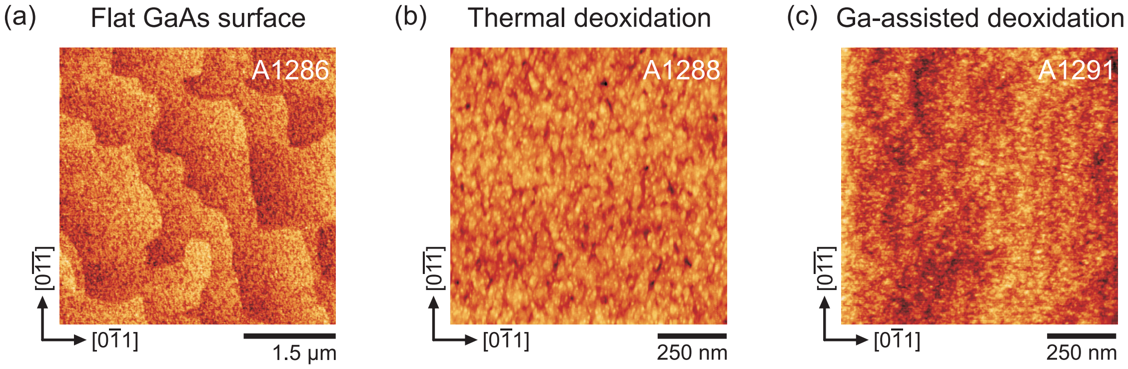

Figure 4.7 AFM images of samples after oxide removal. The sample in (a) did not undergo deoxidation and shows a flat GaAs surface as a reference. Monoatomic steps are observed. The oxide was removed thermally in (b). Monoatomic steps are hardly observed and small pits appear on the surface. Ga-assisted deoxidation was used in (c) in which the monoatomic steps survive. The z-scales are 1.6 nm, 4.1 nm and 1.7 nm in (a), (b) and (c), respectively.

oxide free surface and is eventually consumed during BL growth. However, the additional Ga possibly accumulates at the bottom of the defined nanoholes, thus changing their shape and infilling them [74]. With respect to controlled QD nucleation this situation is to avoid. A slight flattening of the nanohole profile during Ga-assisted deoxidation is tolerable as long as the shape is not fundamentally altered. The advantages of Ga-assisted deoxidation are obvious. The method works at low temperature, thus avoiding surface pitting and the deposition of Ga does not create any electronic defects. Good control of the depoisted Ga amount is important to maintain the shape of nanostructures but process optimization and process monitoring by RHEED are effective measures for the complete deoxidation while maintaining the pattern structure.

The successful application of Ga-assisted deoxidation is demonstrated in figure 4.7. Two samples were prepared with initially flat GaAs surface by growing a thick GaAs layer on a new GaAs wafer. The samples were kept at air for one day and then transferred back into the MBE system in order to remove the surface oxide. Afterwards, the sample surface was analyzed using an AFM. The flat GaAs surface before deoxidation is characterized by the observation of monoatomic steps, as in (a). These do not survive thermal deoxidation during which pits are formed at the surface, as observed in (b). The sample was kept at 580°C for 20 min. The survival of monoatomic steps during Ga-assisted deoxidation was reported by *Lee et al.* [75] and is also observed in this work, as suggested by (c). The superior performance of Ga-assisted deoxidation can be quantified by measuring the roughness of the surface in the AFM images. The RMS roughness as well as the maximum height amplitude of the AFM images in figure 4.7 are summarized in table 4.2. The surface oxide of sample A1286 was not removed so that it exhibits a very flat surface with a RMS roughness of 0.177 nm which is even below the value for the surface of a new epi-ready wafer (usually on the order of 0.2 nm). The height values in the observed frame range between -0.8 nm and 0.8 nm, hence $\Delta z = 1.6$ nm. In case of thermal deoxidation, the surface is significantly roughened with small pits occurring on the surface. This leads to the higher RMS roughness of 0.32 nm and a height amplitude of $\Delta z = 4.1$ nm with the surface pits being up to 2 nm deep. Ga-assisted deoxidation results in a surface which is almost as flat as before deoxidation with an RMS roughness of 0.185 nm and a height amplitude of $\Delta z = 1.7$ nm. The surface after Ga-assisted deoxidation is flatter than the

Sample	Deoxidation method	RMS roughness [nm]	Δz [nm]
A1286	none	0.177	1.6
A1288	thermal	0.320	4.1
A1291	Ga-assisted	0.185	1.7

Table 4.2 Values of the RMS roughness and the maximum height amplitude depending on the deoxidation method used for the samples shown in figure 4.7.

surface of a new GaAs wafer which demonstrates the advantages of this method. This fact is also reflected by the observation of the 2 × 4 reconstruction of the (1 0 0) GaAs surface in RHEED after oxide removal. When performing thermal deoxidation it is often hard to identify this particular reconstruction as the side maxima are not very distinct because of the rougher surface. As described in chapter 3 the occurrence of a clear reconstruction is an indicator for good, clean and flat surfaces.

Summary

The relevance of surface cleaning and deoxidation in the context of site-selective growth of QDs was discussed. Incomplete removal of organic contamination during substrate cleaning results in defect holes which possibly interfere with the atempt to deterministically position QDs. Such organic compounds can be efficiently removed with the use of UV light and ozone. The approach is easy to implement so that an adequate UV/ozone cleaner could be built. The process was optimized and its performance was demonstrated. Alternatively, an oxygen plasma in a plasma asher can as well be used for the complete removal of organic contamination. When GaAs substrates are exposed to air they will grow a thin oxide layer on their surface. This oxide layer has to be removed before a GaAs BL or InAs QDs can be grown by MBE. Standard thermal deoxidation is not advisable as it is performed at high temperature against which fine nanostructures are not stable with their shape degrading after short time. Additionally, pits form on the surface during deoxidation and compete with defined nanoholes in the selective growth of QDs. A low temperature approach is needed which conserves the nanostructures. Ga-assisted deoxidation was applied at low temperatures revealing surfaces as flat as before deoxidation. Monoatomic steps survive and structural properties of nanostructures are not degraded.

5 Site-selective growth of quantum dots

The first major part of this work was to establish a reproducible procedure to fabricate quantum dots of high structural and optical quality at defined locations. This task is accomplished by employing various technologies such as electron beam lithography including wet or dry etching, UV/ozone cleaning, structure sensitive deoxidation and molecular beam epitaxy, each involving numerous fabrication steps. In the end, each single process step influences the success of quantum dot positioning. The main features of the listed technologies along with relevant parameters were introduced in the previous chapters and improvements in the sample preparation process were demonstrated. Consequently, this chapter focuses on the analysis of complete samples which have run through the whole process chain. Different aspects are emphasized which are relevant in the context of applications. First, the structural properties of positioned quantum dots are analyzed by atomic force microscopy and transmission electron microscopy in order to determine their structural quality. This is accompanied by optical characterization and a statistical analysis of the data. Then, the influence of different patterning techniques on the quantum dot growth is investigated with respect to quantum dot size and distribution. Furthermore, different structure designs are analyzed in terms of their ability to control the quantum dot occupation.

5.1 Structural and optical properties of positioned quantum dots

All samples are prepared and grown according to the following procedure, if not otherwise stated in the text. After patterning of the samples and subsequent thorough cleaning they are entered into the MBE system and pumped to UVH. The baking step in the loading chamber takes about 5 hours (1 hour baking + 4 hour cooling down) before the samples are ready to be further transferred into the growth chamber. The last task before the actual growth begins is to remove the surface oxide. Ga-assisted deoxidation is used as it allows to avoid additional surface pitting and since it is performed at a temperature lower than 500°C severe degradation of the nanohole shape is not encountered. All samples are prepared according to a standard recipe including a final etch step right before loading into the MBE. This allows to perform the deoxidation with a fixed set of parameters. Once the amount of Ga required to completely remove the surface oxide is known, further optimization is not necessary due to the standard preparation procedure which results in a reproducible oxide thickness. Nevertheless, the deoxidation process is monitored using RHEED by observing the emergence of the (2×4) reconstruction of the $(1\,0\,0)$ GaAs surface. The deoxidation is stopped once a clear and streaky reconstruction pattern is obtained. In the case that the oxide layer is thinner than assumed, the deoxidation process can be stopped earlier and if the oxide layer is thicker more Ga will be provided. It takes some experience to correctly interpret the RHEED pattern, especially to recognize the onset of the transition to Ga droplet formation which marks the completion of the deoxidation process. The streaks of the reconstruction become fuzzier at this point, signalizing to stop the deposition of pure Ga. Immediately, the As-valve and the As-shutter are opened in order to establish an As background pressure which is necessary to maintain the stoichiometry between Ga

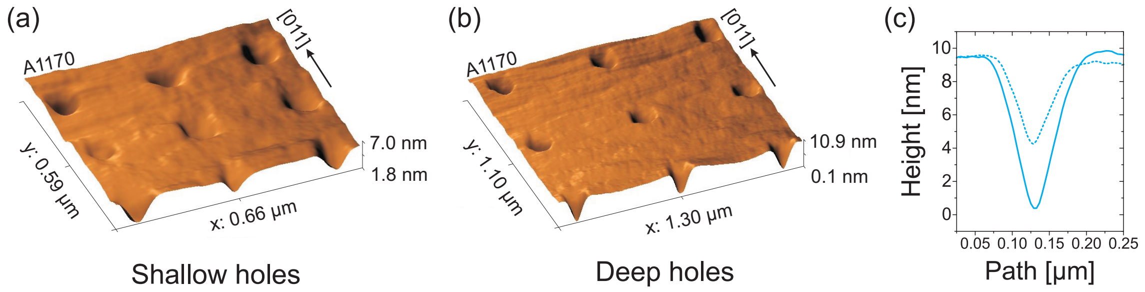

Figure 5.1 AFM images of overgrown holes and representative hole profiles. The lateral size of the holes in (a) was smaller than in (b) which results in enhanced infilling during GaAs BL. Assuming a similar depth prior to growth the holes in (a) become shallower than the ones in (b) after deposition of the BL. This is confirmed by the two representative profiles shown in (c). The dashed line is the profile of a shallow hole in (a) while the solid line is the profile of a hole in (b).

and As at the surface of the GaAs substrate. This is because As already starts to desorb from the surface at a temperature of 350°C [3]. To ensure complete desorption of all oxide complexes from the surface the sample temperature is quickly ramped up to between 550°C and 580°C where the samples are annealed for a few minutes before being cooled to the growth temperature of 500°C [74]. The growth comprises two main steps, the deposition of a thin GaAs BL followed by the growth of InAs QDs. Although the nanoholes have been fabricated with greatest care and most surface sensitive methods, a small degree of surface roughening cannot be avoided. The substrate surface, especially around and inside the nanoholes, is prone to the formation of defects. Growing a GaAs BL therefore reduces the chances that features of the regrowth interface influence the structure of the QDs and hence their properties. A large separation from the regrowth interface and thus a thick BL is advantageous in this respect. An upper limit of the BL thickness is, however, imposed by the depth of the nanoholes as the hole shape is not maintained during growth. The holes become larger and shallower with increasing BL thickness and eventually undergo a shape transformation before they completely infill [72]. As a rule of thumb, the BL should not be thicker than the depth of the nanoholes. Since the hole depth is usually found to range between 20 nm and 30 nm the GaAs BL thickness is limited to the range of 10 nm to 20 nm. Thinner layers are not recommended since they do not provide enough separation from the regrowth interface [72]. The deposition of InAs is started right after completion of the BL. Quantum dots will form in the holes at a layer thickness of less than 1.7 ML, which is the critical thickness for QD formation on planar (1 0 0) GaAs surfaces. Finally, the sample is rapidly cooled down in order to prevent post growth processes such as annealing which affect the QD properties, as demonstrated in chapter 6. The As-valve is closed once the substrate temperature drops below 350°C. Hereupon, the pressure in the growth chamber decreases and reaches a stable value of 1×10^{-8} Torr. The sample can then be transferred back into the buffer chamber where it is stored in UHV. When a set of samples has been grown they are placed in the loading chamber where they are brought to atmospheric pressure in order to take them out of the MBE system.

5.1.1 General structural features

The exact hole evolution during BL growth strongly depends on the lateral size of the hole, as illustrated in figure 5.1. The sample was patterned using EBL where holes of different sizes were defined. Two sets of holes with different lateral size were analyzed.

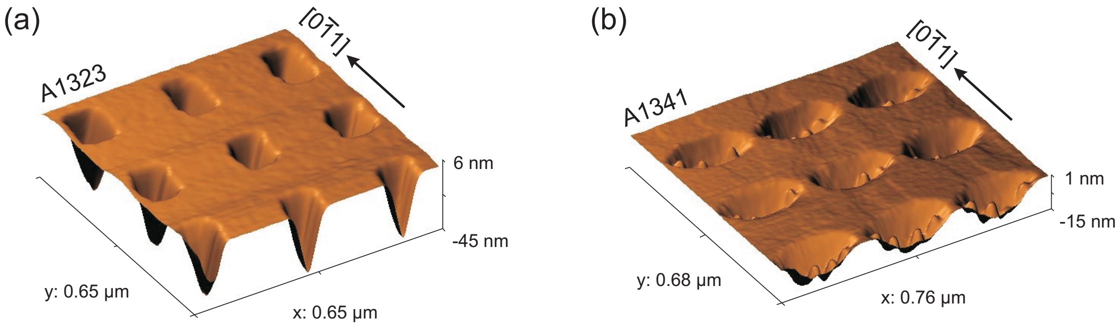

Figure 5.2 AFM images of a hole array after lithography and a comparable array after overgrowth. The holes in (a) exhibit an elongation in the $[0\,\bar{1}\,1]$ direction. This elongation is shifted by 90° due to a shape transformation of the hole during deposition of a 20 nm GaAs BL. 1.8 ML were subsequently deposited leading to selective QD formation inside the holes. Several QDs align in each hole along the preferred direction of hole elongation.

The diameter of the holes in the resist was defined as 70 nm and 90 nm. Wet chemical etching increases the lateral size by about 30 nm so that diameters of 100 nm and 120 nm were found after the pattern transfer, respectively. A 20 nm thick GaAs BL was grown on the pre-patterned substrate followed by the deposition of nominally 1.5 ML of InAs, which was not enough to enforce QD formation. AFM images of the two sets of holes are shown after growth, with the smaller holes being depicted in (a) and the larger ones in (b). The spacings between the holes are 250 nm and 500 nm, respectively. The z-scale is given in each image implying that the smaller holes are shallower than the larger ones. This is confirmed by the two representative hole profiles shown in (c) where the hole depth is measured to about 5 nm and 9 nm for average small and large holes. Smaller holes hence promote infilling during BL growth. Taking into account the influence of surface curvature on the local growth rate introduced in chapter 2 a faster filling of the smaller holes is likely related to a stronger curvature at the bottom of the hole before growth (not shown). This is possible if the initial depth of the holes is assumed to be equal. Then, a smaller diameter leads to a smaller flat base at the bottom of the hole which is equal to a larger curvature. A difference in hole depth can also result during etching for very small hole diameters. In this case, the narrow channel in the resist complicates the transport of etch solution to and etch products away from the etched surface. However, the difference in depth of the above holes is too large to be explained by locally reduced etch rates alone.

Another important observation is made when more InAs is deposited so that QDs selectively form inside the defined holes, as demonstrated in figure 5.2. 1.8 ML of InAs were grown on top of a 20 nm thick GaAs BL. A hole array with a spacing of 250 nm was etched 30 nm deep into the substrate during EBL prior to growth. The AFM image in (a) shows a similar hole array which was etched 45 nm deep into the substrate. The holes were defined as circular structures in the resist but transform into very symmetric rectangular structures during etching. The reason for that was explained in chapter 3 and is related to crystallographic etching. The different etch rates of Ga- and As-terminated facets leads to the observed elongation in the $[0\,\bar{1}\,1]$ direction. This elongation is, however, not maintained during BL overgrowth and subsequent QD formation as the AFM image in (b) reveals. An array of well positioned QDs is found with several QDs in each hole. The alignment of the QDs inside the holes is guided by the hole shape which exhibits an elongation along the $[0\,1\,1]$ direction, thus perpendicular to the original elongation. The hole shape must have

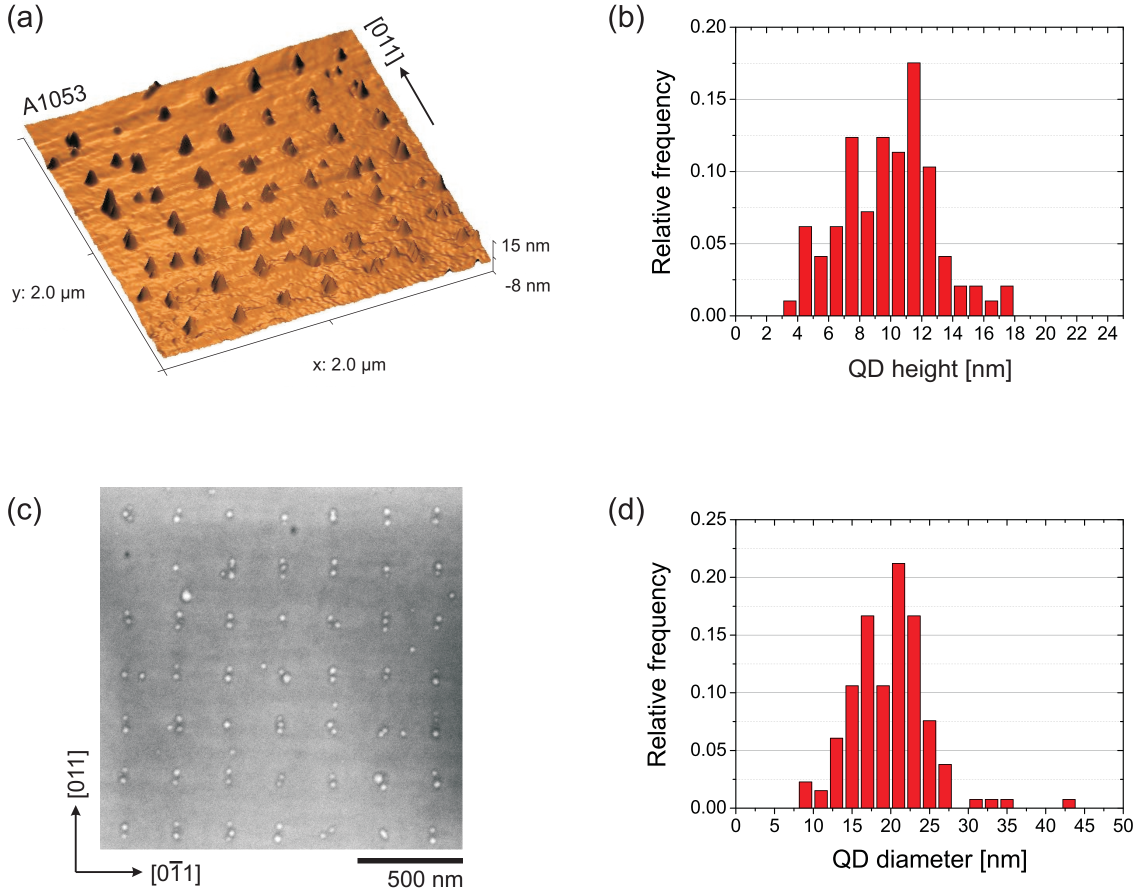

Figure 5.3 Size statistics of positioned QDs on a hole array with 250 nm spacing. The height of the QDs was obtained from AFM height data (a). The corresponding height histogram is shown in (b). The average QD height is 9.8 ± 2.9 nm. The QD diameters were extracted from the SEM image in (c) using the software ImageJ [76]. The diameter histogram is given in (d) and the average QD diameter is 19.8 ± 5.0 nm.

undergone a transformation during BL growth. The enhanced mobility of Ga adatoms in the $[0\,1\,1]$ and $[0\,\bar{1}\,\bar{1}]$ directions leads to a deformation of the holes with an elongation occurring in these directions. The reason for this enhanced mobility is related to the different faces described earlier. A net migration of adatoms away from Ga-terminated facets towards As-terminated ones is observed which then leads to the change in the elongation of the hole.

The size of positioned QDs is of interest because it influences their optical properties. Larger QDs will exhibit a lower confinement energy, as described in chapter 2. The size and therefore the emission wavelength of self-assembled QDs grown on planar substrates can be controlled by adjusting the growth parameters. The indium content of the QDs is a second parameter influencing the optical properties. It can be varied over a wide range, e.g. by mixing Ga into the InAs layer. The dependence of the optical properties on QD size and In concentration have been intensively investigated in the past [77]. A broad range of values can be accessed depending on the needs for the contemplated application. The QD size uniformity is a critical aspect when thinking of large scale applications which rely on identical QDs. A narrow size distribution is therefore favored. While the random nature of self-assembly inherently produces a certain fluctuation in QD size using nanoholes to guide the QD nucleation offers a way to possibly increase the size uniformity, provided that perfectly uniform hole patterns are available.

The QDs fabricated in this work are designed with the aim to integrate them into resonator structures such as micropyramids or -pillars as well as photonic crystal cavities in the future [14, 15]. In this context, small QDs with strong confinement and emission in the range of 900 nm to 1000 nm are favored. This is assured by depositing pure InAs using rather high growth rates which lead to the formation of small QDs and by using rather high substrate temperatures around 500°C to control the In concentration in the QDs. The lithography systems used for the hole fabrication are not optimized with regard to size homogeneity of structures on the few nm scale. Therefore, a fluctuation in the hole size on the order of 10% could not be avoided. An ordered array of QDs was fabricated in order to determine the size of the positioned QDs in this work. 1.7 ML of InAs were grown on top of 16 nm thick GaAs BL. AFM images can be used to measure the height of the QDs whereas SEM images are more useful to determine the lateral size since the QD diameter observed in AFM images appears large than it really is due to a convolution of the finitely sized AFM tip with the measured QD. Figure 5.3 (a) shows an AFM image of the ordered QD array. The holes are completely infilled which is probably related to the holes being shallower compared to the sample in figure 5.2. The spacing between the nucleation sites is 250 nm and two or three QDs are found in most of the holes. The alignment of multiple dots in the holes along the [0 1 1] direction is similar to the case described earlier and is caused by an elongation of the hole in this direction during BL growth. Few QDs are also found between the holes indicating that the amount of deposited material was too high. The defect holes occurring on this sample could be avoided in later samples by developing an improved cleaning procedure prior to MBE growth, see chapter 4. The corresponding height distribution is depicted in (b) and contains only the heights of the positioned QDs. The average height amounts to 9.8 ± 2.9 nm with the standard deviation being roughly 30%.

The QD diameters were exctracted from the SEM image shown in (c) using the image analysis software ImageJ [76] which allows for a standardized evaluation of particle sizes. and is The average QD diameter is 19.8 ± 5.0 nm with a 25% standard deviation. The corresponding QD diameter distribution is depicted in (d). Not only because of system-dependent growth parameters but also because of frequently overestimated QD diameters resulting from the analysis of AFM images it is difficult to compare these values to those in the literature. To emphasize this fact, the QD diameters were also measured in the AFM image in (a) resulting in a much larger average value of 32.0 ± 12.7 nm. The larger standard deviation is probably due to the fact that less QDs could be measured. In general, it is possible to deconvolute the AFM image if the exact geometry and size of the AFM tip used for the measurement is known. Such a deconvolution was performed for the AFM image in (a) assuming a large tip radius of 50 nm. The resulting average QD size is 26.5 ± 10.3 nm and thus closer to the value obtained from the SEM image. Abbrasion of the tip during scanning might alter its geometry and size. In day to day work it is therefore not very practicable to characterize the AFM tip every time an AFM measurement was performed. The measurements in the SEM images using the software slightly underestimate the real QD value but are probably more reliable than the values extracted from the AFM images.

In order to relate these values to conventional self-assembled QDs the same structure was grown on a planar GaAs substrate. Although the deposited InAs amount of 1.7 ML and the growth conditions were equal to the overgrowth of the patterned sample QD formation was not observed on the flat surface. Small precursor states of 10-20 nm in diameter and 1-2 nm in height were found in AFM images but no regular QDs. This means that the critical thickness of InAs for QD formation was not reached yet implying that its value should

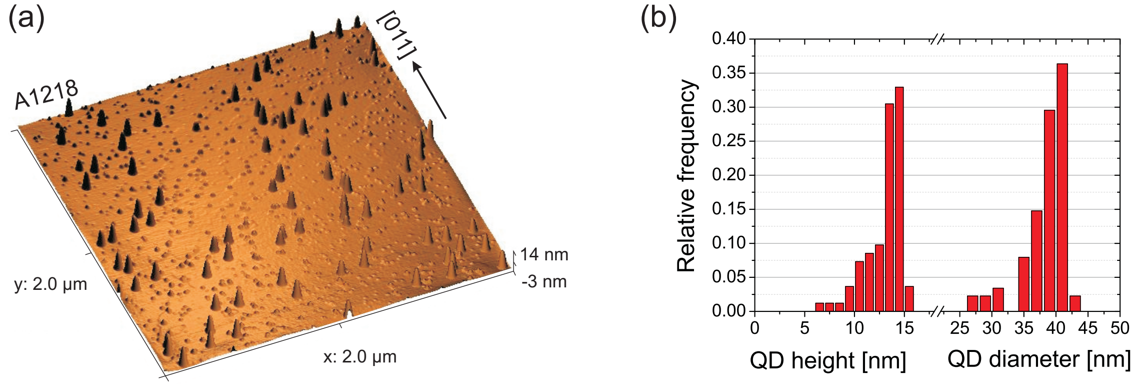

Figure 5.4 Size statistics of random self-assembled QDs for reference. Both QD heights and diameters were extracted from the AFM image in (a). The average QD height is 13.0 ± 1.7 nm and the average QD diameter 38.3 ± 3.9 nm. The histogram for both quantities is shown in (b).

be above 1.7 ML under the given growth conditions. Thus, another sample with a thicker InAs layer of 1.9 ML was grown which exhibited a clear 2D→3D transition in the RHEED pattern, indicating the formation of QDs. This is confirmed by the AFM image depicted in figure 5.4 where the QD density is similar to the one of the positioned QD sample. The QD height and diameter distributions were both extracted from the AFM image and the average values are 13.0 ± 1.7 nm and 38.3 ± 3.9 nm, respectively. The corresponding histograms are depicted in (b). The values for the QD diameters are overestimated because a deconvolution of the AFM image was not performed due to the lack of knowledge of the exact tip geometry. Nevertheless, a few conclusions can be drawn. The observed average height of the self-assembled QDs is slightly higher than that of the positioned QDs while the height distribution is narrower with a standard deviation of about 13%. However, the base of the positioned QDs is likely to be situated below the plane level since they nucleate inside holes. Therefore, the actual average QD height is probably comparable to that of the self-assembled QDs. The average QD diameter is significantly higher compared to the positioned QDs (deduced from comparison of the values which were both extracted from convoluted AFM images) while the QDs are more uniform with a standard deviation of about 10%. Altogether, the self-assembled QDs exhibit a larger volume which can be related to the overall higher amount of InAs deposited so that a larger reservoir of material is available for each QD. This is accompanied by a slightly longer growth time which is known to lead to larger QDs [77]. The larger fluctuations in height and diameter of positioned QDs is probably caused by fluctuations in the hole size. It is known that the average QD size depends on the volume of the holes used for site-selective growth [72]. A detailed analysis of QD sizes depending on various parameters such as hole size or hole spacing will be presented in chapter 6 in the context of control of the structural properties of positioned QDs.

Two further aspects are important with respect to controlled formation of defect free QDs at defined locations. The deformation of the holes during BL overgrowth influences the ordering of the QDs as several aligned QDs were found in each hole instead of one single QD. The nucleation of these QDs must be related to the transformed shape of the hole and the exact position of the QDs inside the holes can be investigated by TEM. High resolution TEM (HRTEM) images can also be analyzed with respect to the formation of defects. Self-assembled QDs are usually coherently strained and therefore do not contain any defects

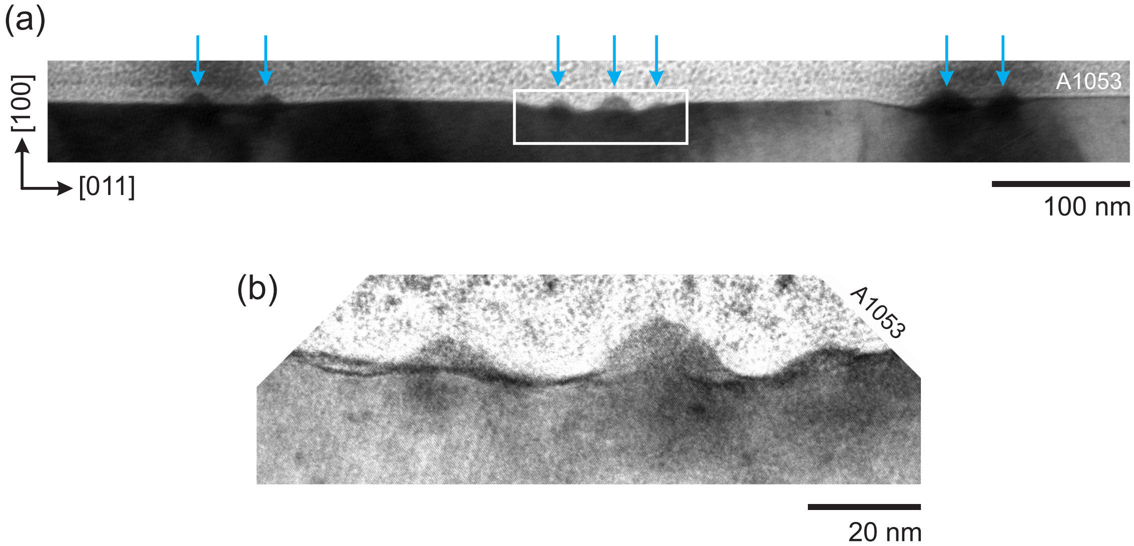

Figure 5.5 TEM investigation of site-selective QDs. The TEM image in (a) reveals well ordered QDs nucleated in defined holes. The QDs are marked with blue arrows. The separation between the holes is 250 nm. A magnified TEM image of the part in the white frame is depicted in (b) revealing three QDs in the hole. While one QD is found at the center of the hole, two QDs have formed on the sidewalls.

provided that they were grown on a clean surface. The growth on a patterned substrate is different since the substrate surface was etched and exposed to different substances during processing. Etched surfaces are subject to roughening which is partly compensated by the growth of the thin buffer layer. However, the restrictions on the BL thickness emerging from the fact that the holes fill up during growth possibly lead to an influence of the regrowth interface onto the formation of QDs and their coherence. Dislocations are one prominent type of defect that can be found in QDs and which are frequently observed in very large islands [78]. The occurrence of defects in the QDs likely degrades their optical properties.

In order to further characterize the site-selective QDs of the above sample (A1053) a thin lamella containing a row of several holes and thus QDs was cut out of the sample by focused ion beam and thinned with a beam of Ar^+. In this way, a 50-100 nm thin lamella can be obtained which is then suitable for TEM analysis. The TEM image in figure 5.5 (a) shows the profile of several positioned QDs. The QDs are free-standing and were only covered with Pt for the fabrication of the lamella. Three holes are observed with two or three QDs nucleating inside, as indicated by the blue arrows. The spacing between the holes is 250 nm. The interface between the patterned substrate surface and the GaAs BL is not observed as the contrast is too low. Variations in the contrast might be due to electrostatic loading of the sample during investigation or variations in the thickness of the lamella. A HRTEM image of the middle hole containing three QDs is shown in (b) and reveals some information on the QD positions inside the hole. The middle QD is found in the center of the hole and is also the largest of the three, both in diameter and height. The other two QDs are found at the tilted sidewall of the hole, possibly close to the rim. This implies that two favorite sites for QD formation inside holes can be distinguished, namely at the center of the hole and on the sidewalls. The first nucleation site is consistent with the earlier analysis which led to the local growth rate enhancement at the center of the hole due to increased In adatom migration to this site, compare the diagram in figure 2.8 (c).

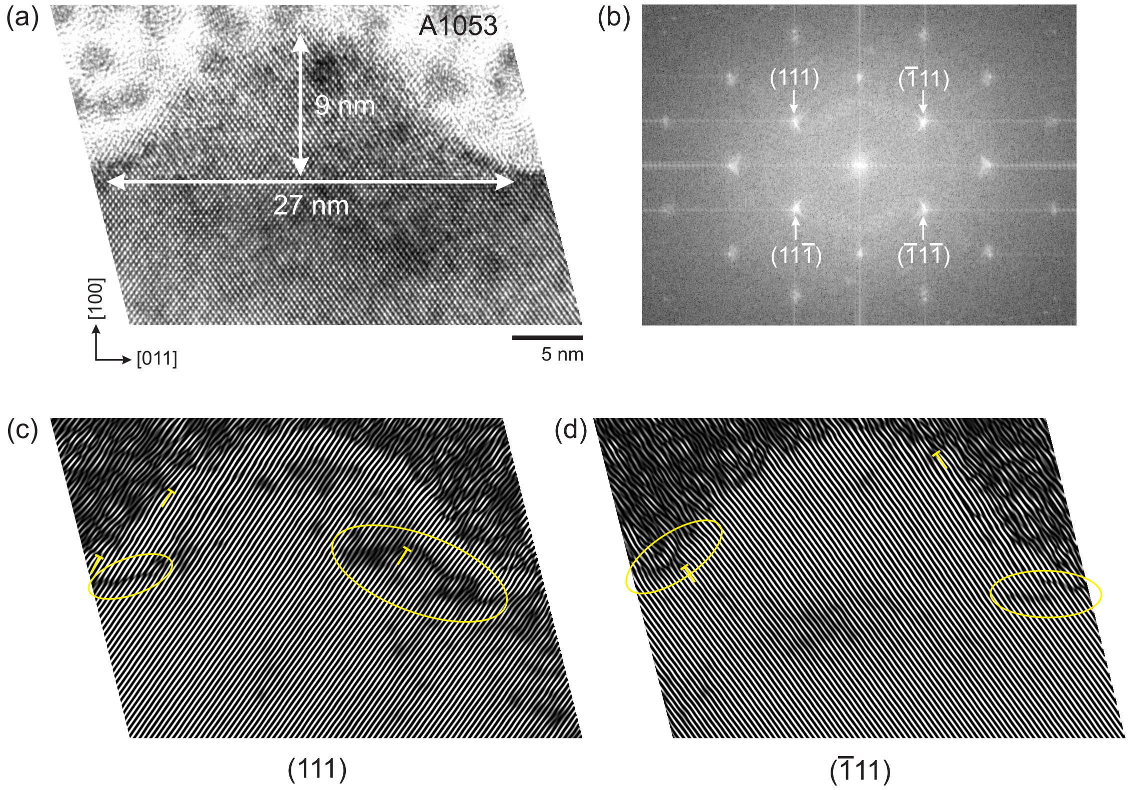

Figure 5.6 A HRTEM image with atomic resolution of the QD from the center of the hole is shown in (a). The dome-like shape of the QD is revealed. Crystallographic planes can be identified in the *Fourier* transform of the HRTEM image, (b). Selecting particular reflexes it is possible to investigate structural defects inside the QD. The inverse *Fourier* transform of the $(1\,1\,1)$ and $(\bar{1}\,1\,\bar{1})$ reflexes is shown in (c) and (d), respectively. The yellow ellipses mark irregularities in the line pattern, indicating lattice defects. A few edge dislocations are also marked.

There, two significantly smaller local growth rate maxima emerge at each side of the central growth rate maximum in addition. Their positions correspond very well with the observation of the QDs nucleating on the sloped side of the hole. Also, the reduced height is an indication of a lower local growth rate compared to the center. Not all holes exhibit the same QD arrangement. Other holes contain for example two QDs, each nucleating at the sidewall, or one QD in the center and another QD at the sidewall. Local variations in the hole's profile, size and depth which originate from imperfections in the lithographic definition of the holes likely influence the nucleation of the QDs in the holes and therefore account for the different QD configurations which have been observed.

In order to further investigate the QD structure a HRTEM image with atomic resolution was taken of the middle QD, as depicted in figure 5.6 (a). The measured size is in agreement with the statistical evaluation provided earlier. The shape of the QD is well observed and can be described as dome-like. In general, differences in the contrast might result from thickness variations of the lamella but if they are observed on a short scale they are more likely related to inhomogeneities in the material distribution. Even if pure InAs was grown on GaAs the emerging QDs do not consist of pure InAs. Interdiffusion leads to mixing of In and Ga in the respective layers at the interface. Unless special measures are taken to introduce diffusion barrier layers, InAs QDs will always contain a certain amount of Ga which is largest at the interface between InAs and GaAs. Similarly, the GaAs BL on top of which InAs is deposited will also contain some amount of In with a gradient in the opposite direction. Thus, the In concentration is highest at the top of the QD and some In is found in the GaAs layer below the QD. Such In concentration profiles could be revealed by TEM [77], grazing incidence x-ray diffraction [79] or cross-sectional scanning tunneling microscopy [80] in the past. Elements with higher atomic number Z appear darker in the TEM image. The dark areas in the HRTEM image in (a) are hence regions of higher In content since In has a lower atomic number than Ga ($Z_{\mathrm{In}} = 31$ and $Z_{\mathrm{Ga}} = 49$). This is at least true for the part below the QD where only the layer was imaged. An influence of the Pt cover on the contrast in the QD cannot be completely ruled out since it produces dark spots around the QD as well ($Z_{\mathrm{Pt}} = 78$). Since the lamella containing the QD has a thickness of 50-100 nm Pt is found before and behind the QD in the given image which possibly interferes with the material contrast inside the QD. The inhomogeneities in the material distribution are marked with white arrows. The *Fourier* transform (FT) of the HRTEM image in (a) can be used to identify crystallographic planes of the sample. The regular order of the atoms observed in the image and the specific crystal structure of GaAs and InAs lead to the reciprocal space image in (b) after performing the FT. A regular pattern of distinct spots is obtained with each spot corresponding to a specific crystal plane. The streaks in the FT image are artifacts originating from the edges of the real space image as the periodicity is abruptly broken. The reflexes of the $\{1\,1\,1\}$ planes are marked and are further used to investigate possible structural defects in the QD. Diagonally opposite reflexes belong to the same planes because the corresponding vectors normal to the planes are parallel but point in opposite directions. The $(1\,1\,1)$ and $(\bar{1}\,1\,\bar{1})$ reflexes were selected and the inverse FT was performed in order to obtain a real space image only containing the $(1\,1\,1)$ planes, as depicted in (c). The sames was done for the $(\bar{1}\,1\,1)$ and $(1\,1\,\bar{1})$ reflexes resulting in a real space image containing the $(\bar{1}\,1\,1)$ planes, see (d). The profile of the QD is visible and the diagonal lines represent the respective crystal planes. If defects were not present, a regular pattern of straight lines would fill the profile of the grown structure. Varying intensity along a line is related to the differences in contrast of the original image. Disrupted lines, however, indicate the occurrence of defects. Edge dislocations are easily identified by abruptly ending lines. Other defects such as stacking faults are more complicated to investigate and require a lot of experience in defect analysis. Regions marked with yellow ellipses exhibit irregularities in the line pattern and are thus possibly related to defects. Some edge dislocations are also indicated, mostly emerging at the edge of the QD. The GaAs layer and the central part of the QD show a perfectly periodic line pattern and are therefore considered to be free of defects. Altogether, the site-selective QD appears to be coherently strained with a few defects forming close to its surface and at the transition of the QD to the flat surface. The latter observation is consistent with the fact that the accommodated strain leads to a strong deformation of the lattice at the transition of the QD to the flat surface [81].

5.1.2 Photoluminescence measurements

After structural characterization of the site-selective QDs, their optical properties are considered next. Besides growing QDs at defined locations it is important that they are of high enough optical quality in order to be useful for applications in which they act as emitters, for example. Photoluminescence measurements can be used to investigate the optical quality of the QDs. Two samples were prepared in order to refer the measured PL to a particular configuration of site-selective QDs. The first sample contains a 16 nm GaAs BL grown on a patterned substrate followed by the deposition of 1.8 ML InAs resulting in

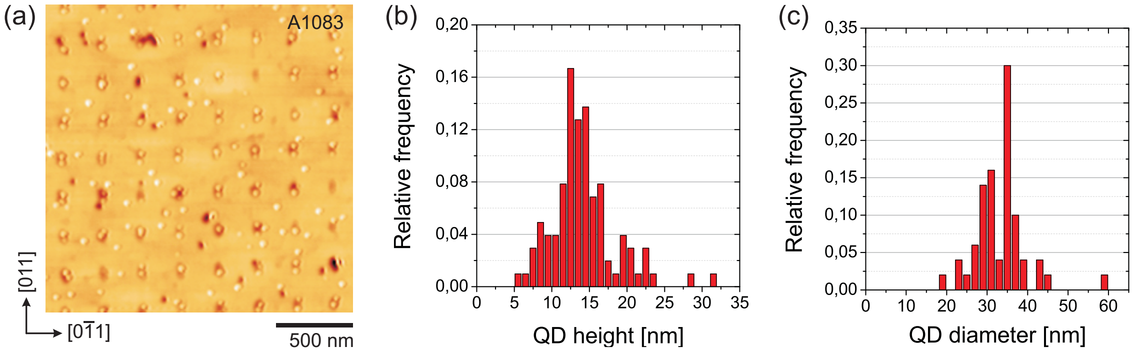

Figure 5.7 An AFM image of the uncapped reference sample reveals the regular QD array, (a). The hole spacing is 250 nm. The size statistics were extracted from the AFM image. The QD height histogram is shown in (b) and the average QD height is 14.2 ± 4.3 nm. The QD diameter histogram is given in (c) and the average QD diameter is 33.4 ± 6.3 nm.

QD formation. The second sample is similar but was additionally covered with a 90 nm thick capping layer of GaAs. An AFM image of the uncapped reference sample is shown in figure 5.7 (a). Again, mainly double QDs nuleate in the defined holes which were 58.4 ± 6.1 nm in size (measured along the elongated side, i.e. in the $[0\,\bar{1}\,1]$ direction) after lithography. The double dots are aligned in the $[0\,1\,1]$ direction due to the shape transformation of the hole during BL growth, just as before. The slightly larger amount of deposited InAs leads to larger QDs which is confirmed by the QD height and diameter distributions given in (b) and (c), respectively. The average QD height amounts to 14.2 ± 4.3 nm and the average QD diameter is 33.4 ± 6.3 nm. Despite the larger size of the QDs the size uniformity is in the same range as before with the standard deviations being 30% for the height and 19% for the diameter. A few unintentional holes are present on the sample as well as QDs nucleating in between the defined nucleation sites. The first problem could be later solved by improving the sample preparation process while the second problem of QD nucleation between the defined sites will be addressed in chapter 6 by introducing a post growth treatment.

The capped sample was placed into a continuous flow liquid helium cryostat and cooled down to 10 K for the PL measurement. Since only small arrays of 100 µm in size were patterned it is essential to precisely locate these arrays once the sample is in the cryostat. A pair of x- and y-nanopositioners was available in the cryostat allowing for access of different regions on the sample surface. A helium-neon laser beam at 632.8 nm is used to excite electrons in the sample above the GaAs band gap. The excited electrons in the conduction band and the emerging holes in the valance band possibly relax to their respective band edges in the InAs QD, bound together to form an exciton and finally recombine by emitting a photon. The resulting emission of the QD is collected in reflection geometry using a 100× objective. The PL signal is dispersed with a 1.26 m grating spectrometer and detected with a silicon CCD which is cooled by liquid nitrogen. The laser beam is strongly focused onto the sample so that a spatial resolution of about 1 µm is achieved, thus allowing for µ-photoluminescence measurements.

Four spectra were taken at different locations on the patterned array. For reference, another four spectra were recorded on unpatterned regions. All these spectra are shown in figure 5.8. The integration time during data acquisition was 5 s. Single QD emission lines are observed both in the patterned region, (a), and in the unpatterned region, (b). A

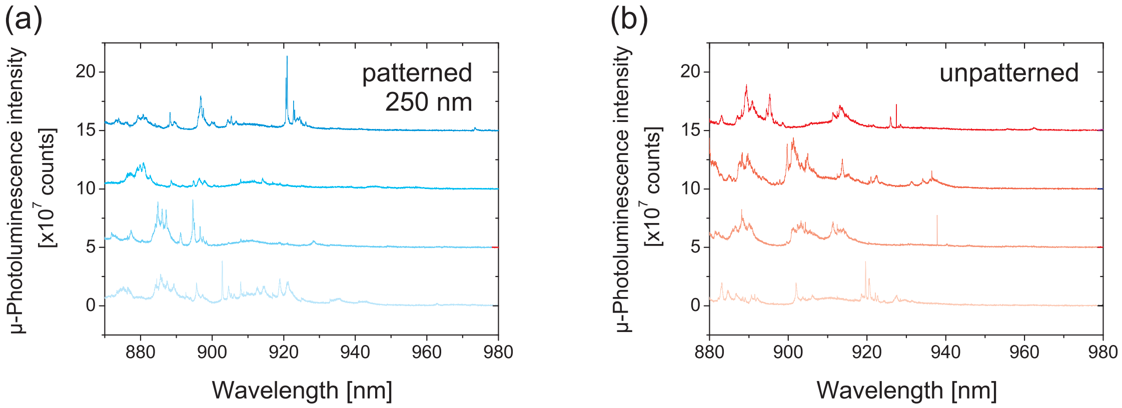

Figure 5.8 Micro-PL spectra were recorded in the patterned region at four different locations, (a). The hole spacing is 250 nm. Since the laser spot is focused to 1 µm, several QDs are illuminated at the same time. For reference, four spectra were recorded in the unpatterned region, (b).

difference between the spectra on the pattern and off the pattern is not obvious at first sight. The hole spacing in the patterned area was 250 nm. Since the spatial resolution is larger than the separation between the site-selective QDs several QDs will be excited simultaneously. Further complication arises from the fact that QDs nucleating between the holes will also contribute to the PL signal. It is thus not possible to distinguish the emission of site-selective QDs from that of self-assembled QDs. A qualitative statement on the optical quality of the site-selective QDs is however desired. Combining the AFM measurements of the uncapped sample with the PL data it is possible to deal with this difficulty and to estimate the degree of photoluminescence originating from positioned QDs. This statistical analysis is based on a comparison of the QD density in the unpatterned region with the density of QDs in the patterned region. The latter density can be further specified by distinguishing between positioned QDs and QDs nucleating between the defined sites. Thus, three different types of QDs can be identified. The densities are then related to the observed PL intensities by the following equation

$$c \cdot I_{\mathrm{PL}} = \eta \cdot n \quad . \tag{5.1}$$

The PL intensity I_{PL} is integrated over the range given in figure 5.8 and divided by the power of the incident laser to account for detector spectral response. The proportionality constant c is necessary as quantities with different units are related to each other. The density of the QDs contributing to the PL signal is given by n. It is not known whether the site-selective QDs emit as efficiently as the self-assembled QDs. Introducing the effective quantum efficiency η, which takes values between 0 and 1, can account for that fact. It is assumed that self-assembled QDs in the unpatterned region have the highest efficiency which is therefore set to $\eta_{\mathrm{un}} = 1$. Several AFM images were analyzed to determine the average densities of the respective QD types. Besides the array with 250 nm spacing a second array with 500 nm spacing was investigated by AFM on the uncapped sample and by PL measurements on the capped sample. The QD densities as well as the respective integrated PL intensities are summarized in table 5.1.

Provided that QDs found between the holes emit as efficiently as QDs in the unpatterned region the integrated PL intensity of these QDs should be equal to the ratio of the respective QD densities times the integrated PL intensity from the unpatterned region. Using equation 5.1 this reads $(n_{\mathrm{bet}}/n_{\mathrm{un}}) \cdot I_{\mathrm{PL,un}} = I_{\mathrm{PL,bet}}$. Plugging in the val-

Spacing	Region	Index	n [1/µm^2]	I_{PL} [10^5 counts/mW]
	unpatterned	un	28.8	5.15
250 nm	between holes	bet,250	18.5	4.54
	in holes	in,250	30.9	
500 nm	between holes	bet,500	23.1	5.57
	in holes	in,500	1.5	

Table 5.1 Values of the parameters used in the statistical evaluation of the PL signal. The density of QDs is denoted with n while the integrated PL intesity is given by I_{PL}.

ues (taken from table 5.1) on the left hand side leads to an integrated PL intensity of about 3.3×10^5 counts/mW. The PL intensity from the array with 250 nm spacing being 4.5×10^5 counts/mW exceeds this number by almost 40%. The extra light must hence originate from the site-selective QDs in the holes. The effective quantum efficiencies can be derived by setting up the linear system of equations

$$\begin{aligned} c \cdot I_{\mathrm{PL,un}} &= \eta_{\mathrm{un}} \cdot n_{\mathrm{un}} \\ c \cdot I_{\mathrm{PL,250}} &= \eta_{\mathrm{bet,250}} \cdot n_{\mathrm{bet,250}} + \eta_{\mathrm{in,250}} \cdot n_{\mathrm{in,250}} \\ c \cdot I_{\mathrm{PL,500}} &= \eta_{\mathrm{bet,500}} \cdot n_{\mathrm{bet,500}} + \eta_{\mathrm{in,500}} \cdot n_{\mathrm{in,500}} \end{aligned} \tag{5.2}$$

and solving for the unknown efficiencies η_{in} and η_{bet}. Here, it is assumed that $\eta_{\mathrm{in,250}} = \eta_{\mathrm{in,500}} = \eta_{\mathrm{in}}$ and $\eta_{\mathrm{bet,250}} = \eta_{\mathrm{bet,500}} = \eta_{\mathrm{bet}}$. The solution reads $\eta_{\mathrm{in}}/\eta_{\mathrm{bet}} = 0.306$ and $\eta_{\mathrm{bet}}/\eta_{\mathrm{un}} = 0.996$. These results show that the effective quantum efficiency of QDs nucleating between the holes is practically equal to that of the QDs in the unpatterned region, which is consistent since both types of QDs are formed in the same way so that they should not exhibit any differences in their optical quality. More important, the site-selective QDs have an effective quantum efficiency of about 30% of that of QDs nucleating between holes. The inferior optical quality is likely related to the occurrence of defects, as described above. Nevertheless, the site-selective QDs are optically active and the statistical method presented here can be very useful in the course of optimization of sample fabrication and QD growth.

5.2 Influence of pattern and growth parameters on quantum dot formation

The general structural features of positioned QDs and their optical properties have been described. Several QD arrays have been shown which were grown under similar conditions but using different hole geometries. Double dot nucleation was found in small shallow holes whereas longer chains of four or more QDs formed inside of larger and deeper holes. Besides defining the QD position it is also important to control the QD distribution, i.e. the number of QDs per hole and the overall QD density. The hole size influences the QD formation so that larger holes will accommodate more QDs. *Atkinson et al.* investigated in detail the relationship between hole size, deposited amount of InAs and QD occupancy [72]. They found an increase in the average number of QDs per hole for larger holes which is in agreement with the above observation. Furthermore, the QD occupancy for a given hole size depends on the deposited amount of InAs. The number of QDs per hole increases

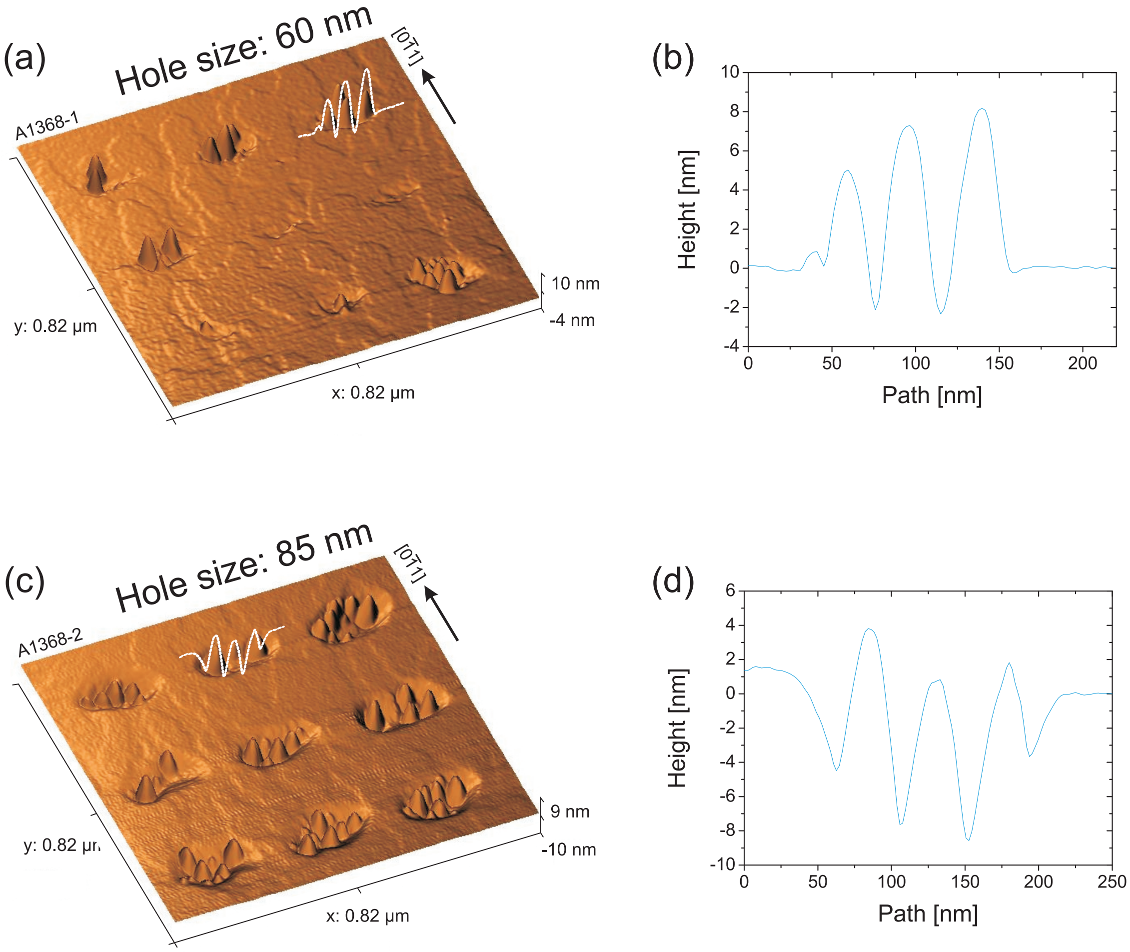

Figure 5.9 Influence of lateral hole size on QD formation in the holes. The AFM images show parts of a QD array in which the original hole diameter before BL growth was 60 nm, (a), and 85 nm, (c). Representative height profiles reveal the formation of QDs inside the holes, while the smaller holes, (b), are shallower than the larger ones, (d). Infilling is promoted for smaller holes.

if more material is provided. The influence of several pattern and growth parameters on the QD formation is investigated in order to gain further insight into the control of QD nucleation. The lateral hole size, the buffer layer thickness and the amount of InAs are expected to be critical parameters in this context. Four samples were prepared with optimized EBL and cleaning procedure so that QD formation is only observed inside the holes. Each sample contains several hole arrays with varying lateral hole size and hole spacing. The BL thickness and the deposited amount of InAs were varied.

5.2.1 Lateral hole size

A 15 nm BL was grown on a patterned substrate followed by the deposition of 1.6 ML of InAs which is below the critical thickness of QD formation on flat GaAs layers. The holes were etched 30 nm deep into the substrate and had an average lateral size of 60 nm and 85 nm before overgrowth. The pattern spacing was 250 nm. AFM images containing a part of the QD arrays and representative profiles of QDs in the holes are shown in figure 5.9. The array with the originally 60 nm large holes is depicted in (a) while the QDs grown

Lateral hole size	Spacing	Average QD occupation
60 nm	250 nm	2.2 ± 1.8
	500 nm	2.5 ± 1.1
85 nm	250 nm	3.7 ± 1.6
	500 nm	4.9 ± 1.4
	1000 nm	6.3 ± 1.3

Table 5.2 The average QD occupation was measured for different lateral hole sizes on several hole arrays with varying spacing. Both larger holes and larger hole spacings lead to higher QD occupations.

on the 85 nm large holes are presented in (c). Two profiles of several QDs in a hole were extracted from the AFM scans and are shown in (b) and (d) for the smaller and larger holes, respectively. In both cases the holes have grown in size due to the overgrowth with GaAs, as seen in the profiles. Although both hole types become shallower, the difference in the original hole sizes influences the growth process. The smaller holes are faster infilled during BL growth so that the positioned QDs are almost at surface level. The depth of the larger holes is not as strongly decreased so that the nucleating QDs are almost completely contained inside the holes. Quantum dots are found in the center of the hole and at the tilted sidewall, which is consistent with the earlier observation. The real height of the QDs can be deduced from the profiles and is on the order of 10 nm. This is consistent with other samples grown under similar conditions. The lateral hole size affects the number of QDs nucleating inside the holes. The average QD occupation on QD arrays of different spacing is given in table 5.2. The average number of QDs in the small holes does not seem to strongly depend on the spacing. This is explained by the fact that some of the holes are close to being or have already been filled up prior to QD growth, as confirmed by the QD array shown in (a). Hence, the hole volume is small and can only accommodate a certain amount of InAs. These holes which are not completely filled contain on average the maximum number of QDs which fit into the hole. The large standard deviation can be related to non-uniformities in the original hole size. The situation is different for the larger holes. First, the average number of QDs per hole is larger compared to that of the smaller holes. This is explained by the larger hole volume which can consequently accommodate a larger amount of QDs. Second, the QD occupation clearly depends on the hole spacing and increases with larger spacing. The reason is, that on the dense pattern the deposited InAs feeds a larger number of holes so that the reservoir of In adatoms for each individual hole is smaller compared to the sparser arrays. If all material is consumed and the maximum number of QDs that a hole can accommodate on average is not reached, a lower QD occupation is found. If the spacing between the holes is increased, the reservoir of In adatoms for each hole is larger and thus, more QDs can nucleate inside the hole. The QD occupation increases till the maximum number of QDs that the holes of a given size can contain is reached. Finally, the QD occupation can be controlled by varying the lateral hole size. It depends, however, on the spacing between holes if the amount of provided InAs is not enough to fill the holes with the maximum number of QDs.

5.2.2 Buffer layer thickness

Next, the BL thickness was varied. AFM images of three samples with a BL thickness of 5 nm, 15 nm and 35 nm are shown in figure 5.10. The holes had a lateral size of about 85 nm before growth and the separation is 500 nm. The influence of the BL thickness on

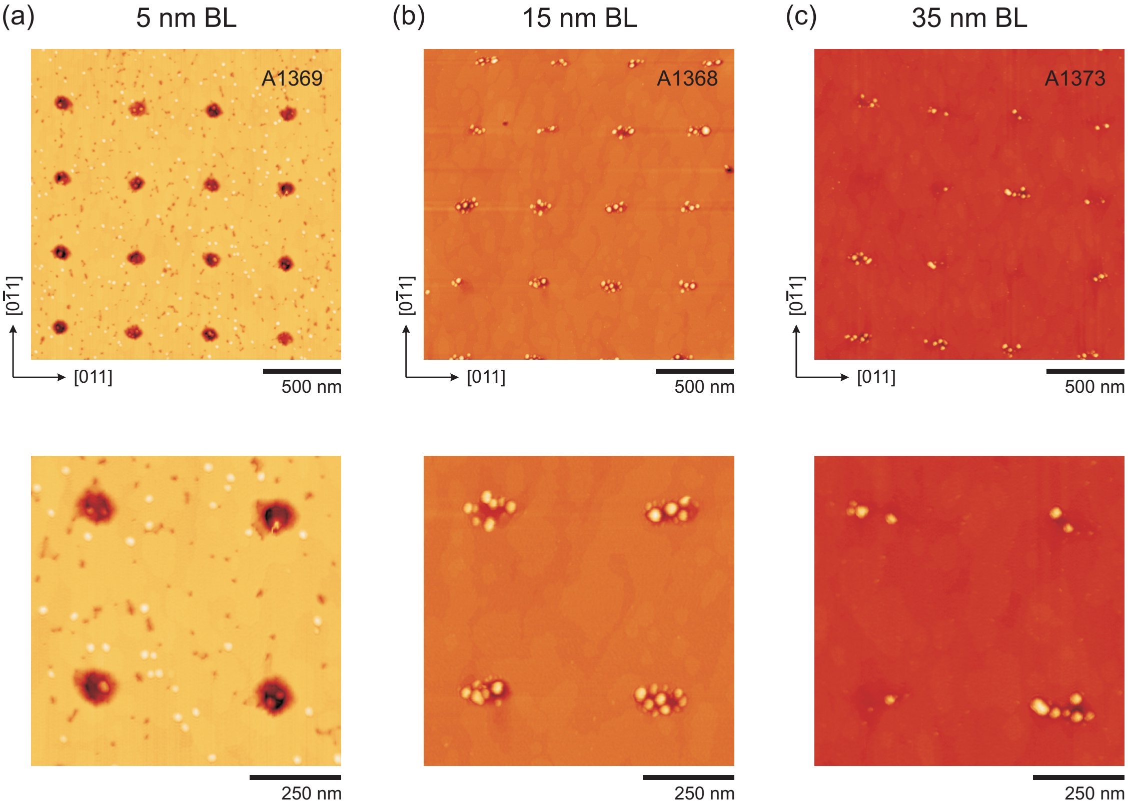

Figure 5.10 Three samples with different BL thickness and subsequent InAs deposition were prepared. The lower row of images is a magnification of the images in the upper row. A 5 nm BL does not lead to a closed film so that many QDs nucleate inbetween the holes, (a). The 15 nm BL leads dominant QD formation inside the defined holes, (b). At ab BL thickness of 35 nm some hole have been almost infilled, (c). The z-scale is 21.3 nm, 24.4 nm, 26.3 nm for (a), (b), (c), respectively.

the QD occupation as well as the QD size is investigated. The larger holes are favored for this analysis since they are not filled up as quickly as the smaller ones during BL growth. A few general characteristics can be deduced from the AFM scans. The deposition of 5 nm GaAs does not lead to the formation of a closed BL. Small pits are observed between the defined holes in (a). The pits are up to 5 nm deep and thus reach down to the regrowth interface. The pits are likely related to the short high temperature step introduced after Ga-assisted deoxidation. The sample is quickly ramped to 580°C and annealed for 2 min in order to remove possible residual oxide compounds. This is necessary to ensure full deoxidation but the short annealing at high temperature is obviously sufficient to promote the formation of pits on the freshly deoxidized surface. The 5 nm BL is not thick enough to fill up the unintentional holes. Residual surface contamination cannot account for the occurrence of the observed pits since the BL is finally closed when more GaAs is deposited, as seen in (b). Surface contamination would not allow for the closure of the BL as the Ga adatoms tend to keep away from the defect area. This is the result of the earlier TEM analysis of a defect hole which led to the subsequent optimization of the sample cleaning. The formation of the small pits is disadvantageous as it leads to the nucleation of QDs beyond the defined sites. Since a lot of pits are present many QDs are found between the fabricated holes. This, of course, interferes with the attempt to control the QD position. The holes contain a few QDs but it is questionable whether they are coherent since the

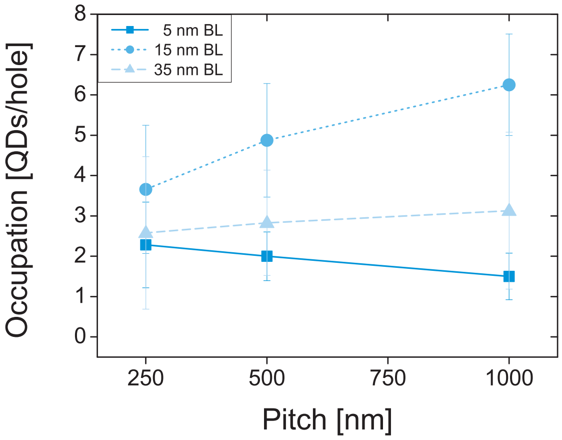

Figure 5.11 The QD occupation is plotted with respect to the hole spacing for different BL thicknesses. The lines are only a guide to the eye. The QD occupation is highest for the 15 nm BL and generally increases with larger hole spacing, once the BL forms a closed film.

thin BL is probably not sufficient to account for the surface roughness in the hole resulting from etching. The deposition of 15 nm GaAs is enough to fill up the unintentional pits and to provide a smooth and closed BL. In general, QD nucleation is only observed in the defined holes, with a few exceptions where defects are still present in the BL. Several QDs are found in each hole and every hole seems to be occupied, as observed in (b). Further increasing the BL thickness up to 35 nm slightly changes this situation because some of the originally 30 nm deep holes have been almost filled up and consequently reduce their attractive potential for site-selective QD formation, as seen in (c). Hence, not all defined sites exhibit several QDs. Also, the average number of QDs per hole seems to have decreased compared to the sample with the 15 nm thick BL.

A quantitative analysis was performed to verify the above observations. The QD occupation was extracted from AFM images and was related to the hole spacing (pitch) for the different BL thicknesses. The results are presented in the diagram of figure 5.11. Two different trends can be described. First, the QD occupation slightly decreases from 2.3 QDs/hole to 1.5 QDs/hole with increasing pitch in case of the thin BL. Second, the QD occupation increases with the pitch for the other samples. The opposed behavior is not precisely understood. Possibly, it can be explained by the formation of QDs between the holes which is observed on the thin but not on the thicker BLs. The deposited amount of InAs limits the number of nucleating QDs. In case of the 5 nm BL, some In adatoms diffuse into the defined holes whereas the larger part forms QDs at random sites. Since the defined holes cover a certain fraction of the substrate surface, less random pits are found per unit area on the dense hole array. This is confirmed by counting the number of randomly nucleating QDs. In representative areas an average density of 44 QDs/µm^2, 57 QDs/µm^2 and 75 QDs/µm^2 was found between the defined holes for a spacing of 250 nm, 500 nm and 1000 nm, respectively. The number of defined holes in one µm^2 is 9, 4 and 1 for the different spacings. The gain in random QDs per unit area with increasing spacing (13 QDs/µm^2 and 17 QDs/µm^2) is larger than the decrease in the hole number (5 holes/µm^2 and 3 holes/µm^2) so that less material possibly leading to QD formation is available for each defined hole on average. Unintentional random QDs are essentially not observed on the samples with thicker BLs. For 15 nm and 35 nm the average QD occupation increases with larger spacing. This can be explained by the fact that the holes do initially not

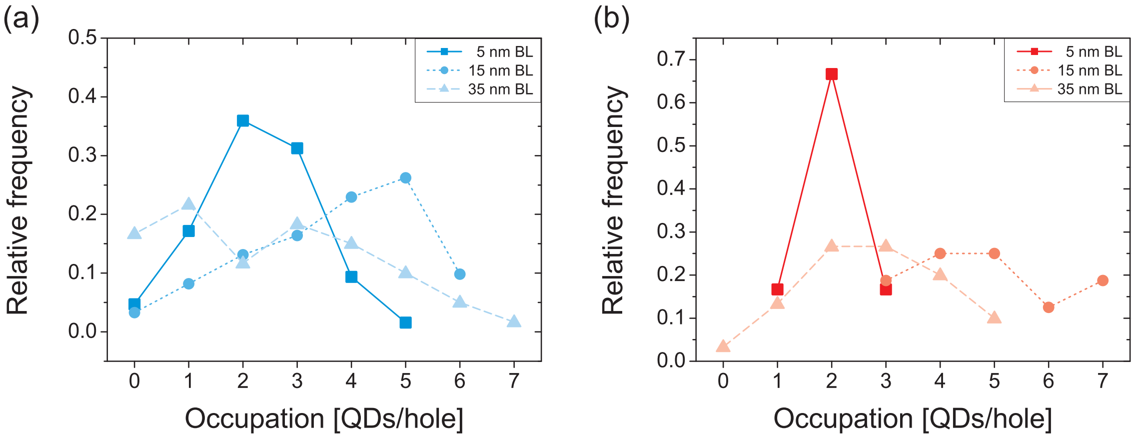

Figure 5.12 The distribution of QD occupations is given different BL thicknesses. The hole spacing is 250 nm in (a) and 500 nm in (b). The distributions are rather broad, but slightly shift to tower occupation values for thicker BLs.

contain the maximum number of QDs that could be accommodated. Increasing the hole spacing reduces the hole density and thus more material is available for each individual hole, effectively increasing the number of nucleating QDs. The average QD occupation increases from 3.7 QDs/hole to 6.3 QDs/hole for the 15 nm BL and from 2.5 QDs/hole to 3.1 QDs/hole for the 35 nm BL. Despite the thick BL all holes are still occupied which is an indication that they have not completely filled up yet. However, the QD occupation is lower on the 35 nm BL for all spacings. The reason is that the holes become shallower with increasing BL thickness and therefore lose their attractive force for QD formation which is based on the surface curvature. The local accumulation of InAs is reduced and hence less QDs nucleate in the defined holes. The dependence of the average QD occupation on the hole spacing is also reduced as the increase from the 250 nm to the 1000 nm spacing is only 0.6 QDs/hole (compared to 2.6 QDs/hole on the 15 nm BL). The reason is again related to the transformation of the hole shape. The reduced potential for adatom accumulation weakens the dependence on the surrounding. Less material is attracted into the holes so that the competition between neighboring holes decreases. An increase in hole spacing does therefore not lead to a strong gain in QD formation.

Besides the average QD occupation the distribution of occupation numbers is also of interest. In an ideal case, a narrow distribution is desired which means that the QD occupation can be well controlled on a given pattern and the fluctuations can be reduced to a minimum. The actual number of QDs/hole should then be determined by the hole geometry and the process parameters. The QD occupation distributions were calculated for the different BL thickness and two hole spacings. The resulting diagrams are depicted in figure 5.12. The distributions for the array with 250 nm spacing are shown in (a). The distribution for the 5 nm BL reaches from 0 QDs/hole to 5 QDs/hole while more than 60% of the holes contain two or three QDs. The distribution is, however, not very meaningful since a lot of QDs have nucleated between the holes and it is doubted that the site-selective QDs are free of defects. The distribution of QD occupations is rather broad in case of the 15 nm thick BL. It ranges from 0 QDs/hole to 6 QDs/hole and 2, 3, 4, 5 and 6 QDs are found in more than 10% of the holes each. This large spread is likely related to fluctuations in the original hole size. The distribution becomes even broader when growing the QDs on top of the 35 nm thick BL. The peak has shifted to the left so that lower occupation numbers are more frequent. More than 15% of the holes are unoccupied. The corresponding distributions for

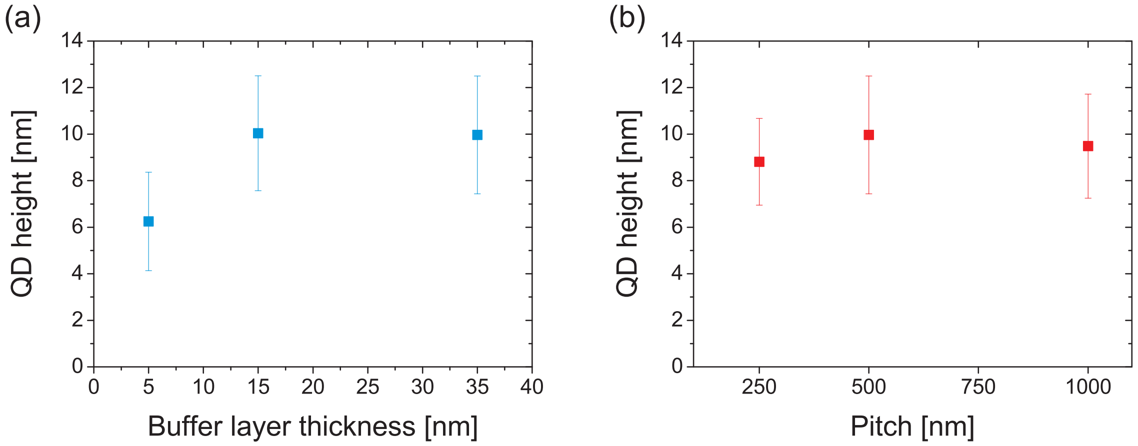

Figure 5.13 The average QD height is plotted with respect to the BL thickness, (a), and the hole spacing, (b). While the QD height is smallest for the thinnest BL it is rather constant for a BL thickness of 15 nm and 35 nm. The hole spacing has only little influence on the QD height.

the 500 nm spaced hole array are given in (b). The position of the distributions is similar to the lower spaced array but the widths have narrowed. More than 65% of the holes contain two QDs on the 5 nm BL. Due to the same concerns mentioned above, this result should not be over-interpreted. The distribution for the 15 nm BL is still rather flat but extends only from 3 QDs/hole to 7 QDs/hole. An explanation for the narrower distribution is difficult since the fluctuation in hole size should be the same as for the 250 nm array. The reduced hole density possibly enforces a more equal distribution of material. Locally varying growth conditions due to fluctuations in hole size are likely enhanced if the holes are closer together. The QD growth inside a particular hole on the larger spaced array is then less influenced by its local surrounding since neighboring holes are further away. The distribution for the 35 nm BL has again shifted to lower QD occupation values and more than 50% of the holes contain two or three QDs. Only a few holes contain no QDs which is an improvement compared to the 250 nm array. Both, pattern spacing and variation of the BL thickness affect the QD distribution. Larger spacings promote higher numbers of QD per hole and slightly more uniform distributions for a given hole size. Thicker BLs can decrease the QD occupation while slightly improving the occupation uniformity.

In addition to the evaluation of the QD distribution, a short analysis of the relationship between QD size and BL thickness is provided. The average height of the positioned QDs was measured on the 500 nm array and was related to the BL thickness, as shown in the diagram of figure 5.13 (a). An increase in the QD height from about 6 nm to 10 nm is observed when the BL thickness changes from 5 nm to 15 nm. Due to the unintended QD nucleation between the holes, less InAs is available, on average, to be accumulated in the holes overgrown with the 5 nm BL. It is questionable if the rough surface allows for efficient growth rate enhancement in the hole. The average QD height decreases from 10 nm to about 4 nm on the 35 thick BL. The efficiency to attract In adatoms depends on the hole profile and the associated surface curvature. The overgrown holes lose their shape with increasing BL thickness and therefore their potential to locally accumulate In adatoms. This is the cause for the reduced QD height on the 35 nm BL as the holes in which the QDs nucleate have become much shallower. The dependence of the QD height on the pattern spacing is not very significant, as illustrated by the diagram in (b). The average QD height was measured for different hole spacings on the sample overgrown with

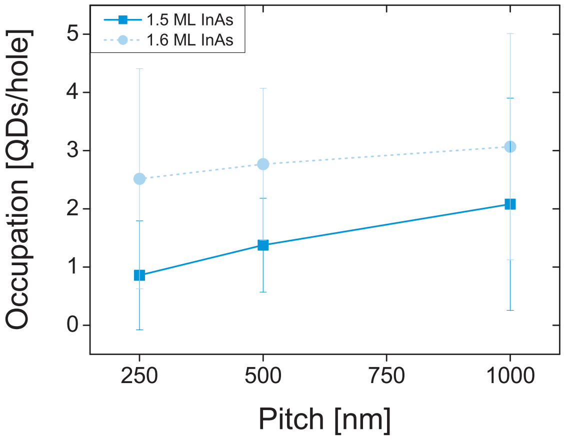

Figure 5.14 The average QD occupation is given depending on the hole spacing for different amounts of deposited of InAs. The occupation increases with larger spacing and with larger InAs amount.

the 35 nm thick BL. The average QD height slightly increases from 3.3 nm for the 250 nm spacing to 3.9 nm and 3.8 nm for the 500 nm and 1000 nm spacings, respectively. The standard deviation amounts to about 25% in all cases. The QD height and hence the QD size is more influenced by the BL thickness.

5.2.3 InAs amount

The increase of the number of QDs per hole with larger hole spacing was related to a larger reservoir of InAs for each individual hole on sparser arrays. Therefore, the amount of available InAs plays a role in the formation of a particular QD distribution. The amount of provided InAs was varied in order to investigate its effect on the QD occupation and size. 1.5 ML and 1.6 ML of InAs were deposited on a patterned substrate which was overgrown with a 35 nm GaAs BL. The QD occupation was measured for different hole spacings. The results are shown in the diagram of figure 5.14. In the case of 1.6 ML, essentially all holes are occupied, independent of the pitch. A slight increase of the occupation with larger spacings from 2.5 QDs/hole to 3.0 QDs/hole is observed, as analyzed before. The occupation values are smaller for the lower InAs amount and the increase with hole spacing is a little stronger, from 0.9 QDs/hole to 2.1 QDs/hole. The trend is the same as for the 1.6 ML of InAs but the reduced amount of deposited InAs is responsible for the lower occupation. The relative value for the standard deviation of the average occupation is not improved by the 1.5 ML of InAs but the absolute values are lower than for 1.6 ML. This is reflected in the occupation distribution.

The diagrams in figure 5.15 depict the occupation distributions for 1.5 ML and 1.6 ML of InAs on the 250 nm (a) and 500 nm array (b). While in (a) the distribution is rather broad and flat for 1.6 ML, the distribution for 1.5 ML rises with smaller occupation and is maximum at 0 QDs/hole. Almost 50% of the holes are unoccupied. The amount of InAs is not sufficient to form QDs in the majority of holes. As a result, the shape of the occupation distribution is different from the sample containing 1.6 ML. The latter also contains not enough InAs to occupy all holes with QDs but the variation in occupation values is much larger. This might be due to fluctuations in the original hole size combined with the insufficient amount of InAs. The situation on the 500 nm array is another, as seen in (b). 1.5 ML of InAs is enough to populate almost all holes with QDs with almost

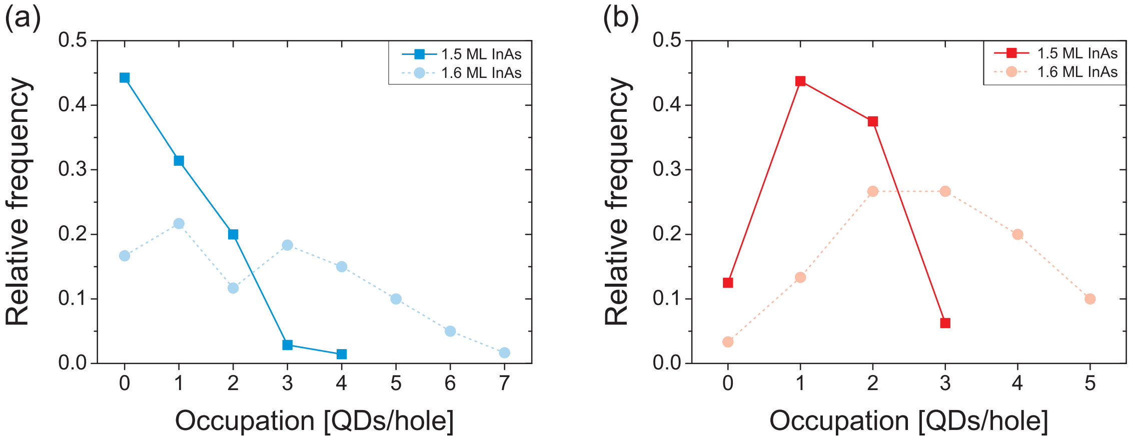

Figure 5.15 The QD occupation distributions are shown for different amounts of deposited InAs. The hole spacing is 250 nm for (a) and 500 nm for (b). Smaller amounts of InAs lead to a narrower distribution which shifts to lower occupation values.

80% of the holes containing one or two QDs. The distribution is narrower than for the 1.6 ML sample where two or three QDs are found in about 50% of the holes. Varying the deposited amount of InAs it is thus possible to influence not only the occupation but also the occupation distribution. Lower amounts lead to narrower distributions on average which is favorable, if a uniform occupation is aimed at.

Finally, the QD height was analyzed with respect to the amount of InAs. The expected reduction in QD size is observed in the diagram of figure 5.16 where the average QD height is given with regard to the hole spacing for 1.5 ML and 1.6 ML of InAs. The values were measured on samples containing a 35 nm GaAs BL. While a slight variation of the height is observed depending on the pitch, the average QD height is a factor of three lower when 1.5 ML of InAs is deposited instead of 1.6 ML. The small change in the InAs amount has a strong effect on the QD height. This has to be considered when searching for appropriate QD configurations and sizes. However, other techniques like post growth annealing are available to control the QD size after growth so that the benefits of reduced deposition amounts could be used while maintaining a certain freedom in adjusting the QD size, in general.

5.3 Quantum dot growth on dry etched hole arrays

One inherent problem in the hole fabrication process used for the above investigations is the limited control of the hole profile due to the use of wet chemical etching. Crystallographic etching leads to lateral etching which substantially enlarges a hole, with the increase in diameter being approximately proportional to the etch time. Furthermore, major crystallographic planes of the GaAs substrate, $\{1\,1\,1\}$ in this case, will be etched so that an originally round hole in the resist transforms into a rectangle in the substrate. Another consequence is that the sidewalls of the holes will hence correspond to major crystal planes of the GaAs substrate so that their slope can hardly be controlled. Different etch rates for orthogonal crystal directions finally result in an elongation of the holes in the $[0\,\bar{1}\,1]$ direction.

It was shown in chapter 3 that reactive ion etching can be used to partly circumvent the described limitations of WCE. EBL and RIE with an inductively coupled plasma was used to fabricate hole arrays in which the holes exhibit steep sidewalls of up to 90°. The

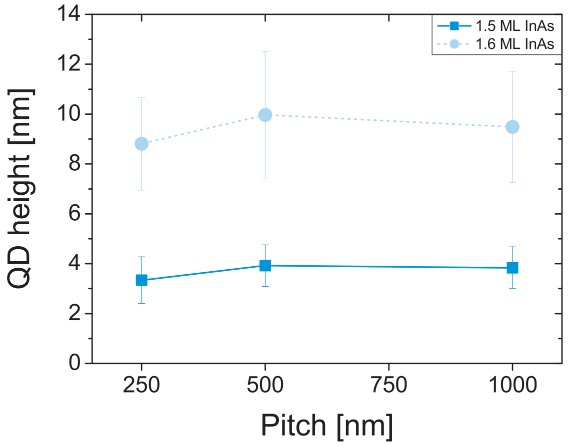

Figure 5.16 The average QD height was measured on differently spaced arrays for two amounts for InAs. While no significant dependence on the hole spacing is observed, the QD height increases with the deposited amount of InAs.

hole shape is largely maintained and the elongation of the holes in the particular $[0\,\bar{1}\,1]$ direction could be reduced. A set of three samples was fabricated for which the etch time was varied in order to study the dependence of the QD occupation on the hole depth. The samples were etched with a mixture of $SiCl_4$ and Ar with a ICP power of 150 W and a RF power of 20 W in order to obtain a low etch rate. The three samples were etched for 10 s, 15 s and 20 s. Afterwards, the remaining resist was removed and the samples were cleaned according to the optimized procedure. Ga-assisted deoxidation was used to remove the surface oxide and a 12 nm thick GaAs BL was grown on top of the patterned substrate after a quick annealing at 560°C. The deposition of 1.6 ML InAs led to the formation of site-selective QDs with essentially no random QDs nucleating on the flat surface between the holes.

Four AFM images of QD arrays are shown in figure 5.17. The amplitude signal is shown for better contrast and representative height profiles were extracted from height images. The images in (a) and (b) belong to the sample etched for 10 s and the ones in (c) and (d) to the sample etched for 20 s. The hole spacing is 500 nm. The two arrays of each sample differ by the hole size. The original hole sizes defined in the resist were equal in (a) and (c) and in (b) and (d), while the holes were smaller in the first two arrays. The situation slightly changes during dry etching since lateral etching cannot be completely avoided. The longer the etch time, the larger a hole becomes. As a consequence, the originally equal holes of the two samples differ in size after dry etching. Additional complication arises from the fact that in RIE the etch depth of narrow structures for a given etch time depends on the lateral size of the structure. This is referred to as RIE lag. Hence, on each sample larger holes become deeper. Nonetheless, it is possible to qualitatively analyze and compare the samples with different etch times with respect to the QD occupation. In all AFM images QD formation is only observed inside the holes, which proves the high selectivity of the holes for QD nucleation. The average diameter of the holes in the arrays of (a) and (b) after GaAs BL overgrowth were determined as 92 nm and 119 nm, respectively. Despite the thin BL, considerable enlargement of the holes is observed induced by the overgrowth. As observed in the respective height profiles, the holes in (a) are shallower compared to those in (b). The described RIE lag effect is one reason, but as before, small holes tend to infill faster than larger ones. As a consequence, more QDs are found to nucleate in each hole on average in (a). A similar situation is observed for the sample which was etched for

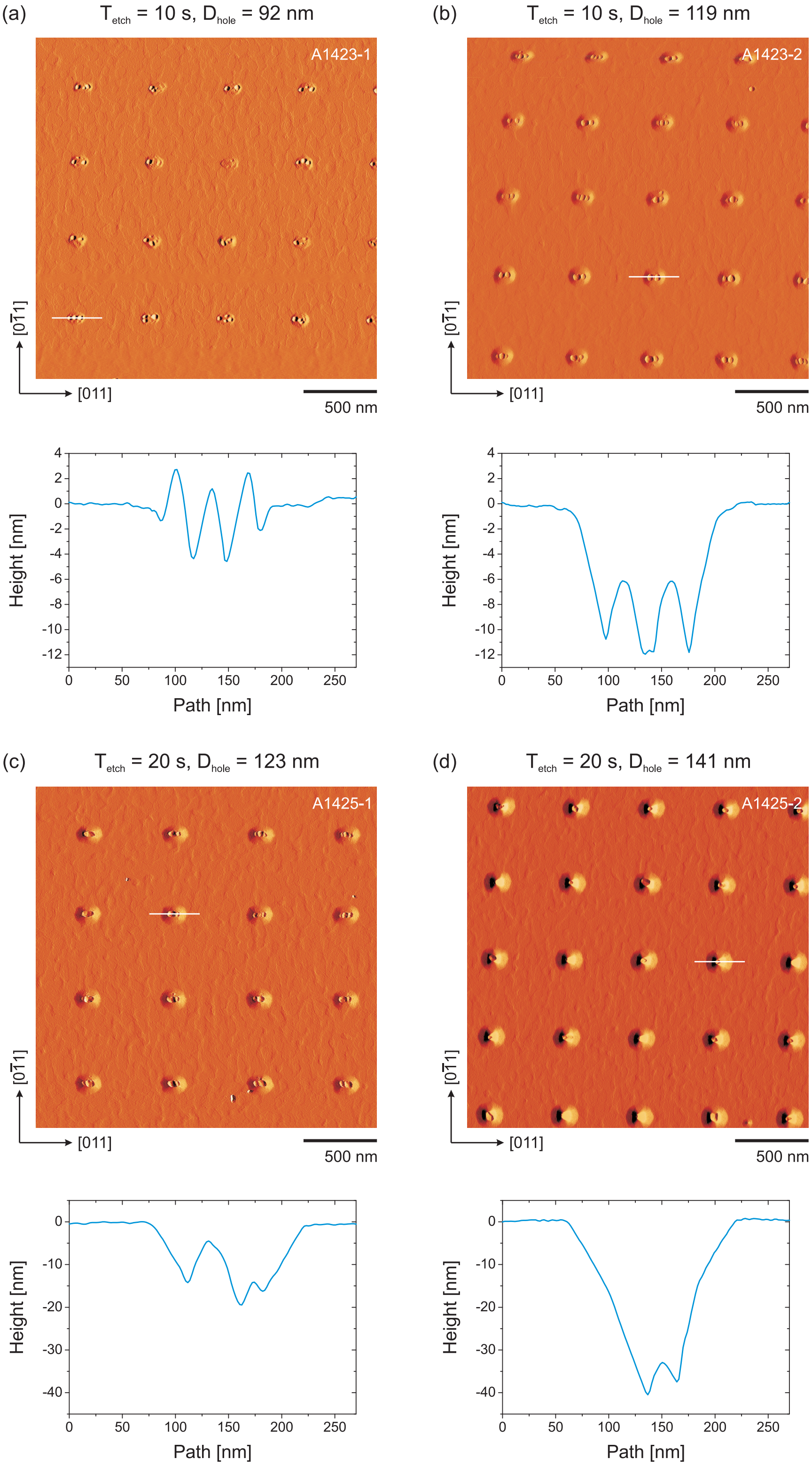

Figure 5.17 AFM images of site-selective QDs formed in dry etched holes are shown. The holes in (a) and (b) were etched for 10 s, the holes in (c) and (d) for 20 s. The average size of the holes after BL growth is given for each AFM image. Representative height profiles were extracted.

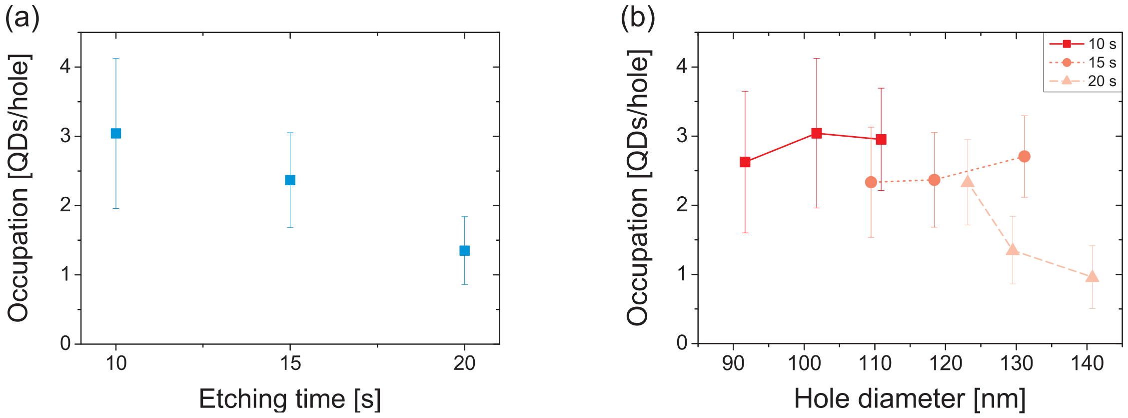

Figure 5.18 The average QD occupation was measured for different etch times and thus different hole depths, (a). The hole spacing is 500 nm and the holes were of the same size before etching. In (b), the average QD occupation is shown with respect to the hole diameter after BL overgrowth for the differently etched samples. Since each three holes were originally equal in size, it is demonstrated that longer etch times lead to a lateral increase in hole size. For a given etch time, the QD occupation slightly increases with the hole diameter. Only for the longest etch time, the QD occupation decreases. The effect of the hole depth is also observed. The hole spacing is 500 nm.

20 s. The holes in (c) are shallower than the ones in (d) and the number of QDs per hole decreases for the deeper holes.

A quantitative evaluation of the QD occupation led to the diagrams of figure 5.18. In (a) the average QD occupation is given with respect to the etch time, thus the hole depth. In order to extract these values the same arrays, i.e. same original hole size and same hole spacing (500 nm), were analyzed on the three samples. As described above, the originally equal hole diameters are not conserved during dry etching, but this does not interfere with the observed trend, that the QD occupation decreases with increasing hole depth. The average diameters of the analyzed holes were 101.9 ± 33.8 nm, 118.4 ± 14.0 nm and 129.5 ± 5.5 nm for the samples etched for 10 s, 15 s and 20 s, respectively. The average QD occupation drops from 3.0 ± 1.1 QDs/hole to 1.4 ± 0.5 QDs/hole. Apparently, the fluctuation of QD occupations has also decreased as deduced from the lower standard deviation. The diagram in (b) shows QD occupation depending on the hole diameter for the three samples. The original hole diameters were equal for each sample, but dry etching and overgrowth lead to the described enlargement of the holes. Longer etch times result in larger holes. Furthermore, the behavior seen in (a) is reproduced for all hole sizes. Namely, the average QD occupation values of the sample etched for 20 s are below those of the sample etched for 15 s and these are again below those of the sample etched for 10 s. Nevertheless, a different dependencies on the hole size are noticed for the three samples. For the samples etched for 10 s and 15 s the average QD occupation slightly increases with larger hole diameter. This is in agreement with the investigations of wet chemically etched holes, for which a similar behavior was found. However, the sample with the deepest holes exhibits an opposite dependence. Here, the average QD occupation constantly decreases with increasing hole diameter. A possible explanation might be related to the fact that the sidewalls become steeper with increasing hole depth. Therefore, QD nucleation on the sidewalls, as found in shallow holes, is probably inhibited and QD formation is only observed at the bottom of the holes. As a consequence, site-selectivity can be improved by deeper holes. This is confirmed by the observation, that on the array with the deepest, and at the same time largest, holes (not shown) 80% of the holes are occupied with a single QD.

The influence of the hole profile and even more of the hole depth on the QD occupation was hence demonstrated. A tendency of reduction in average QD occupation with increasing hole depth could be found. To gain a better understanding of theses influences and the many parameters involved, further studies are needed in which the BL thickness might also be varied and finally, the optical quality of such positioned QDs remains to be tested. Since inferior photoluminescence intensities were found for site-selective QDs formed on dry etched patterns [82] one possible way to account for this drawback might be to increase the hole depth and therefore allow for a thicker GaAs BL. Electronic defects introduced at the etched surface during dry etching are likely reduced this way.

5.4 Conclusion

To conclude with, the experimental realization of site-selective QD formation was described in this chapter. Positioned QDs have smaller diameters compared to self-assembled QDs but the heights are comparable. The size distribution of positioned QDs is mostly related to size fluctuations of the lithographically defined holes. The internal structure of a positioned QD was investigated by TEM and the QD was found to be nearly defect free and coherently strained. The optical properties of site-selective QD were investigated by photoluminescence measurements. A statistical analysis confirmed that positioned QDs are optically active. Next, the influence of the pattern and the growth parameters on the QD formation was considered. It was found that larger holes lead to higher QD occupations, but the occupation also depends on the hole spacing. An increase in hole spacing promotes the accumulation of more InAs per hole so that the of QDs inside a hole rises with larger spacings. The thickness of the GaAs buffer layer also influences the QD formation. Thicker buffer layers result in lower QD occupations, especially when the holes start to infill. Infilling of the holes was found to be enhanced for smaller holes. The amount of deposited InAs is relevant and can be used to control the overall amount of site-selective QDs. Dry etching was used to change the hole profile and shape. It could be observed that deeper holes reduce the QD occupation. Finally, arrays with single QD occupation in up to 80% of the holes could be realized.

6 Controlling structural properties of positioned quantum dots by in situ annealing

Controlling the QD occupation and the QD size are important aspects of site-selective growth as these properties affect the applicability of the structure in a possible device. It was shown in the previous chapter that the QD occupation is largely influenced by the lateral hole size, the hole depth, the hole spacing, the buffer layer thickness or the deposited amount of InAs, whereas the QD size mainly depends on the InAs amount. Structural parameters of the pattern and growth parameters have therefore to be adjusted together according to the needs. It is known that QD occupation and QD size are also affected by the InAs growth rate. Smaller growth rates favor the formation of larger QDs and lower QD occupations [72]. However, the exact reasons for such a behavior were not emphasized so far. It is likely that the reduced growth rate gives more time to the In adatoms to rearrange on the surface during the growth process. Such a mechanism could in turn be exploited as a way to control the material distribution after growth and therefore allow for an expansion of possible QD configurations for future applications. The process of keeping a readily grown QD sample at elevated temperature without any further material deposition (besides As to stabilize the surface) is termed *in situ* annealing. The elevated temperature enhances the material redistribution through diffusion, desorption and interdiffusion. The latter process, for example, is known to cause a shift of the QD emission towards the blue during *ex situ* rapid thermal annealing (RTA) [7]. The reason is an intermixing of In and Ga in the QD. RTA can therefore be applied to a final QD structure in order to adjust its PL emission. The overall material distribution and the QD configuration can, however, not be controlled this way. The advantages of *in situ* annealing are based on the fact that the QDs are not covered with a capping layer yet and thus, all three above processes could in general contribute to the material redistribution. The potential of this approach to control the structural properties of positioned QDs as well as the QD distribution was investigated and is presented in this chapter. A closer description of involved processes is given and general conclusions are drawn from first annealing experiments. This is followed by a quantitative analysis of the QD evolution during *in situ* annealing. Finally, X-ray diffraction experiments to quantify the observations on a large scale are presented.

6.1 Redistribution of In during in situ annealing

Leading processes that take place during *in situ* annealing are depicted in figure 6.1. Indium adatoms can desorb from the surface (1) or from a QD (2), they can detach from a QD (3) and diffuse on the surface (4), they can attach to a QD (5) and In and Ga atoms can intermix (6) so that an InAs QD will contain a considerable amount of Ga. The processes are not exclusive, i.e. several of them can act on a single In adatom. An In adatom could, for example, detach from a QD, diffuse on the surface and then desorb or attach to another QD. The extent to which these processes are observed mainly depends

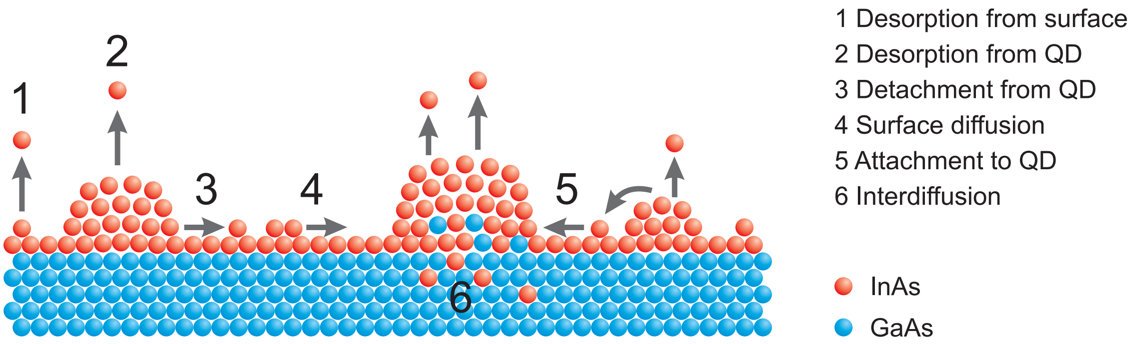

Figure 6.1 Illustration of leading processes that take place during *in situ* annealing.

on the annealing temperature and the As background pressure.

In general, two processes that alter the QD structure can be distinguished. At lower temperatures QDs tend to ripen whereas they dissolve at higher temperatures [26, 27]. The ripening of QDs is based on standard ripening theory according to *Ostwald* in which large particles grow at the expense of smaller ones which slowly disappear [83]. The driving force for this process is a reduction in surface free energy. According to the *Gibbs-Thomson* effect smaller particles have a higher vapor pressure. The reason is the stronger curvature compared to large particles. Molecules at the surface of smaller particles are less tightly bound and can hence more easily detach from the particle surface. A net diffusion of molecules towards larger particles is then observed. Larger particles have a smaller surface to volume ratio and are thus thermodynamically favored. A critical particle size exists at each stage of the ripening process which determines whether a particle will shrink or ripen. This was theoretically described by *Lifshitz/Slezov* [84] and *Wagner* independently [85]. While *Ostwald* ripening was originally formulated for fluid solutions it was later extended to solid solutions by *Vengrenovitch* in order to calculate the maximum particle size as well as the distribution of particle sizes during annealing [86, 87]. In this approach, three different ripening models were distinguished. *Hu* investigated these processes in detail by measuring the film force exerted by a particular QD configuration during annealing [20]. At lower annealing temperatures (440°C) ripening is governed by the diffusion of atoms along the QD boundaries while at higher temperatures (455°C) the ripening is controlled by detachment and attachment of atoms on the QD surface.

At elevated substrate temperatures desorption of atoms becomes dominant and thus governs the evolution of the QD structure. The detailed study of *Heyn* revealed that desorption of atoms from InAs QDs takes place in a layer-by-layer fashion, starting from the top of the QD [27]. The desorption rate strongly depends on the substrate temperature because of the temperature dependence of the sticking coefficient α_{In} (inversely proportional to the attempt frequency for desorption ν_{de} introduced earlier) of impinging In atoms. A continuous reduction of α_{In} usually sets in at temperatures around 500°C. The flux of impinging As_4 molecules also influences the desorption rate with an increase of the QD lifetime for higher As_4 fluxes [27]. In this context, the lifetime of a QD is referred to as the time upon which the QD size has not decreased below a minimum value. The As flux can hence be used to stabilize the QDs. Intermixing of the InAs in the QDs with Ga from the substrate was reported and elevated substrate temperatures likely increase the interdiffusion of In and Ga species [27]. Despite the fact that InAs QDs will accumulate Ga atoms during growth and annealing, Ga desorption was not observed in the above annealing studies as it has a high activation energy [27].

Altogether, ripening and desorption alter the structure of QDs and have to be considered as relevant processes already during QD growth, especially when small growth rates are employed. On the other hand, *in situ* annealing can be regarded as a powerful tool to control the size or the composition of self-assembled QDs after growth if high growth rates are used. Further properties such as QD shape or QD ordering are also influenced which extends the adjustable parameters. So far, *in-situ* annealing experiments have only been carried out with self-assembled QDs and a verification of the described mechanisms for positioned QDs is sought after in this work.

Two samples were prepared to provide first insights into the effects of *in situ* annealing on positioned QDs. AFM images of the as grown and the annealed sample are shown in figure 6.2 (a) and (b), respectively. The samples were prepared in the same way. Holes were fabricated using EBL and the oxide was removed using Ga-assisted deoxidation. After a quick thermal annealing of 2 min at 550°C the patterned substrate was overgrown with a 16 nm GaAs BL at a substrate temperature of 500°C. This was followed by the deposition of 1.8 ML of InAs at the same temperature. While the first sample was rapidly cooled down after QD growth, the second was kept at growth temperature for 2:30 min before being cooled down. The temperature ramp down after growth proceeded with a rate of 30°C/min with the substrate heater still being close to the sample. Temperature ramp down was reported to be critical with respect to the QD configuration [88]. Material redistribution was still observed at this stage due to a considerable amount of rest heat, possibly altering the QD properties. However, extracting a sample from the growth chamber right after growth in order to quench it to room temperature was not possible due to the high As background pressure in the growth chamber. Although some material redistribution might be present during temperature ramp down, the ramp rate was always kept constant so that reproducibility and comparability of different samples is assured. The As_4 BEP was kept around 3×10^{-6} Torr during growth and annealing. According to the calculations of *Heyn* this should result in an In sticking coefficient of $\alpha_{\mathrm{In}} = 1$ during growth.

In (a), nucleation of mainly two QDs is observed in the defined holes. Additional unintentional holes are also present which are caused by insufficient substrate surface cleaning prior to growth. This problem was addressed at a later stage of this work by improving the sample cleaning procedure, see chapter 4. A few QDs have formed around the defect holes and at other sites between the defined holes. The reason is the hight amount of deposited InAs being above the critical thickness for QD formation on flat GaAs surfaces. After annealing this QD configuration for 2:30 min, the QD distribution has changed. The two QDs per hole have merged into a single larger QD. These observations are confirmed by the values of the QD occupation in the corresponding AFM images. On average, 1.6 ± 0.8 QDs/hole are found on the as grown sample. More than 50% of the holes are occupied with two QDs, as seen in the QD occupation distribution in (c). After short annealing, the average number of QDs per hole has decreased to 1.0 ± 0.7 and more than 60% of the holes contain one QD. Besides the described morphological transition, the number of QDs found between the holes has decreased. To ensure this observation it is useful to compare the QD densities in the patterned area (QDs in hole + QDs between holes) with that outside the patterned area (not shown). For the as grown sample, the QD densities are roughly $n^{\text{on-site}}_{\text{as grown}} = 4.8 \times 10^9/\text{cm}^2$ and $n^{\text{off-site}}_{\text{as grown}} = 1.6 \times 10^9/\text{cm}^2$ in the patterned (on-site) and unpatterned (off-site) areas, respectively. For the annealed sample the densities are about $n^{\text{on-site}}_{\text{as grown}} = 2.6 \times 10^9/\text{cm}^2$ and $n^{\text{off-site}}_{\text{as grown}} = 0.9 \times 10^9/\text{cm}^2$. For both samples the QD density is about three times higher in the patterned area compared to the unpatterned one which relates to the site-selective nucleation of QDs. The difference in on-site QD density between the as grown and the annealed sample supports the above

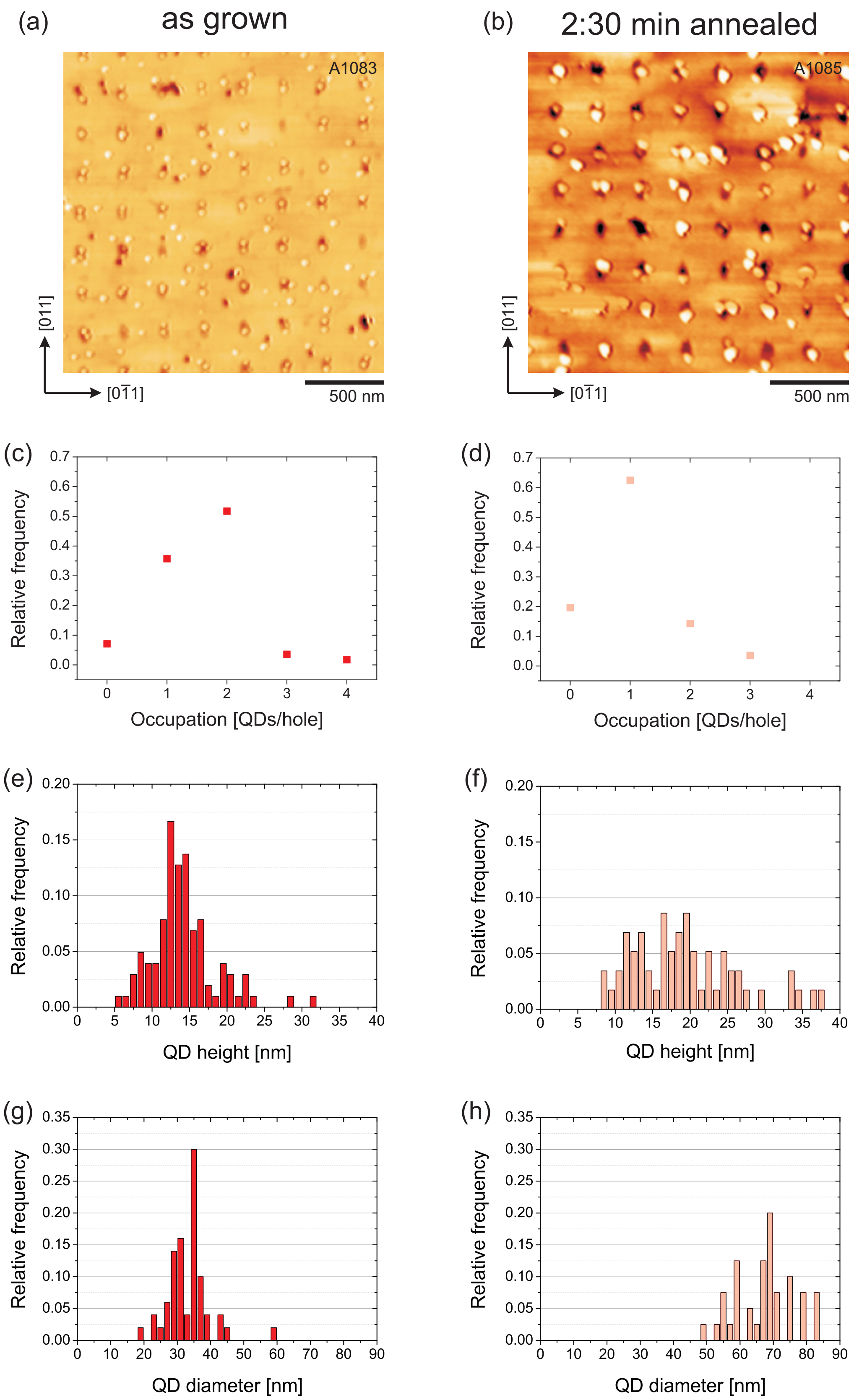

Figure 6.2 AFM images of as grown and *in situ* annealed sample. The QD occupation distributions, the QD heights and the QD diameters were extracted from the images. A redistribution of the deposited InAs is observed.

observation of the morphological transition. The merging of double dots into single QDs, as a consequence, reduces the density of QDs. The annealing step as well reduces the off-site density of randomly grown QDs by a factor of about 2. In correspondence, the on-site QD densities differ by a factor of about 2 because double dots merge into single dots and the number of random dots is halved.

The structural change of the QDs affects their size. The AFM images of (a) and (b) suggest an increase in QD size during short annealing, which corresponds to a ripening process. Large QDs grow at the expense of smaller ones which disappear. The temperature used during annealing is rather high. According to the work of *Hu*, a kinetic model is thus assumed for the ripening process, with ripening being limited by attachment and detachment of atoms on the QD surface [89]. The site-selective QD are more stable than the QDs nucleating in between the holes, which disappear during annealing. The larger size of the site-selective QDs could account for that fact, but also the surface curvature due to the hole is likely to affect the diffusion of In adatoms since this is the initial reason for site-selective growth. The increase in QD size after annealing is support by the histograms in (e), (f), (g) and (h). The QD height distribution of the as grown sample in (e) exhibits a peak around 13 nm and the average QD height amounts to $14.2 \pm 4.3\,\mathrm{nm}$. The QD height distribution of the annealed sample in (f) has broadened significantly but it has also shifted to higher values. This is reflected by the average QD height of $19.3 \pm 7.1\,\mathrm{nm}$, which has a much larger absolute standard deviation. The behavior of the lateral QD size is similar. The distribution of QD diameters in the as grown sample is shown in (g). A maximum is observed around 35 nm and the distribution is quite narrow. The average QD diameter is $33.4 \pm 6.3\,\mathrm{nm}$. After short annealing, the QD diameter distribution becomes broader and shifts to higher values, as seen in (h). The corresponding average diameter of annealed QDs is $67.4 \pm 8.6\,\mathrm{nm}$. The QD diameters were extracted from the AFM images after deconvolution of the tip shape (assumed tip radius of 20 nm at apex). Assuming a dome-like shape consistent with the TEM analysis in chapter 5 it is possible to calculate the average volume of the positioned QDs by $\overline{V} = 1/2 \cdot 4/3 \cdot \pi \overline{h}(\overline{d}/2)^2$. The average QD height is denoted as $\overline{h}$ and the average QD diameter as $\overline{d}/2$. The average volumes of as grown and annealed QDs are then $\overline{V}_{\text{as grown}} = 8300 \pm 2700\,\mathrm{nm}^3$ and $\overline{V}_{\text{annealed}} = 46000 \pm 29000\,\mathrm{nm}^3$. The volume of the annealed QDs is hence larger than that of the as grown QDs. However, due to the large standard deviation it is difficult to answer the question if the average amount of InAs per hole is larger after annealing. This would then point to the fact that In desorption is not significant at this stage of annealing and ripening dominates the QD evolution.

The potential of this annealing procedure to improve the material distribution and to act on the QD size is further illustrated by the sample depicted in figure 6.3. It consists of a 16 nm thick GaAs BL grown on top of a patterned substrate followed by the deposition of 2.6 ML of InAs. The QDs were then annealed for 7:30 min. Growth and annealing temperature were both around 500°C. The BEP of the As_4 flux was again about 3×10^{-6} Torr during growth and annealing. Despite the high amount of provided InAs which necessarily leads to the formation of many QDs between the defined holes, after annealing well localized QDs are observed in the AFM image in (a). Almost no unintended QDs are left on the 250 nm array. Essentially all holes are occupied with QDs, whose sizes, however, differ quite significantly. Two sets of QDs can be distinguished according to the QD height and size histograms presented in (b). Small QDs with a height of about 4 nm and larger ones with a height of roughly 16 nm are found (corresponding to the maxima in the QD height distribution). Maxima in the QD diameter distribution are seen around 35 nm and 55 nm. Apparently, some of the QDs were subject to ripening during the whole annealing

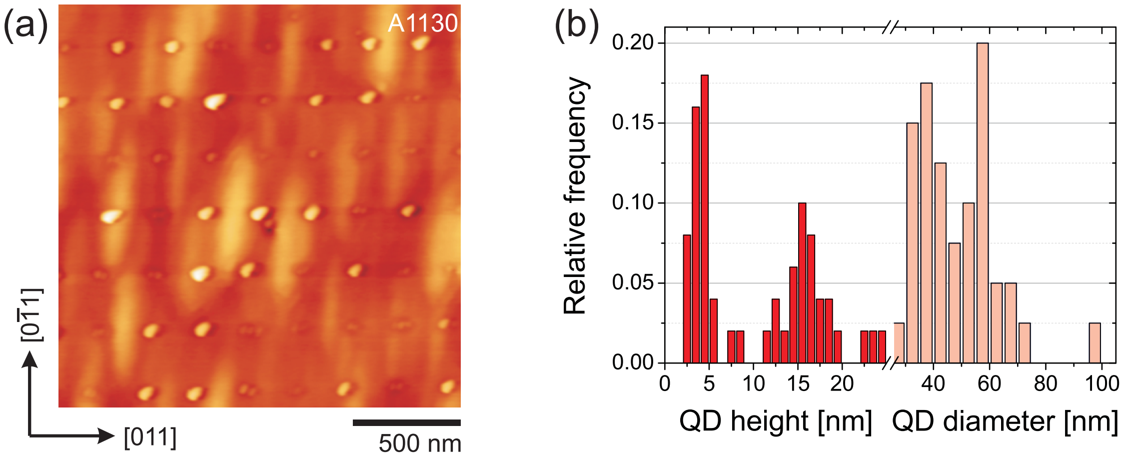

Figure 6.3 A large amount of InAs was deposited (2.6 ML) followed by a long annealing of 7:30 min. After annealing well localized QDs are revealed in the AFM image in (a). The QD heights and diameters are shown in the histogram in (b).

process whereas the evolution of others took a different path. Connecting these results to the above observations it is found that *in situ* annealing opens a way to control the QD distribution. While positioned QDs are stable, surrounding unintentional QDs can be removed by implementing a proper annealing recipe. Choosing the right growth and annealing parameters, it should then be possible to extend this mechanism to sparse arrays with larger spacing in order to obtain arbitrary QD configurations. To gain a deeper understanding of the annealing effects on positioned QDs and to further strengthen the findings the evolution of positioned QDs during *in situ* annealing was studied and changes in terms of QD size and distribution were quantified.

6.2 Evolution of quantum dots during annealing

Three samples were prepared under similar conditions. First, several hole arrays with different hole sizes and spacings were fabricated on a GaAs substrate by EBL. An electron beam with a beam energy of 100 keV was used for the exposure in order to increase the hole size uniformity. A representative part of an 250 nm array is shown in the SEM image of figure 6.4 (a). The originally circular holes in the resist transform into rectangular holes in the GaAs sample due to preferential etching of $\{1\,1\,1\}$ facets. Furthermore, the holes are elongated in the $[0\,\bar{1}\,1]$ direction. This is related to unequal etch rates in perpendicular crystal directions for GaAs, as described earlier. The depicted holes are 72 ± 3 nm long, 63 ± 5 nm wide and about 30 nm deep. Altogether, arrays with spacings of 250 nm, 500 nm, 1000 nm and 2000 nm were fabricated and the hole length (width) varied between 51 ± 3 nm (44 ± 3 nm) and 72 ± 3 nm (63 ± 5 nm). The increased uniformity due to the higher electron beam energy is revealed in the low fluctuation of hole sizes which is less than 8%. Before growth of the QDs the native oxide was removed using Ga-assisted deoxidation after which the samples were heated up to 580 °C for a quick annealing and then cooled down to the growth temperature of 500 °C. A 20 nm GaAs BL was then grown on the patterned substrate to reduce the surface roughness of the etched areas. The enhanced mobility of Ga adatoms in the $[0\,1\,1]$ and $[0\,\bar{1}\,\bar{1}]$ directions leads to a deformation of the holes with an elongation occurring in these directions. The deposition of 1.7 ML InAs then entails the formation of QDs localized inside the defined holes and aligned along the

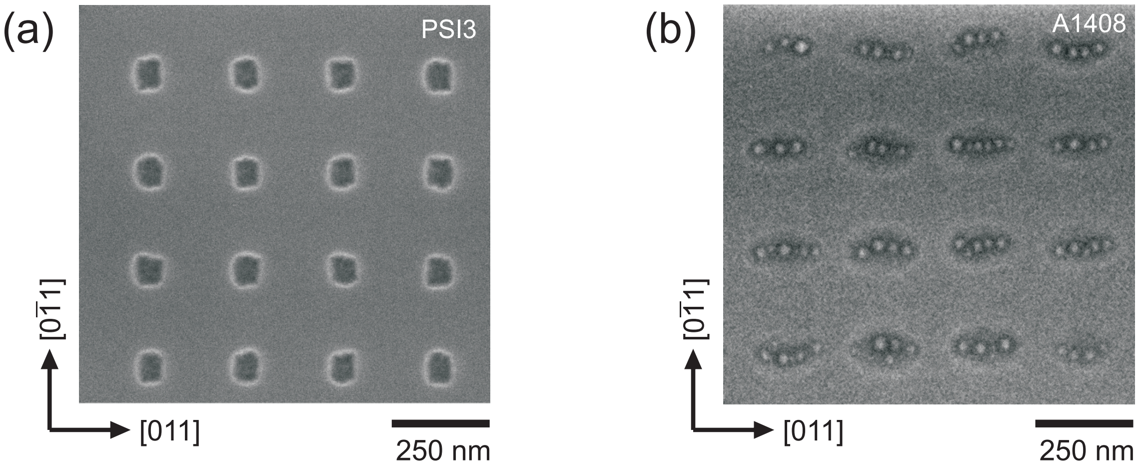

Figure 6.4 A hole array is depicted in the SEM image in (a) after etching. Elongation of the holes due to preferential etching is observed. A similar array after overgrowth with a thin GaAs BL and InAs QDs is shown in the SEM image in (b). The BL growth leads to a change in the orientation of the hole elongation.

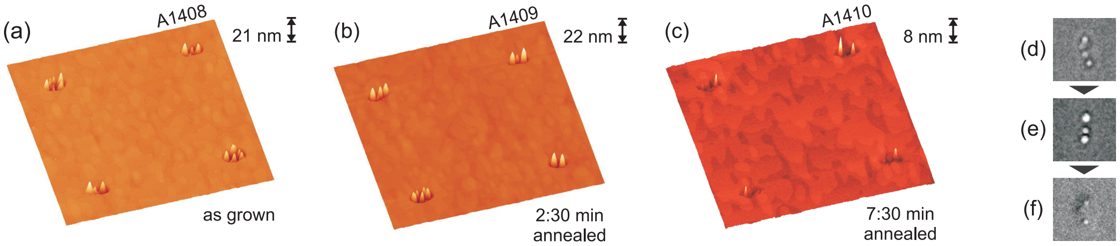

Figure 6.5 Representative AFM (a)-(c) and SEM (d)-(f) images of positioned QDs showing the evolution of QDs during in-situ annealing at different stages: as grown (a), (d), after 2:30 min annealing (b), (e), after 7:30 min annealing (c), (f). The spacing between QD positions is 1000 nm, the z-scale of the AFM images is given next to these and the size of the SEM images is 250 nm × 250 nm.

elongated direction. The elongation occurring during BL growth is thus perpendicular to that obtained from wet etching, as seen by comparing the SEM images in (a) and (b) which have the same orientation. The SEM image in (b) shows a part of a sample after QD growth on a hole array similar to that in (a). In a last step, the samples were annealed at growth temperature for several minutes under high As background pressure before being rapidly cooled down. It is important to notice that the growth rate for the QDs was rather high with 0.068 ML/s. This is to separate the QD growth from the processes taking place during annealing. The evolution of the QDs and their distribution due to *in situ* annealing was analyzed *ex situ* by AFM and SEM.

The AFM and SEM images in figure 6.5 show the three samples which are as grown, annealed for 2:30 min and annealed for 7:30 min. The QDs are well located at the defined positions which are 1 µm apart. Considering the z-scale of the images (a)-(c) it seems that the QD height slightly increases for short annealing times and then decreases for longer annealing times. At the same time, the number of QDs per dip constantly decreases. The SEM images (d)-(f) suggest that the QD diameter evolves like the QD height with a slight increase for short annealing times followed by a decrease for longer annealing times. A quantification of these observations is given in the following sections.

6.3 Quantification of the change in quantum dot distribution and size

For a quantitative analysis of the QD evolution during *in situ* annealing several properties are evaluated: the QD occuption per site, the QD size and the QD shape aysmmetry. All these properties are relevant for integration of positioned QDs in devices as they influence the interaction between the QDs and their environment.

6.3.1 QD occupation

To begin with, the influence of the hole size, the hole spacing and the hole arrangement on the QD occupation is measured for the as grown sample. The diagrams in figure 6.6 show the average QD occupation with respect to different initial hole sizes for several hole spacings. The holes were arranged on a square grid. Due to the asymmetric hole shape the hole length is given and ranges between about 60 nm to 72 nm. Smaller holes, although being fabricated during EBL, were not analyzed since they were essentially filled up during GaAs BL growth. The diagram in (a) refers to the 250 nm array. The average QD occupation is below 1 QD/hole for all hole sizes. Despite the large fluctuations in hole size and therefore in QD occupation a slight trend is visible with higher occupation for larger holes. The average number of QDs per hole increases from 0.5 to 0.8. The values of the diagram in (b) were extracted from the 500 nm array. Here, the trend is more pronounced with an increase in QD occupation from 2.1 QDs/hole for the smallest holes to 3.4 QDs/hole for the largest holes. In addition, the average QD occupation is significantly higher at each site compared to the smaller spaced pattern. Further increasing the hole spacing to 1000 nm produces a similar behavior, see (c). The QD occupation increases from 2.0 QDs/hole to 4.6 QDs/hole but then slightly decreases again to 4.5 QDs/hole. The reason for the final decrease is not understood, but considering the large fluctuations in QD occupation and hole size it is advisable to not over-interpret small deviations. Nevertheless, the general trend of increasing QD occupation with increasing hole size is confirmed on that array as well. Larger holes have a larger volume and can therefore accumulate more InAs than smaller holes during QD growth. Furthermore, they can simply host more QDs due to their larger surface. Both, hole size and hole spacing can thus be used to adjust the QD occupation in a certain range. In the following treatment, the evaluation is based on QDs that have formed in the largest holes presented. Since the largest holes contain the highest available number of QDs, it is expected that annealing effects on the QD occupation will be most effective here.

Next, the influence of the hole arrangement on the QD occupation is investigated. Two different arrangements were defined, a square grid and a hexagonal grid. The average QD occupation depending on the hole spacing is shown in figure 6.7 (a) for the two arrangements. Again, the QD occupation increases continuously with the hole spacing up to 1000 nm. Beyond that pitch, no further increase is seen which is related to the fact that a particular hole size can only allow for a maximum number of QDs. This maximum number of QDs that a hole of the given size can accommodate on average is close to five in this case. The general trend is the same for both arrangements, but a small difference is visible. The average QD occupation is slightly higher by about 0.3 QDs/hole on the hexagonal array. This is surprising since the number of holes per unit area is larger in the hexagonal array. With the hole spacing d the hole density in the square array is given by $1/d^2$ while it is $2/\sqrt{3} \cdot 1/d^2$ in the hexagonal array. The fact that the QD occupation rises with increasing hole spacing is equivalent to an increase with decreasing hole density.

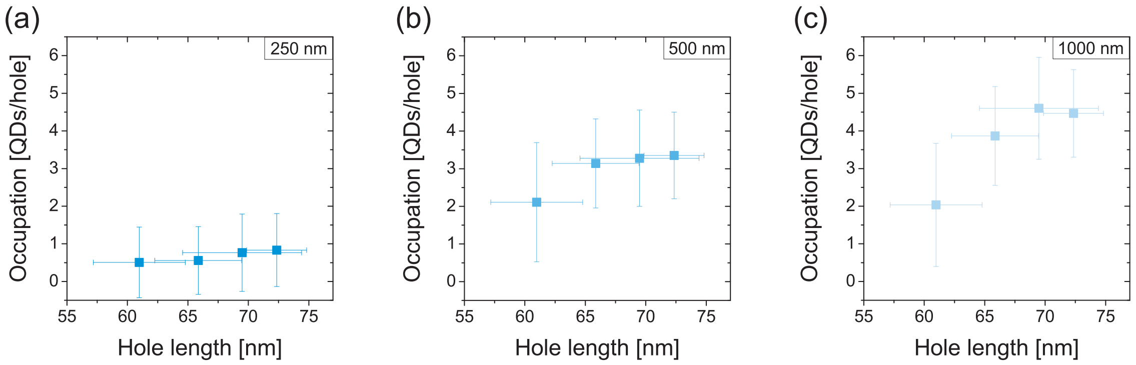

Figure 6.6 The average QD occupation was measured with respect to the lateral hole size. The hole spacing was 250 nm, (a), 500 nm, (b), and 1000 nm, (c). Both larger holes and larger hole spacings promote an increase in QD occupation.

Therefore, the higher average QD occupation on the hexagonal array must be related to the arrangement because the higher hole density should lead to a lower average QD occupation. Apparently, the hexagonal arrangement enhances the accumulation of InAs so that more QDs can be formed in holes of the same size as on the square array. One possible explanation could be the distance between a particular hole and its neighbors along the main crystallographic directions, i.e. $[0\,1\,1]$ and $[0\,\bar{1}\,1]$. It is assumed that the In adatom migration, which leads to the accumulation of InAs in the holes, is very effective along these axes. In the case of a square array, the distance to the nearest neighbors along these axes corresponds exactly to the hole spacing d, as illustrated in (b). In the hexagonal array, this is only true for one of these directions. The distance to the nearest neighbors in the other direction is larger, namely $\sqrt{3}$ times the spacing. Hence, In adatoms can be attracted from further away so that slightly more material can be accumulated despite the denser array.

After having analyzed the QD occupation with respect to the most important pattern parameters, the effect of the annealing process on the QD occupation is considered next. For a better overview, only the data obtained from the square array are shown. All observations also hold for the hexagonal array, with a slightly higher average QD occupation being the only difference. Figure 6.8 shows the average QD occupation per defined hole depending on the spacing (pitch) between the holes for different annealing durations. The average QD occupation for the densest array (250 nm) of the as grown sample lies below 1 QD/hole. This means that some of the holes remain unoccupied. That is due to the amount of deposited InAs which is not enough to form QDs inside each hole of the dense array. The QD occupation strongly rises with increasing pitch because of the larger available reservoir of In per hole. At a spacing of 500 nm an average of 3.0±1.2 QDs is found per hole which is exceeded by 4.5±1.1 QDs/hole for a pitch of 1000 nm. For larger spacings, a significant increase is not observed any more, as an average of 4.7±1.4 QDs occupies each site of the 2000 nm spaced array. As described above, the size of the hole likely defines an upper bound for the number of QDs which can nucleate inside the hole. The second reason for that upper limit probably is the diffusion length of In adatoms which is estimated to be not much more than 1 µm.

After annealing for 2:30 min the QD occupation decreases for all spacings. The decrease is strongest for the 500 nm spaced array where the QD occupation drops below 1 QD/hole. Nonetheless, the dependence of the QD occupation on the array spacing remains unchanged since the decrease of the number of QDs per hole is similar for both 1000 nm and 2000 nm

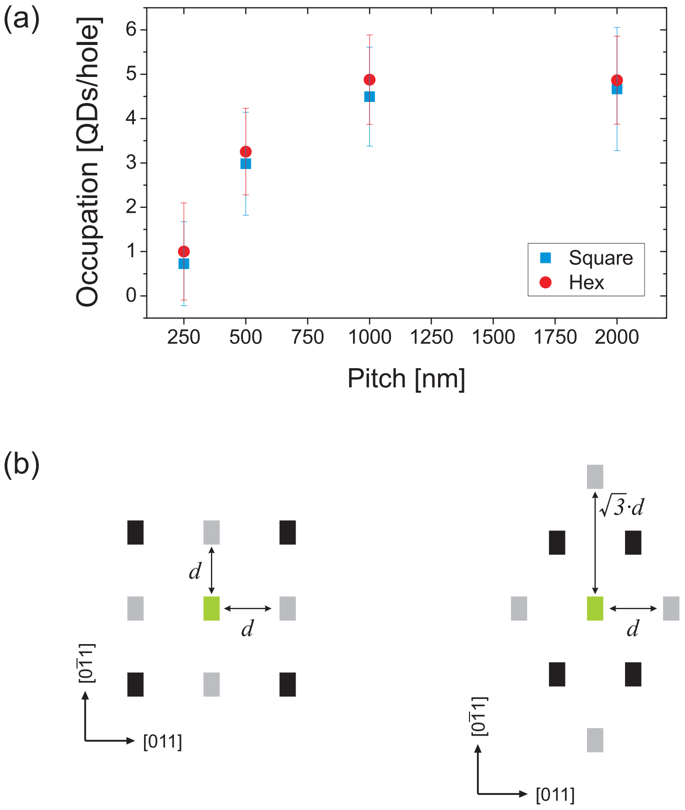

Figure 6.7 The dependence of the average QD occupation on the pattern geometry was tested for different hole spacings, (a). Although the hole density is higher on the hexagonal array, the average QD occupation is higher compared to the square array. A possible explanation is illustrated in (b), where the distance to nearest neighbors on the hexagonal array is larger than on the square array in one direction.

pitches. The standard deviations of the average values have become smaller which is an advantage when trying to obtain uniform positioned QD ensembles. Even longer annealing for 7:30 min leads to a further decrease of the QD occupation with the result that the arrays become sparsely filled since the average occupation drops below 1 QD/hole for all spacings. The differences in QD occupation for the various hole spacings fade, especially after longer annealing. The overall reduction in QD occupation is in agreement with the earlier observation where two QDs merged into a single one. However, in order to determine whether pure ripening takes place or if desorption is also effective the evolution of the QD size has to be considered.

The relative frequency of QD occupations refers to the percentage of holes which are occupied with a certain number of QDs. It is a measure for the degree of control that is achieved by site-selective growth. This quantity is depicted in figure 6.9 for the 1000 nm spaced array. The QD occupation distribution is given depending on the number of QDs per hole for different annealing times. For the as grown sample, all holes are occupied but the occupation distribution is rather broad, ranging from 2 QDs/hole to 7 QDs/hole, with a maximum at 4 QDs/hole. The width of the distribution reflects the corresponding large standard deviation to the average QD occupation in figure 6.8. Despite the high resolution EBL leading to little fluctuation in hole sizes, the holes change their shape during BL overgrowth. As shown in chapter 5, the broadness of the distribution is not improved during BL growth but rather increased for thicker BLs. Therefore, it is assumed

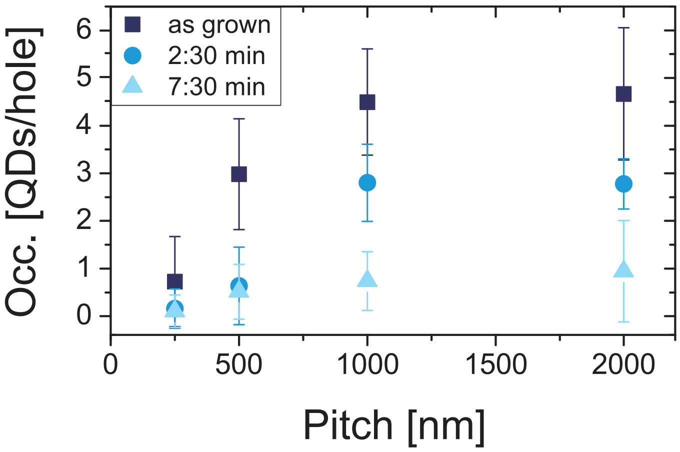

Figure 6.8 Evolution of average QD occupation during annealing. The average number of QDs per hole with respect to the hole spacing (pitch) is plotted for different annealing times. The occupation is continuously reduced throughout the annealing process.

that originally small hole size fluctuations are enhanced during BL growth and finally account for the large distribution of QD occupations. When annealed for 2:30 min the distribution shifts to lower occupation numbers and narrows such that more than 40% of the holes are occupied with three QDs. This is consistent with the decrease in average QD occupation and its associated variation. Still, all holes are occupied. This changes for longer annealing times. When annealing the sample for 7:30 min a large fraction, almost 40%, of holes becomes unoccupied. However, the QD occupation distribution has further narrowed and more than 50% of the holes are now occupied with one QD. The power of annealing to alter and even improve the occupation distribution is hence demonstrated.

6.3.2 QD size

The size evolution of positioned QDs during annealing on differently spaced arrays was investigated. SEM images were analyzed to extract information on the QD diameter while height information was obtained from AFM data. Three plots of the QD diameter over annealing time for different pattern spacings (250 nm, 500 nm, 1000 nm) are shown in figure 6.10 (a). The average QD diameters on the 250 nm and 500 nm spaced arrays are almost equal with 22.0±4.7 nm and 22.5±4.6 nm, respectively. The width of the size distribution (the standard deviation is a little more than 20%) is higher than that of random self-assembled QDs presented earlier where a standard deviation of about 10% was measured, see chapter 5. However, the results are comparable to data for self-assembled QDs published in literature [29], which indicates good growth conditions. The average diameter on the 1000 nm spaced array is slightly larger with 24.8±5.5 nm. This difference could be explained by the amount of In available for the site-selective QDs. The sparse array inherently has a lower density of defined nucleation sites. This leads to a lower QD density as well. However, the deposited amount of In is equal on each array. Thus, the reservoir of In available for each QD is higher for increased spacing which then allows for the observed increase in QD size. This behavior is based on the diffusion of In adatoms and similar to the increase in QD occupation with hole spacing. If the spacing becomes larger than the diffusion length there should be no further increase in QD size. Indeed, the average QD diameter on a 2000 nm spaced array (not shown here) is 25.3±6.1 nm and therefore comparable to that of the 1000 nm spaced array. This indicates a diffusion length

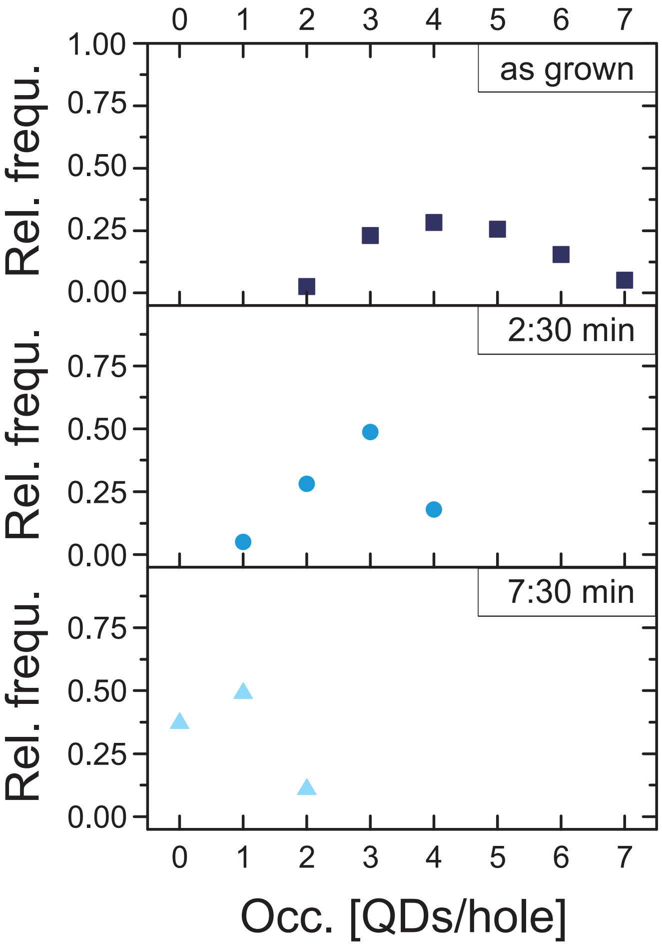

Figure 6.9 The distribution of different QD occupations is given with respect to the occupation number for different annealing times. The distribution shifts to lower QD occupation values and becomes narrower. The array spacing was 1000 nm.

of In adatoms which is not much more than 1 µm for the given growth conditions.

After 2:30 min of annealing the average QD diameter has increased on all arrays. The values are now closer together, ranging between 28.5 nm to 29.5 nm. The width of the QD size distribution has not significantly changed. The gain in size after short annealing can be explained by a ripening process if the standard ripening theory of particles introduced above is used. QDs with diameter D larger than a critical diameter D_{crit} grow in size at the expense of smaller QDs with $D < D_{\text{crit}}$ which dissolve. According to *Hu et al.* the In content of the QDs determines their evolution [29]. The high In content of the QDs at the beginning of annealing leads to a small critical diameter such that ripening occurs. In the course of annealing, In can, due to the high temperature, either desorb or interdiffuse with the GaAs matrix. In both cases the In content of the QDs is reduced which entails an increase in D_{crit}. Eventually, D_{crit} becomes larger than the maximum QD diameter so that ripening is inhibited. Indium desorption and interdiffusion, however, will continue and therefore determine the subsequent QD evolution. In this context, the observed increase in QD diameter is related to the described ripening process. The observed reduction of the number of QDs per hole confirms this explanation. The average QD occupation decreases by more than 40% during short annealing but the QD diameter increases by at least 15%. Together with an increase in QD height, seen in (b), the increase in average volume of

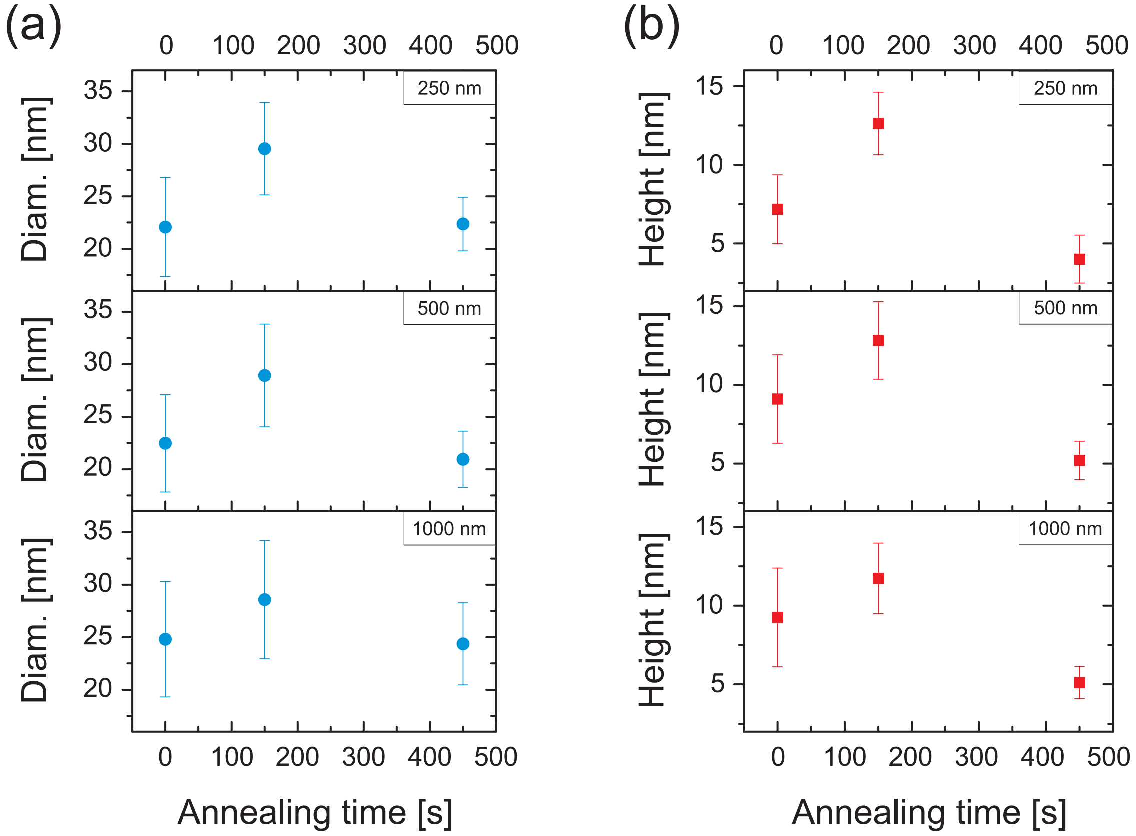

Figure 6.10 Evolution of QD size during annealing. The average QD diameter is given with respect to annealing time for different hole spacings, (a). The average QD height of the corresponding samples is plotted over annealing time, (b). Both average QD diameter and height increase for short annealing times and decrease for longer annealing.

the QDs becomes larger than the decrease in QD occupation. Hence, desorption might be present but the ripening process dominates the QD evolution for short annealings and further In is accumulated from the surrounding of the holes, which is suggested by the larger amount of InAs contained in the positioned QDs after short annealing. The third sample was annealed for 7:30 min. A strong reduction of the QD diameter is observed on all arrays with the average diameters dropping down to or even below the initial values. The width of the size distribution (standard deviation) has narrowed by a factor of almost two. According to the works of *Hu* on self-assembled QDs, In desorption was only observed for short annealing times up to 3 min and interdiffusion was identified as main driving force for the subsequent QD evolution [20, 29]. She observed a continuous reduction in self-assembled QD density during the course of *in situ* annealing at high temperatures while the average QD volume strongly decreases at the beginning but is then rather stable beyond an annealing time of 2:30 min. Such behaviour cannot solely depend on interdiffusion, since it does not explain why some QDs disappear and others do not. It is more likely, that a very narrow window was found in which ripening and desorption are very balanced. The ripening process decreases the QD density while the In desorption keeps the size of the resulting QDs more or less constant. The fact that In desorption was not identified during film force measurements is probably related to the fact that In desorption from the InAs wetting layer is mainly measured. Hence, the annealing conditions in the underlying work were slightly different from the ones employed by *Hu* [20, 29], with mainly ripening being dominant at short annealing times and desorption becoming pronounced for longer annealing.

Analyzing the corresponding average QD height for the given annealing times and the different array spacings helps to extend the above findings. The evolution is depicted in figure 6.10 (b) and is comparable to that of the average QD diameters. The average QD heights initially range between 7-9 nm and slightly depend on the array spacing, with larger heights for larger spacings. After short annealing times a clear increase in the average QD height up to about 11-13 nm is observed which is caused by dot ripening. For longer annealing times the average QD height drops to 4-5 nm which is below the original value. Indium is not equally distributed inside the QDs. The In concentration is higher at the top of the QDs so that In mainly desorbs from that part [27]. This could explain the relative change in height being larger than that of the diameter. As for the average diameter evolution, the width of the height distribution (standard deviation) is decreased for long annealing times.

Two annealing regimes were identified. The QD evolution is mainly governed by a ripening process for short annealing times while In desorption becomes dominant at longer annealing times. The change in the QD evolution is related to the In content in the QDs. Desorption and interdiffusion continuously decrease the In content such that the critical diameter for QD ripening D_{crit} becomes larger than the largest QD diameter at some point. Beyond that point, ripening is not possible any longer. The analysis proves that it is possible to control the size of positioned QDs after growth by employing an adequate annealing recipe. Both increase and decrease in QD size can be achieved by adjusting the annealing time.

6.3.3 QD shape asymmetry

When looking more closely the QDs might not be perfectly round shaped. *Riotte et al.* found as grown self-assembled QDs with a shape elongated along the $[0\,\bar{1}\,1]$ direction [30]. Furthermore, they observed a shape transition during annealing to symmetric QDs. In order to analyze the asymmetry of the QD shape SEM images were taken to fit ellipses to the QDs using the free software ImageJ [76]. Minor and major axes of the fitted ellipses are automatically extracted as well as the orientation of the ellipse. The evolution of the QD shape asymmetry during annealing for different array spacings is shown in figure 6.11. The average ratio of minor axis and major axis is plotted over annealing time. Min. ax./Maj. ax. = 1 would correspond to a perfectly round shaped QD. Before annealing the average ratios range between 0.75-0.8 and slightly decrease with increased spacing. The QDs are thus elongated and not symmetrically shaped. In addition, the elongation occurs approximately in the $[0\,\bar{1}\,1]$ direction and is therefore perpendicular to the hole elongation after BL growth. After short annealing the average ratio of the ellipse axes increases for the 500 nm and 1000 nm spacings and slightly decreases for the 250 nm spacing. Longer annealing leads to a further increase of the ratio up to 0.83-0.87 for all spacings. At the same time the standard deviation of the ratios constantly decreases during annealing. This is related to the increased size homogeneity described in the previous section. The reason for the original QD elongation is found in different diffusion barriers for In adatoms along the two orthogonal $[0\,1\,1]$ (high barrier) and $[0\,1\,\bar{1}]$ (lower barrier) surface directions [90] and eventually leads to QD alignment in chains on flat GaAs substrates [91]. A reduction in shape asymmetry is then attributed to a compensation of the limited diffusion length during annealing [30]. Thus, it is possible to control, to some extent, the shape of positioned QDs during *in situ* annealing.

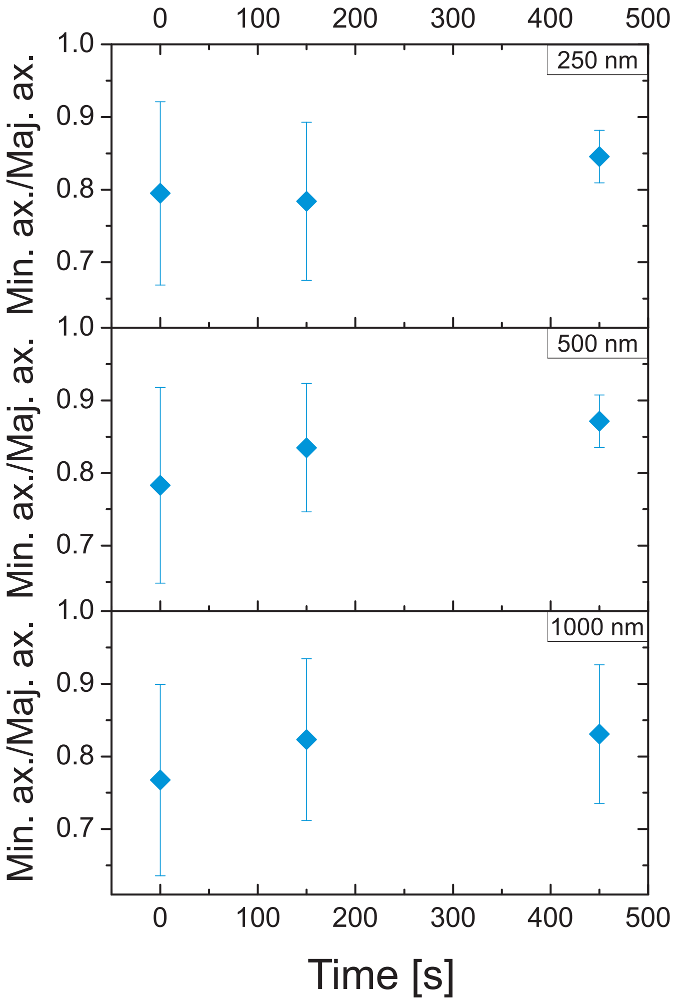

Figure 6.11 Evolution of QD shape asymmetry during annealing for different spacings. The QD shape is approximated by an ellipse. The ratio of minor and major axis describes the deviation from a round shaped QD (Min. ax./Maj. ax. = 1). The QDs become slightly more symmetric in the course of *in situ* annealing.

6.4 Large scale analysis of site-selective quantum dot arrays before and after annealing

So far, the investigation of annealing effects was restricted to a small part of the pattern. This is enough to extract information on the QD occupation or the QD size. Ordering effects occurring on a small scale can, however, not be revealed this way. In addition, information on the evolution of QDs on a large scale are not accessible. Monitoring shape and strain of the QDs would help understanding the processes during annealing in more detail. A powerful technique to investigate these properties is high resolution X-ray diffraction (HRXRD). It was widely applied to study laterally ordered nanostructures in a non-destructive fashion [79]. *In situ* annealing effects on self-assembled QDs were also examined in the past and provided information on QD ordering, QD shape and strain evolution [30]. However, a combined study was not performed so far.

Two measurement techniques are appropriate to access information on different QD properties. The Grazing incidence diffraction (GID) is sensitive to the lateral lattice parameter and is therefore mainly used to study the in plane strain at the substrate surface. Due to the larger lattice constant of InAs compared to GaAs the formation of QDs is accompanied by a particular strain profile in the QD but also in the underlying substrate. Measuring this strain profile by GID allows to retrieve information on the QDs as the strain will depend on In content, QD size, QD shape, etc. HRXRD measurements in GID geometry are based on the effect of total external reflection. When the X-ray beam impinges on the surface of the crystal below a certain grazing angle it will be completely reflected and only an evanescent wave will penetrate into the sample. As a result, the scattering volume is concentrated in a very thin layer at the surface which makes GID a powerful tool to investigate nanostructures at the surface. The depth sensitivity can be controlled by adjusting the incident angle, with higher angles leading to deeper penetration. The emerging diffraction pattern contains information about strain and effective shape of the scattering volume which are entangled with each other. In case of a regular arrangement of nanostructures, the diffraction pattern will further be superimposed by a periodic signal reflecting the order of the nanostructures. Hence, adequate methods are required in order to decompose the signal into the different contributions. The most widely used model for the interpretation of GID patterns is the iso-strain scattering model [92]. This model considers the scattering volume to be composed of a stack of iso-strain layers with average lattice parameter. The second measurment technique which enables the study of surface nanostructures is called grazing incidence small angle X-ray scattering (GISAXS). The X-ray beam impinges under a grazing angle on the sample surface and is scattered by the surface nanostructures. The forward scattered parts of the beam are detected under a small angle. This method allows to study the spatial ordering and the shape of the scatterer without strain-induced contributions to the signal. This method is as well based on the total external reflection and benefits from very high intensities of the specular reflected beam. Short exposure times can be achieved this way, which is useful when studying the temporal evolution of QDs during *in situ* annealing.

The structure of the samples used in HRXRD measurements is depicted in figure 6.12 (a). It was designed to specifically investigate the QD array without any contribution from other parts of the sample. EBL was used to create the hole array. Since the exposure time scales quadratically with the array width the size of the array cannot be made arbitrarily large. As a result, the samples consisting of a quarter of a 2” wafer could not be completely covered with holes. Instead, a 500 µm × 500 µm large mesa was defined by EBL at the center of each sample on top of which the hole array was fabricated. The parts of the sample surrounding the mesa were covered with a gold (Au) layer. As before, a 20 nm GaAs BL was grown before the deposition of about 1.7 ML of InAs. The Au cover around the mesa inhibits the formation of an epitaxial GaAs film and the subsequent formation of QDs so that only the surface of the mesa is of mono-crystalline quality. As a consequence, only site-selective QDs on top of the mesa will contribute to the diffraction pattern and the intensity of a possible background is reduced to a minimum. The exact fabrication procedure for the samples can be found in the appendix. Two orientations of the hole array were defined. First, the square array was aligned along the $\langle 0\,1\,1 \rangle$ directions, as before. In order to reveal possible dependencies of the annealing process on the pattern orientation the square array was rotated by 45° so that the main axes of the array were aligned to the $\langle 0\,0\,1 \rangle$ crystal directions. Both orientations are schematically shown in (b). The spacing between the holes is 250 nm in order to ensure a high QD density and no QD nucleation between the holes, which would lead to a disturbing background signal.

The HRXRD measurements were performed at the surface diffraction beamline ID03 of the European Synchrotron Radiation Facility (ESRF) in Grenoble, France. A set of samples

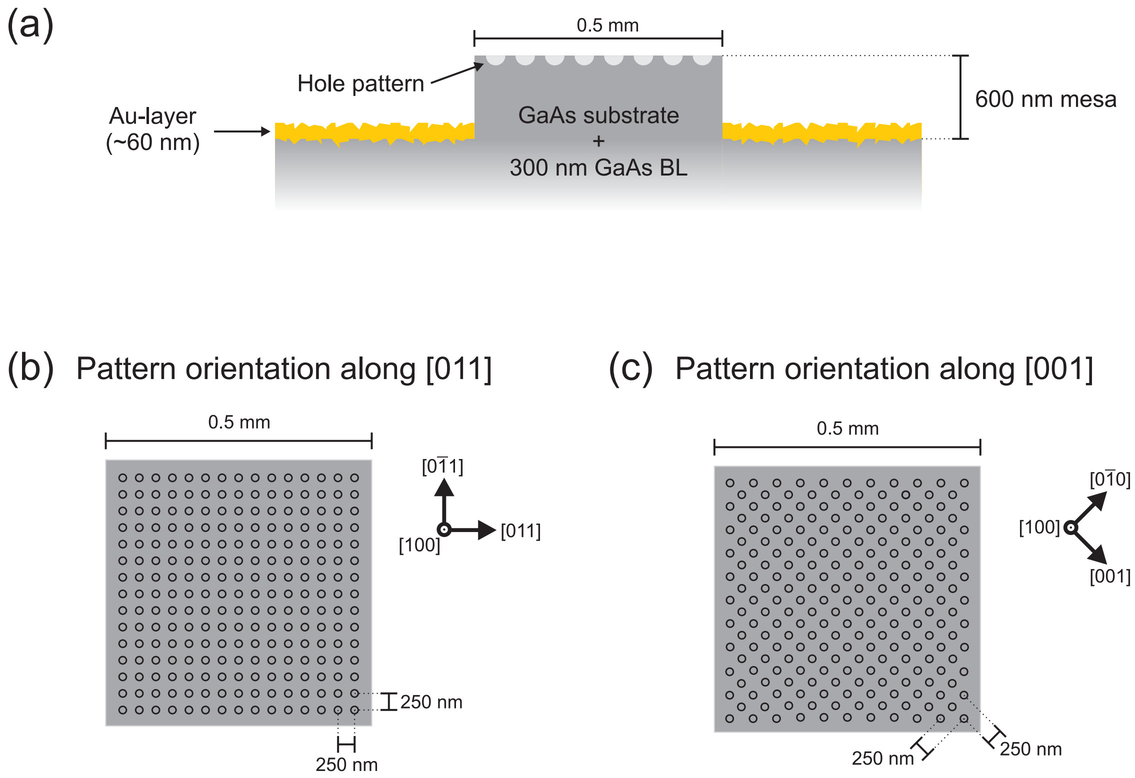

Figure 6.12 Sample layout and pattern orientation for the HRXRD experiments. The sample profile is depicted in (a). A mesa was fabricated on top of which a regular hole array was defined. The parts surrounding the mesa were covered with a Au layer. Two pattern orientations were defined. The normal alignment along $\{0\,1\,1\}$ directions is shown in (b) and the same array rotated by 45° is shown in (c).

was prepared and grown at KIT and measured *ex situ* at the beamline. Another set was prepared the same way but carried in a portable MBE chamber under UHV conditions to the synchrotron, which allowed for *in situ* characterization of the annealing process. The samples were grown in the stationary MBE system at KIT and immediately transferred to the portable MBE chamber after growth. The portable chamber was connected to the UHV of the stationary system so that the samples were not exposed to air after growth. This prevented the samples from oxidation and allowed for *in situ* annealing experiments in the portable MBE system at ESRF by heating up the samples to a desired temperature under As background pressure. A focused X-ray beam (spot size $50\,\mu\mathrm{m} \times 50\,\mu\mathrm{m}$) with $E = 13\,\mathrm{keV}$ ($\lambda = 0.1\,\mathrm{nm}$) was used at a grazing incoming angle of $\alpha_\mathrm{i} = 0.5°$ for both *ex situ* and *in situ* HRXRD measurements.

A full polar GISAXS scan of a QD array oriented along $\langle 0\,1\,1 \rangle$ is depicted in figure 6.13 (a). It was obtained by rotating the sample around the surface normal while successively recording GISAXS images. The polar scan corresponds to a reciprocal space map of the QD array. The highest intensity is observed at the center and is related to the specular reflection of the incident beam. The pattern observed in reciprocal space is related to the periodic arrangement of holes and, possibly, QDs. The highly ordered pattern in (a) reflects the high quality of the fabrication process. An AFM scan of the investigated sample is shown in (c). The amplitude signal is depicted for better contrast. QDs are well localized in the holes with several QDs arranging in a chain in each hole. The average QD occupation amounts to 3.2 ± 1.1 QDs/hole and more than 70% of the holes are occupied with 3 or 4

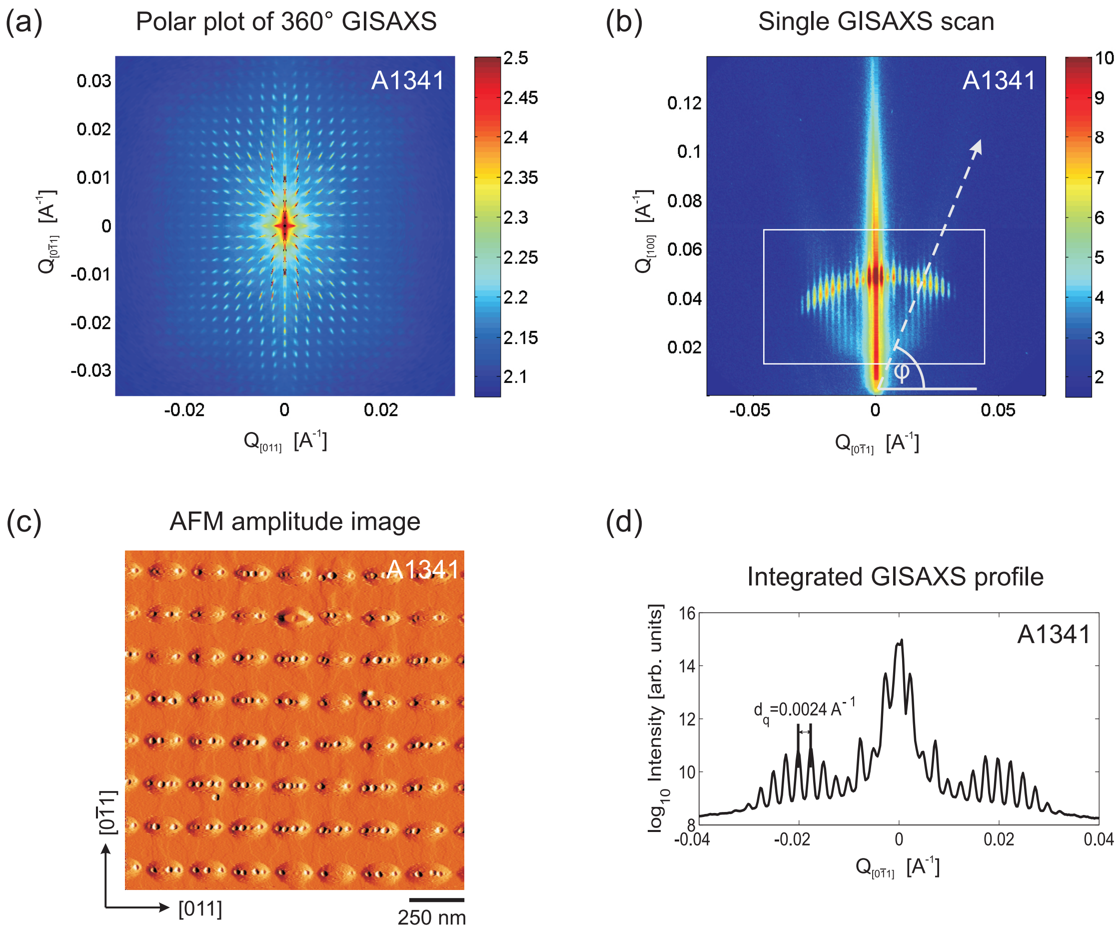

Figure 6.13 A full polar GISAXS plot is shown in (a). The regular hole array is observed in reciprocal space. A single GISAXS scan is depicted in (b). Next to the central truncation rod, a chevron is observed. The surface of the measured sample is depicted in (c). The AFM amplitude signal is shown for better contrast. The signal in the white frame was integrated in the vertical direction so that the intensity profile could be obtained, see (d). The separation between the periodic peaks corresponds to the reciprocal spacing of the holes in real space. The intensities in the GISAXS maps are given in log-scale.

QDs. A single GISAXS scan is shown in (b). It shows a diffraction pattern which is normal to the surface. The sample was irradiated along the $[0\,1\,1]$ direction and hence parallel to the long axis of the holes. The central feature is a so called truncation rod (TR) being the result of the scattering off a surface instead of a 3D crystal. It is related to the specular reflection. The periodicity of the pattern is translated into the periodic modulation of the signal. Besides the maximum intensity of the TR side maxima are observed along streaks forming a V-like shape. It was found that these chevrons originate from scattering off the sidewalls of the holes and not off the QDs. This can be verified by comparing the angle ϕ indicated in the image with the sidewall angle α_{sidewall}. The relation between the two is given by $\alpha_{\text{sidewall}} = 90 - \varphi$. The sidewall angles can be extracted from AFM images. They were found to be different for sidewalls parallel to $[0\,1\,1]$ and $[0\,\bar{1}\,1]$. The angles are approximately 15° and 10°, respectively. The angle of the chevron in (b) amounts to $\varphi \approx 73°$ so that the above relation is approximately fulfilled. Further confirmation of the origin of the chevrons can be obtained when rotating the sample by 90° around the surface normal so that the X-ray beam is incident along the $[0\,\bar{1}\,1]$ direction. A larger angle of $\varphi \approx 78°$ is measured for the chevron (not shown), which is in accordance with the lower sidewall angle of $\alpha_{\mathrm{sidewall}} = 10°$. The diffraction pattern in (b) was integrated along $[1\,0\,0]$ inside the white box and the resulting intensity profile is shown in the diagram of (d). The two side maxima corresponding to the intensity contribution from the chevron is clearly observed. Furthermore, the distance between the periodic maxima is given and corresponds to the hole spacing in real space. It can be calculated from $2\pi/d_{\mathrm{q}}$ and yields about 260 nm. The pattern in the polar GISAXS plot is thus the reciprocal version of the hole array. A QD signal could not be identified in GISAXS. The scattering volume of the hole is much larger than that of the QDs and since the ordering/alignment of the QDs is parallel to the preferential directions of the sidewalls of the holes, the QD signal is exceeded by scattering off the holes. The shape of the QDs possibly contributes to the shape of the area beyond which the intensity of the reciprocal pattern strongly decreases. A similar shape of the diffuse region was observed in GISAXS of self-assembled QDs in the study of *Riotte et al.* [30]. However, clear evidence is not given in this case as the convolution with the hole signal is too strong.

Since the information of the GISAXS signal were not satisfying GID measurements were tested in order to reveal the QD evolution during *in situ* annealing. The investigated sample was transferred to the synchrotron under UHV and heated up to the annealing temperature in the portable MBE system mounted on the diffractometer. The As background pressure was set to about 3×10^{-7} Torr. This is much lower (one order of magnitude) compared to the As BEP during growth in the stationary MBE system, but higher As fluxes were not possible with the portable system. The calibration of the substrate temperature was difficult since only a thermocouple at the substrate heater was available and no pyrometer. An annealing temperature of 500°C was aimed at, similar to the annealing experiment above. The sample was heated up from room temperature to a nominal temperature of 500°C and kept at this for 40 min. Thereafter, the substrate temperature was further increased to nominal 550°C at which the sample was kept for another 15 min before being cooled down to room temperature. The whole annealing process including temperature ramp up and ramp down took 230 min during which GID data were continuously recorded by measuring a small region in the vicinity of the GaAs $[0\,2\,2]$ *Bragg* peak. The *Bragg* angle for scattering off the $(0\,2\,2)$ planes is 13.803°.

Reciprocal space maps of the sample before *in situ* annealing, during annealing at 500°C and after annealing are shown in figure 6.14 (a), (b) and (c), respectively. The sample contained a hole array of 250 nm spacing which was rotated by 45° so that the major axes of the array point in the $\langle 0\,0\,1\rangle$ directions (see figure 6.12 (c)). Several features are observed in the map of (a). Sharp maxima with regular order appear in reciprocal space which are related to the periodic arrangement of scatterers on the substrate surface. The rotation of the array in real space is translated by exact the same rotation in reciprocal space. The pitch of the pattern in reciprocal space corresponds again to the spacing in real space. The border enclosing the peak array beyond which the intensity significantly drops is of hexagonal shape, as in GISAXS. By rotating the sample about 90° the hexagonal border rotates in the same way, which confirms it being a shape effect (either of QDs, but more likely of holes). The central maximum is related to the *Bragg* peak for the unstrained GaAs substrate and is found at the reciprocal vector $(Q_{\mathrm{x}}, Q_{\mathrm{y}}) = (0, 31.6)$. This roughly corresponds to the distance between $\{0\,2\,2\}$ planes in reciprocal space which is $d_{022} = 1.9987\,\mathrm{\mathring{A}}$. With respect to the GaAs lattice constant larger (smaller) Q_{y} values imply a compressively (tensile) strained lattice. Due to the formation of QDs the GaAs substrate exhibits different regions which are strained in one of the two ways. Since the

(a) Before annealing

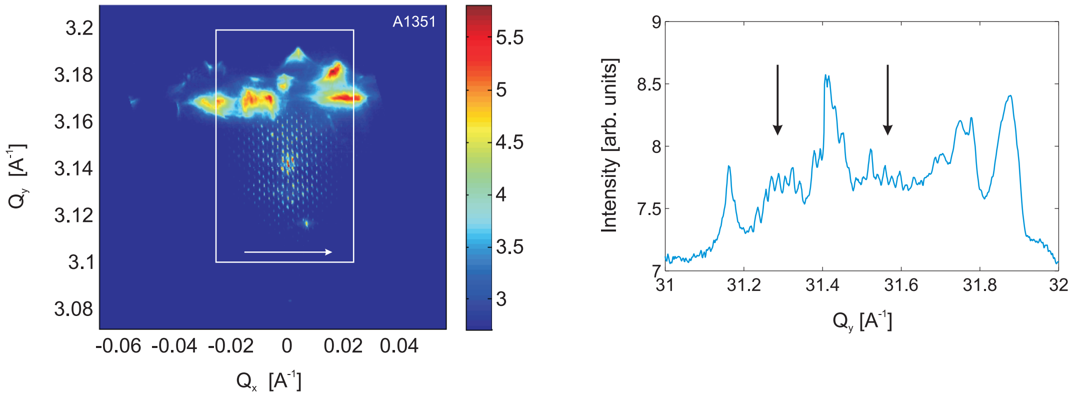

(b) During annealing at 500°C

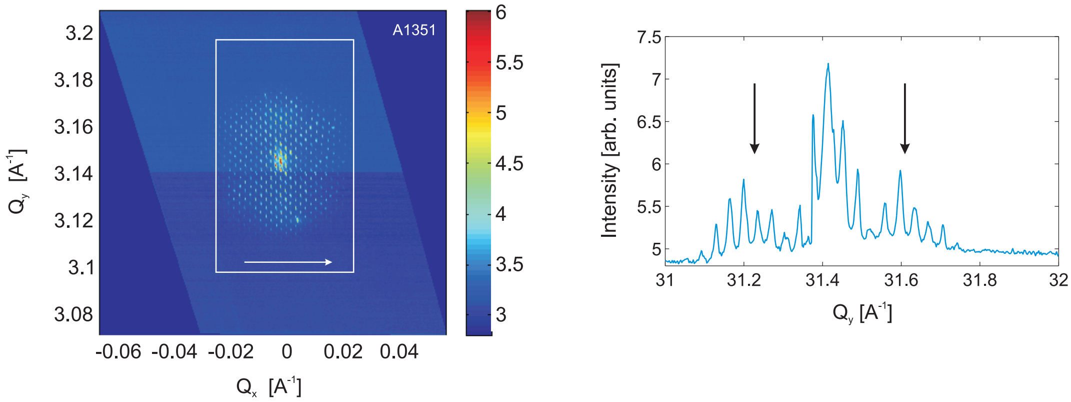

(c) After annealing

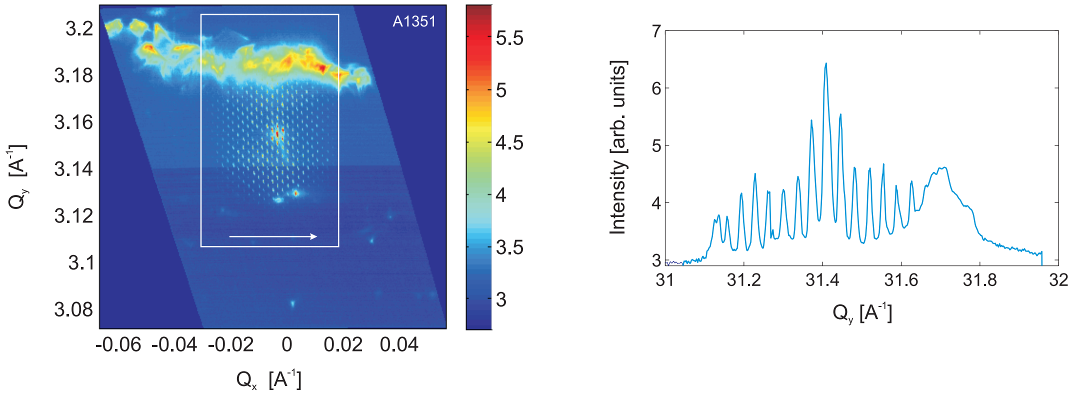

Figure 6.14 The evolution of the QD array was measured in GID geometry during *in situ* annealing. A reciprocal space map before the annealing process is shown in (a). The map in (b) was obtained during annealing at nominal 500°C and the one in (c) after annealing when the sample was cooled down. Intensity profiles were extracted from each GID map in order to better reveal the evolution. The signal in the white frame was integrated along the direction indicated by the arrow. The intensities in the GISAXS maps are given in log-scale.

QDs are coherently strained, a smooth transition of diffuse intensity should be observed in the reciprocal map between the InAs and the GaAs *Bragg* peaks. Such a feature is not seen. Diffuse maxima above and below the GaAs *Bragg* peak are observed (marked with black arrows in the intensity profile) but these are related to a shape effect, likely originating from varying hole sizes. This can be confirmed by rotating the sample. A specific alignment with the sample is observed as the diffuse intensity maxima rotate in the same way as the sample. If the diffuse intensity was related to strain it would not depend on the pattern orientation. A QD signal was hence also not observed in the GID pattern, which is a superposition of effects with different origin. The reciprocal space map is dominated by the sharp maxima resulting from the real space pattern while diffuse contributions originate from the individual shape of each hole. Again, the large volume of the holes compared to that of the QDs leads to dominant features in which a possible QD signal disappears. The broad structures of high intensity above the GaAs peak are due to diffraction off polycrystalline GaAs-Au alloys present on the surface surrounding the mesa and also on the mesa sidewalls. Since Au has a smaller lattice constant than GaAs, the possible alloys produce a signal above the GaAs peak. A large range of compositions is available and the exact configuration is not known.

The reciprocal space map in (b) shows one GID measurement during annealing at nominal 500°C. Compared to the GID pattern in (a) a few changes are observed. The most dominant is related to the broad signal above the GaAs peak which has disappeared. Considering the phase diagrams of different GaAs-Au alloys it is found that beyond a temperature of 460° the ternary solid solution of Au/GaAs forms a liquid phase of AuGa on top of solid GaAs [93]. This possibly explains the disappearance of the intensive signal. The regular pattern originating from the hole array in real space is visible and appears even larger than in (a). This is probably related to the missing strong intensity of the alloy which does not outshine the contributions of the hole array any longer. The diffuse intensity above and below the GaAs peak (marked with black arrows in the intensity profile) becomes even more pronounced compared to before the annealing step. The GID measurement depicted in (c) was obtained after the annealing procedure. The intensive diffraction off the alloys has reappeared, but the diffuse intensity has gone, as seen in the intensity profile. The sample shape of the holes has smoothed out during annealing, as was verified by AFM measurements (not shown). If the diffuse signal originates from sloped sidewalls, similarly to GISAXS, the smoothing destroys the distinct slope of the sidewall. Therefore, the diffuse signal has disappeared. The shift of the whole pattern towards higher Q_y values is not real and is due to the realignment procedure of the detector during the measurements. Although the temperature during annealing was expected to be around 500°C, AFM analysis of the sample after annealing reveals that a considerable number of QDs has survived the long annealing procedure. Comparing this fact to the *in situ* annealing investigations presented above it is concluded that the temperature must have been below 500°C. This is the reason why In desorption was not efficient enough to dissolve all QDs during such long annealing. The average QD occupation before annealing was 3.8 ± 0.8 QDs/hole with 60% of the holes being occupied with 4 QDs. After annealing, a considerable average QD occupation of 1.1 ± 0.9 QDs/hole is found, with about 50% of the holes being occupied with 1 QD. No QDs or 2 QDs were found in 25% of the holes, each. Again, the power of the annealing process to control the QD occupation was demonstrated. Despite the fact that the QD signal was not observed in the HRXRD measurements, information on the hole array could be obtained. The limits of this technique were reveald with respect to the investigation of the particular configuration of QDs nucleating inside holes.

6.5 Conclusion

The evolution of positioned QDs and their distribution during *in situ* annealing was investigated. Two different annealing regimes were observed. First, dot ripening occurs for short annealing times. Second, after further annealing In desorption and interdiffusion take over as driving forces for the QD evolution. For the given annealing times of 2:30 min (7:30 min) it was possible to increase (decrease) the average QD diameter and height by more than 30% (7%) and 70% (40%), respectively. At the same time the In content of the QDs is altered which might be useful to control the QD photoluminescence. Furthermore, it was demonstrated that the average QD occupation can be well controlled by array spacing and/or annealing time while the width of the QD occupation distribution constantly decreases during annealing. Bearing in mind that the investigated parameters might not be controlled independently it was shown that *in situ* annealing is a powerful post growth technique to control the structural properties of positioned QDs.

7 Summary and Outlook

The fabrication of positioned InAs quantum dots (QDs) and the control of their structural properties as well as their distribution were in the focus of this work.

Site-selective growth was successfully implemented to form QDs at pre-defined locations. Small holes on the GaAs substrate surface with diameters below 100 nm act as preferential nucleation sites. A reliable fabrication process for the holes using electron beam lithography was established at the beginning of this work and continuously optimized. Holes with diameters down to 30 nm could be reliably fabricated. Molecular beam epitaxy (MBE) was then employed to grow a thin GaAs buffer layer (BL) followed by InAs QDs on top of the pre-patterned GaAs substrates. The preferential nucleation of QDs inside the holes was demonstrated.

The whole sample fabrication process comprised many steps and, consequently, a large number of process parameters needed to be adjusted and optimized in order to achieve good site-selectivity. Two major aspects which largely influence the result of the QD growth were addressed. An efficient sample cleaning process prior to MBE growth was found to be essential in order to get rid of defect holes occurring in the thin GaAs BL. Transmission electron microscopy (TEM) investigations revealed the origin of the defect holes being at the regrowth interface. Additional atomic force microscopy (AFM) studies proved that traces of organic compounds from the resist remained on the GaAs substrate even after thorough cleaning with wet chemicals. A more efficient cleaning mechanism was required. As a consequence, a process based on the interaction of ultraviolet (UV) light and atomic oxygen with organic compounds was implemented. This cleaning concept was realized in a UV/ozone cleaner, which was designed, built and brought to operation. The cleaning performance was demonstrated and optimized. A reduction in root mean square (RMS) surface roughness from 0.390 nm for pre-cleaned samples to 0.255 nm for samples processed in the UV/ozone cleaner was achieved. This relates to a RMS roughness of about 0.180 nm for high quality GaAs films without further processing. Thus, very clean surfaces could be obtained. The efficient removal of residual organic contamination was proven in subsequent BL overgrowth where no defect holes were observed any more.

The removal of the surface oxide right before BL growth is another critical step which determines the success of site-selective growth. It was shown that conventional thermal deoxidation at 580°C leads to the formation of small pits on the surface which interfere with the attempt to position QDs in a deterministic way. A low temperature deoxidation process was required. A surface sensitive deoxidation process was implemented at 480°C which is based on the deposition of pure Ga. The superior performance of Ga-assisted deoxidation was demonstrated. While thermal deoxidation led to a RMS surface roughness of 0.320 nm, this could be improved to 0.185 nm by Ga-assisted deoxidation. The improved cleaning procedure and the surface sensitive deoxidation allowed for the fabrication of perfectly ordered QD arrays, where QD nucleation at un-defined sites was drastically reduced.

General structural features of positioned QDs were investigated. QDs selectively formed in holes were analyzed by high resolution TEM (HRTEM) for the first time. Preferential nucleation sites were found at the center of the hole and on the sidewalls. This is in agreement with the theory introduced to describe the site-selective growth. The shape of the QDs was discovered to be dome-like. It could be shown that the positioned QDs were coherently strained and contained essentially no lattice defects.

The optical quality of positioned QDs was studied in photoluminescence (PL) experiments. The PL spectra obtained from dense QD arrays were correlated with QD densities extracted from AFM measurements on uncapped samples. PL emission from positioned QDs was confirmed but the quantum efficiency was only 30% of that for random self-assembled QDs.

In order to control the structural properties of positioned QDs, the influence of the hole parameters, the pattern parameters and the growth parameters on the QD formation was investigated. It was confirmed that the average QD occupation increases with larger lateral hole sizes. The hole spacing has an influence on the material distribution and more QDs were found per hole for larger spacings. This was related to the individual reservoir of In adatoms for each hole which becomes larger on sparser arrays. The thickness of the GaAs BL, which is deposited on the pre-patterned surface, was varied. The average QD occupation could be decreased by increasing the BL thickness. The QD size was not significantly influenced by the BL thickness. However, the QD height could be decreased by reducing the amount of deposited InAs. Furthermore, lower InAs amounts led to more uniform QD occupations. The arrangement of the holes was also found to influence the QD occupation. Hexagonal hole arrays produced slightly higher QD occupations than square arrays. The increase could be related to a difference in the distance between neighboring holes in major crystal directions on the hexagonal array. Altogether, average QD occupations between 1-6 QDs/hole could be obtained by adjusting these parameters. However, the distribution of QD occupations was rather broad. Therefore, a dry etching technique based on reactive ion etching with an inductively coupled plasma was used to increase the anisotropy of the hole profile. This allowed for an increase in hole depth while maintaining small lateral hole sizes. In this way, it was possible to study the influence of the hole profile and the hole depth on the site-selective QD formation. It was observed that the average QD occupation decreases for deeper holes. The uniformity is improved at the same time. Finally, it was possible to fabricate samples with deep holes where 80% of the holes were occupied with only one QD.

A different approach to control the distribution and the size of QDs for given patterns and growth conditions was studied. The potential of annealing processes to manipulate the properties of site-selective QDs was demonstrated for the first time. *In situ* annealing experiments were carried out in the MBE chamber after QD growth. A redistribtuion of the deposited material was observed. It was found that site-selective QDs are more stable than random self-assembled QDs. A reduction of QDs nucleating between defined sites could be achieved while maintaining full occupation of the defined sites. This observation opens up new possibilities in QD array designs. Unintended QD nucleation can be eliminated by applying an adequate annealing recipe.

Furthermore, the size of the QDs could varied in both directions. An increase in size is observed for short annealing times while a decrease in size is obtained after long annealing. The average QD occupation continuously decreased with annealing time. It was possible to reduce the average QD occupation from 5 QDs/hole to one QD/hole. This was accompanied by an improvement in uniformity of the QD occupation. The shape of the QDs influences the electronic properties and is therefore of interest with respect to applications. The positioned QDs were found to be elongated in the $[0\,\bar{1}\,1]$ direction. This asymmetry is slightly reduced during annealing.

Finally, high resolution X-ray diffraction (HRXRD) measurements of ordered QD arrays did not resolve the QD signal. The limits of the particular geometries used in HRXRD measurements with respect to positioned QDs in holes were found and new measurement strategies have to be developed as a consequence.

Outlook

This thesis was focused on various aspects of the fabrication of site-selective QDs. The promising results of this work have yet to be expanded by optical measurements. While most works in the field of site-selective QD growth have concentrated on the development of particular structures with single QDs for future applications, different ways to control QD occupations and QD sizes were described in this thesis. The influence of various hole and growth parameters on these properties have been demonstrated. The observed trends allow for a better adjustment of a particular QD configuration to the needs of a possible application. After this rather general investigation of influential parameters, more detailed studies will be required in the future to increase the control on a larger scale. Extensive annealing studies with different initial amounts of deposited InAs will be useful to investigate possible impacts of the material redistribution on electronic and optical properties. Using dry etching to fabricate deeper holes might have the potential to grow thicker GaAs BL before the QD growth. The electronic and optical properties of the QDs would probably benefit from an increased distance to the regrowth interface, which is always a possible source of defects.

A General fabrication steps and parameters

The first part of the appendix lists the steps of the different processes used for the sample fabrication in this work including the relevant parameters.

A.1 Molecular beam epitaxial growth of GaAs buffer layer (BL)

- Bake out in loading chamber

  60 min at 130°C

- Thermal deoxidation in growth chamber

  20 min at 580°C
  $\mathrm{BEP_{As}} = 6 \times 10^{-6}$ Torr

- 300 nm GaAs BL, 580°C

  $\mathrm{BEP_{Ga}} = 3 \times 10^{-7}$ Torr
  $\mathrm{BEP_{As}} = 6 \times 10^{-6}$ Torr

- *In situ* annealing

  10 min at 590°C
  $\mathrm{BEP_{As}} = 6 \times 10^{-6}$ Torr

A.2 Substrate patterning by electron beam lithography

Spin coating (AR-P 617.03)

- 3 s at 300 RPM
- 90 s at 5000 RPM
- Baking resist covered sample in convection oven

  60 min at 200°C

Electron beam exposure (Raith ElphyPlus connected to Zeiss SUPRA 55VP)

- See sample list for parameters

Development (AR 600-56)

- 1 min at RT
- Stop in isopropyl alcohol (IPA) bath
- Blow dry with nitrogen

The samples were etched by wet chemical etching or dry etching (Oxford Plasmalab System ICP 180-100).

Wet chemical etching

- 30 s in 1:8:800 H_2SO_4:H_2O_2:H_2O at RT (etch rate $\tilde{1}$ nm/s)
- Stop in H_2O bath
- Blow dry with nitrogen

Dry etching

- Hard baking of resist in convection oven

  30 min at 130°C
- $SiCl_4$:Ar plasma (see sample list for parameters)

Resist removal

- 20 min in remover (AR 600-70) at 70°C
- Rinse in IPA bath
- Blow dry with nitrogen
- 5 min in remover (AR 300-47) at 70°C
- Rinse in H_2O bath
- Blow dry with nitrogen
- 5 min in TCE bath (later NMP bath) at 70°C
- Blow dry with nitrogen
- 2 min in acetone in ultrasonic (US) bath at RT
- 2 min in IPA in US bath at RT
- 2 min in methanol in US bath at RT
- Blow dry with nitrogen

The samples were cleaned using the UV/ozone process or plasma ashing (Diener Electronic Nano).

UV/ozone cleaning

- 10 min O_2 (0.8 l/min) supply at RT without UV illumination
- Ozone generating UV illumination at 100°C with O_2 (0.4 l/min) supply (see sample list for cleaning time)
- 10 min (0.8 l/min) supply at RT with ozone destroying UV illumination

Oxygen plasma ashing

- O_2 plasma with 150 W, 15 sccm O_2 (see sample list for cleaning time)

Native oxide removal

- Dip in 1:3 HCl:H_2O bath
- Rinse in H_2O bath
- Blow dry with nitrogen
- Load into MBE system within 30 min

A.3 Molecular beam epitaxial growth of site-selective quantum dots (QDs)

- Bake out in loading chamber

  60 min at 130°C

- Ga-assisted deoxidation in growth chamber

  8× 30 s Ga (1 ML/min) and 30 s pause at 480°C
  $\mathrm{BEP_{Ga}} = X \times 10^{-8}$ Torr

- GaAs BL, 500°C

  $\mathrm{BEP_{Ga}} = 3 \times 10^{-7}$ Torr
  $\mathrm{BEP_{As}} = 6 \times 10^{-6}$ Torr

- InAs QDs, 500°C

  $\mathrm{BEP_{In}} = 2 \times 10^{-8}$ Torr
  $\mathrm{BEP_{As}} = 3 \times 10^{-6}$ Torr

- *In situ* annealing, 500°C

  $\mathrm{BEP_{As}} = 6 \times 10^{-6}$ Torr

B Fabrication steps for mesa samples

B.1 1st lithography for mesa structure

Spin coating (AR-N 7720)

- 2 s at 400 RPM
- 70 s at 3000 RPM
- Baking resist covered sample on hotplate

  70 min at 85°C

Electron beam exposure (Raith ElphyPlus connected to Zeiss SUPRA 55VP)

- $U = 20\,\mathrm{kV}$
- $d_{\mathrm{ap}} = 120\,\mu\mathrm{m}$
- $I = 4.6\,\mathrm{nA}$
- $D_{\mathrm{area}} = 40\,\mu\mathrm{C/cm}^2$

Development

- Bake out for cross linking reaction

  135 s at 110°C on hotplate
- 135 s in 3:1 AR 300-47:H_2O at RT
- Stop in H_2O bath
- Blow dry with nitrogen

Wet chemical etching

- 30 s in 1:80:800 H_2SO_4:H_2O_2:H_2O at RT (etch rate $\tilde{2}0\,\mathrm{nm/s}$)
- Stop in H_2O bath
- Blow dry with nitrogen

Resist removal

- 20 min in acetone at 70°C
- 2 min in acetone in US bath at RT
- Blow dry with nitrogen
- 5 min in remover (AR 300-47) at 70°C
- Rinse in H_2O bath
- Blow dry with nitrogen
- 5 min in NMP bath at 70°C
- Blow dry with nitrogen
- 2 min in IPA in US bath at RT
- Blow dry with nitrogen

B.2 2nd lithography for lift-off process

Spin coating (AR-N 7720)

- 2 s at 400 RPM
- 70 s at 3000 RPM
- Baking resist covered sample on hotplate

  70 min at 85°C

Electron beam exposure (Raith ElphyPlus connected to Zeiss SUPRA 55VP)

- $U = 20\,\mathrm{kV}$
- $d_{\mathrm{ap}} = 120\,\mathrm{\mu m}$
- $I = 4.6\,\mathrm{nA}$
- $D_{\mathrm{area}} = 40\,\mathrm{\mu C/cm^2}$

Development

- Bake out for cross linking reaction

  135 s at 110°C on hotplate
- 135 s in 3:1 AR 300-47:H_2O at RT
- Stop in H_2O bath
- Blow dry with nitrogen

Au layer deposition

- 60 nm Au in thermal evaporator

Resist removal

- 20 min in acetone at 70°C
- 2 min in acetone in US bath at RT
- Rinse with IPA from wash bottle
- Blow dry with nitrogen
- 5 min in NMP bath at 70°C
- Blow dry with nitrogen
- 2 min in acetone in US bath at RT
- 2 min in IPA in US bath at RT
- 2 min in methanol in US bath at RT
- Blow dry with nitrogen

Oxygen plasma ashing

- 20 min O_2 plasma with 150 W, 15 sccm O_2

B.3 3^{rd} lithography for hole pattern

Spin coating (AR-P 617.03)

- 3 s at 300 RPM
- 90 s at 5000 RPM
- Baking resist covered sample on hotplate
  10 min at 210°C

Electron beam exposure (Raith ElphyPlus connected to Zeiss SUPRA 55VP)

- $U = 30\,\mathrm{kV}$
- $d_{\mathrm{ap}} = 7.5\,\mu\mathrm{m}$
- $I = 16.8\,\mathrm{pA}$
- $D_{\mathrm{dot}} = 0.002\,\mathrm{pC}$

Development (AR 600-56)

- 1 min at RT
- Stop in IPA bath
- Blow dry with nitrogen

Wet chemical etching

- 30 s in 1:8:800 H_2SO_4:H_2O_2:H_2O at RT (etch rate $\tilde{1}$ nm/s)
- Stop in H_2O bath
- Blow dry with nitrogen

Resist removal

- 20 min in remover (AR 600-70) at 70°C
- Rinse in IPA bath
- Blow dry with nitrogen
- 5 min in NMP bath at 70°C
- Blow dry with nitrogen
- 2 min in acetone in US bath at RT
- 2 min in IPA in US bath at RT
- 2 min in methanol in US bath at RT
- Blow dry with nitrogen

Oxygen plasma ashing

- 20 min O_2 plasma with 150 W, 15 sccm O_2
- 2 min in acetone in US bath at RT
- 2 min in IPA in US bath at RT
- 2 min in methanol in US bath at RT
- Blow dry with nitrogen
- 5 min O_2 plasma with 270 W, 15 sccm O_2

Native oxide removal

- Dip in 1:3 HCl:H_2O bath
- Rinse in H_2O bath
- Blow dry with nitrogen
- Load into MBE system within 30 min

B.4 Molecular beam epitaxial growth of site-selective QDs

- Bake out in loading chamber

  60 min at 130°C

- Ga-assisted deoxidation in growth chamber

  8× 30 s Ga (1 ML/min) and 30 s pause at 480°C
  $\mathrm{BEP}_{\mathrm{Ga}} = X \times 10^{-8}$ Torr

- 2 min *in situ* annealing, 580°C

  $\mathrm{BEP}_{\mathrm{As}} = 6 \times 10^{-6}$ Torr

- 20 nm GaAs BL, 500°C

  $\mathrm{BEP}_{\mathrm{Ga}} = 3 \times 10^{-7}$ Torr
  $\mathrm{BEP}_{\mathrm{As}} = 6 \times 10^{-6}$ Torr

- 1.8 ML InAs QDs, 500°C

  $\mathrm{BEP}_{\mathrm{In}} = 2 \times 10^{-8}$ Torr
  $\mathrm{BEP}_{\mathrm{As}} = 3 \times 10^{-6}$ Torr

C List of samples

The third part of the appendix lists the samples presented in this thesis with their respective process parameters.

Sample	**Electron beam exposure**					**Wet chemical etching**	
	U [kV]	d_{ap} [µm]	I [pA]	D_{dot} [pC]	D_{area} [µm/cm^2]	t [s]	H_2SO_4:H_2O_2:H_2O
E10	20	10	31.0		150	300	1:80:800
E13	20	10	30.9	0.006		100	1:8:800
E20	20	7.5	15.7	0.006			
PSI3	100	n.a.	n.a.	n.a.		30	1:8:800

Table C.1 List of samples presented in this work which were used for WCE calibration. The corresponding parameters used in lithography and WCE are given.

Sample	**Electron beam exposure**				**Dry etching**					
	U [kV]	d_{ap} [µm]	I [pA]	D_{dot} [pC]	t [s]	$SiCl_4$:Ar [sccm:sccm]	ICP [W]	RF [W]	P [mbar]	T [°C]
A1319-1	30	7.5	15.6	0.002	15	2:4	350	30	2	10
A1319-2	30	7.5	15.6	0.001	15	2:4	150	20	2	10
A1423-1	30	7.5	15.6	0.0015	10	2:4	150	20	2	10
A1423-2	30	7.5	15.6	0.004	10	2:4	150	20	2	10
A1425-1	30	7.5	15.8	0.0015	20	2:4	150	20	2	10
A1425-2	30	7.5	15.8	0.004	20	2:4	150	20	2	10

Table C.2 List of samples presented in this work which were dry etched. The corresponding parameters used in lithography and ICP-RIE are given.

Sample	**Electron beam exposure**				**UV/ozone cleaning**		
	U [kV]	d_{ap} [µm]	I [pA]	D_{dot} [pC]	t [s]	O_2 [l/min]	T [°C]
A1406-1	30	7.5	15.6	0.001	0	0.4	100
A1406-2	30	7.5	15.6	0.001	30	0.4	100
A1406-3	30	7.5	15.6	0.001	60	0.4	100
A1406-4	30	7.5	15.6	0.001	600	0.4	100

Table C.3 List of samples presented in this work which were used for the optimization of the UV/ozone cleaning process. The corresponding parameters used in lithography and UV/ozone cleaning are given.

Sample	Electron beam exposure				Etching		Cleaning		MBE					
	U [kV]	d_{ap} [µm]	I [pA]	D_{dot} [pC]	WCE [s]	DE [s]	UV/O$_3$ [min]	PA [min]	TD	GaD	GaAs BL [nm]	InAs QDs [ML]	Annealing [min]	GaAs CL [nm]
A1053	20	10	30.5	0.002	30					x	16	1.70		
A1083	20	10	30.8	0.005	30					x	16	1.77		
A1085	20	10	30.7	0.005	30					x	16	1.77	2:30	
A1089	20	10	30.6	0.005	30					x	16	1.77		90
A1130	20	10	30.6	0.005	30		1			x	16	2.60	7:30	
A1170-1	20	10	30.6	0.002	30		1			x	20	1.50		
A1170-2	20	10	30.6	0.005	30		1			x	20	1.50		
A1218									x		16	1.90		
A1286									x		300			
A1288									x					
A1291										x				
A1323	30	7.5	15.6	0.002	45									
A1341	30	7.5	15.7	0.002	30			25		x	20	1.84		
A1351	30	7.5	15.5	0.002	30			25		x	20	1.84		
A1368-1	30	7.5	15.8	0.0005	30			25		x	15	1.60		
A1368-2	30	7.5	15.8	0.002	30			25		x	15	1.60		
A1369	30	7.5	15.5	0.002	30			25		x	5	1.60		
A1373	30	7.5	15.6	0.002	30			25		x	35	1.60		
A1408	100	n.a.	n.a.	n.a.	30			25		x	20	1.63		
A1409	100	n.a.	n.a.	n.a.	30			25		x	20	1.63	2:30	
A1410	100	n.a.	n.a.	n.a.	30			25		x	20	1.63	7:30	
A1423-1	30	7.5	15.6	0.0015		10		25		x	12	1.63		
A1423-2	30	7.5	15.6	0.004		10		25		x	12	1.63		
A1425-1	30	7.5	15.8	0.0015		20		25		x	12	1.63		
A1425-2	30	7.5	15.8	0.004		20		25		x	12	1.63		

Table C.4 List of MBE samples presented in this work. The corresponding parameters used in lithography and MBE growth are given.

List of Figures

List of Tables

Bibliography

[1] G. E. Moore. Cramming more components onto integrated circuits. *Electronics*, 38(8), 1965.

[2] O. G. Schmidt. *Lateral Alignment of Epitaxial Quantum Dots.* Springer, 2007.

[3] M. A. Herman and H. Sitter. *Molecular Beam Epitaxy.* Springer, 1996.

[4] L. Jacak, P. Hawrylak, and A. Wójs. *Quantum Dots.* Springer, 1998.

[5] J.-L. Pautrat, J.-M. Gérard, É. Bustarret, D. Cassagne, E. Hadji, and C. Seassal. *Nanoscience.* Springer, 2007.

[6] K. Nishi. *Semiconductor Quantum Dots.* Springer, 2002.

[7] S. Kiravittaya, A. Rastelli, and O. G. Schmidt. Advanced quantum dot configurations. *Rep. Prog. Phys.*, 72:046502, 2009.

[8] M. Sugawara, editor. *Semiconductors and Semimetals.* London: Academic, 1999.

[9] J. Sabarinathan, P. Bhattacharya, P.-C. Yu, S. Krishna, J. Cheng, and D. G. Steel. An electrically injected InAs/GaAs quantum-dot photonic crystal microcavity light-emitting diode. *Appl. Phys. Lett.*, 81:3876–, 2002.

[10] D. L. Huffaker, G. Park, Z. Zou, o. B. Shchekin, and D. G. Deppe. 1.3 µm room-temperature GaAs-based quantum-dot laser. *Appl. Phys. Lett.*, 73:2564–, 1998.

[11] A. Marent, T. Nowozin, M. Geller, and D. Bimberg. The QD-Flash: a quantum dot-based memory device. *Semicond. Sci. Technol.*, 26:014026, 2011.

[12] P. Michler, A. Kiraz, C. Becher, W. V. Schoenfeld, P. M. Petroff, L. Zhang, E. Hu, and A. Imamoğlu. A Quantum Dot Single-Photon Turnstile Device. *Science*, 290:2282–2285, 2000.

[13] N. Akopian, N. H. Lindner, E. Poem, Y. Berlatzky, J. Avron, D. Gershoni, B. D. Gérardot, and P. M. Petroff. Entangled Photon Pairs from Semiconductor Quantum Dots. *Phys. Rev. Lett.*, 96:130501–130504, 2006.

[14] M. Karl, S. Li, T. Passow, W. Löffler, H. Kalt, and M. Hetterich. Localized and delocalized modes in coupled optical micropillar cavities. *Opt. Express*, 15(13):8191–8196, 2007.

[15] T. Yoshie, A. Scherer, J. Hendrickson, G. Khitrova, H. M. Gibbs, G. Rupper, C. Ell, O. B. Shchekin, and D. G. Deppe. Vacuum Rabi splitting with a single quantum dot in a photonic crystal nanocavity. *Nature*, 432:200–203, 2004.

[16] J. P. Reithmaier, G. Sek, A. Löffler, C. Hofmann, S. Kuhn, S. Reitzenstein, L. V. Keldysh, V. D. Kulakovskii, T. L. Reinecke, and A. Forchel. Strong coupling in a single quantum dot-semiconductor microcavity system. *Nature*, 432:197–, 2004.

[17] A. Badolato, K. Hennessy, M. Atatüre, J. Dreiser, E. Hu, P. M. Petroff, and A. Imamoğlu. Deterministic Coupling of Single Quantum Dots to Single Nanocavity Modes. *Science*, 308:1158–, 2005.

[18] E. Peter, P. Senellart, D. Martrou, , A. Lemaitre, J. Hours, J. M. Gérard, and J. Bloch. Exciton-Photon Strong-Coupling Regime for a Single Quantum Dot Embedded in a Microcavity. *Phys. Rev. Lett.*, 95:067401, 2005.

[19] C. Böckler, S. Reitzenstein, C. Kistner, R. Debusmann, A. Löffler, T. Kida, Höfling S., A. Forchel, L. Grenouillet, J. Claudon, and J. M. Gérard. Electrically driven high-Q quantum dot-micropillar cavities. *Appl. Phys. Lett.*, 92:091107, 2008.

[20] D. Hu. *Stress evolution during growth of InAs on GaAs measured by an in-situ cantilever beam setup.* PhD thesis, Humboldt-Universität zu Berlin, 2007.

[21] C. Teichert, J. C. Bean, and M. G. Lagally. Self-organized nanostructures in $\mathrm{Si}_{1-x}\mathrm{Ge}_x$ films on Si(001). *Appl. Phys. A*, 67:675–685, 1998.

[22] S. Jeppesen, S. Miller, S. Hessman, B. Kowalski, I. Maximov, and L. Samuelson. Assembling strained InAs islands on patterned GaAs substrates with chemical beam epitaxy. *Appl. Phys. Lett.*, 68:2228–2230, 1996.

[23] P. Atkinson, M. B. Ward, S. P. Bremner, D. Anderson, T. Farrow, G. A. C. Jones, A. J. Shields, and D. A. Ritchie. Site control of InAs quantum dot nucleation by *ex situ* electron-beam lithographic patterning of GaAs substrates. *Physica E*, 32:21–24, 2006.

[24] R. V. Kukta and D. Kouris. On the mechanisms of epitaxial island alignment on patterned substrates. *J. Appl. Phys.*, 97:033527, 2005.

[25] P. Atkinson, M. B. Ward, S. P. Bremner, D. Anderson, T. Farrow, G. A. C. Jones, A. J. Shields, and D. A. Ritchie. Site-Control of InAs Quantum Dots using *Ex-Situ* Electron-Beam Lithographic Patterning of GaAs Substrates. *Jpn. J. Appl. Phys.*, 45:2519–2521, 2006.

[26] H. Lee, R. R. Lowe-Webb, W. Yang, and P. C. Sercel. Formation of InAs/GaAs quantum dots by molecular beam epitaxy: Reversibility of the islanding transition. *Applied Physics Letters*, 71(16):2325–2327, 1997.

[27] C. Heyn. Stability of InAs quantum dots. *Physical Review B*, 66:075307, 2002.

[28] E. Placidi, A. D. Pia, and F. Arciprete. Annealing effects on faceting of InAs/GaAS(001) quantum dots. *Appl. Phys. Lett.*, 94:021901, 2009.

[29] D. Z. Hu, A. Trampert, and D. M. Schaadt. Morphology and stress evolution of InAs QD grown and annealed *in-situ* at high temperature. *J. Cryst. Growth*, 312:447–451, 2010.

[30] M. Riotte, E. Fohtung, D. Grigoriev, A. A. Minkevich, T. Slobodskyy, M. Schmidbauer, T. H. Metzger, D. Z. Hu, D. M. Schaadt, and T. Baumbach. Lateral ordering, strain, and morphology evolution of InGaAs/GaAs(001) quantum dots due to high temperature postgrowth annealing. *Appl. Phys. Lett.*, 96:083102, 2010.

[31] D. J. Griffiths. *Introduction to Quantum Mechanics.* Prentice Hall, 2004.

[32] J. P. Reithmaier, editor. *Nanostructured Materials for Advanced Technological Applications.* Springer, 2009.

[33] IOFFE Physico-Technical Institute. New Semiconductor Materials. Characteristics and Properties. www.ioffe.ru, 2009.

[34] S. Ghosh, B. Kochman, J. Singh, and P. Bhattacharya. Conduction band offset in InAs/GaAs self-organized quantum dots measured by deep level transient spectroscopy. *Appl. Phys. Lett.*, 76:2571, 2000.

[35] N. Moll, A. Kley, E. Pehlke, and M. Scheffler. GaAs equilibrium crystal shape from first principles. *Phys. Rev. B*, 54(12):8844–8855, 1996.

[36] E. Pehlke, N. Moll, and M. Scheffler. The Equilibrium Shape of Quantum Dots. *arXiv:cond-mat/9612004v1*, [cond-mat.mtrl-sci], 1996.

[37] F. Adler, M. Geiger, A. Bauknecht, F. Scholz, and H. Schweizer. Intrinsic Carrier Relaxation and the Exciton Lifetime in InAs/GaAs Quantum Dots. *Phys. Statuts Solidi A*, 164(1):431–436, 1997.

[38] L. Vegard. Die Konstitution der Mischkristalle und die Raumfüllung der Atome. *Zeitschrift für Physik*, 5(17), 1921.

[39] M. Helfrich. Site-selective Molecular Beam Epitaxial Growth of InAs Quantum Dots on pre-patterned GaAs Substrates. Diploma thesis, 2009.

[40] J. Tersoff, C. Teichert, and M. G. Lagally. Self-Organization in Growth of Quantum Dot Superlattices. *Phys. Rev. Lett.*, 76(10):1675–1678, 1996.

[41] C. Teichert, M. G. Lagally, L. J. Peticolas, J. C. Bean, and J. Tersoff. Stress-induced self-organization of nanoscale structures in SiGe/Si multilayer films. *Phys. Rev. B*, 53(24):16334–16337, 1996.

[42] N. Gogneau, L. Le Gratiet, E. Cambril, G. Beaudoin, G. Patriarche, A. Beveratos, R. Hostein, I. Robert-Philip, J. Y. Marzin, and I. Sagnes. One-step nano-selective area growth (nano-SAG) of localized InAs/InP quantum dots: First step towards single-photon source applications. *J. Cryst. Growth*, 310:3413–3415, 2008.

[43] N. L. Dias, A. Garg, U. Reddy, J. D. Young, V. B. Verma, R. P. Mirin, and J. J. Coleman. Directed self-assembly of InAs quantum dots on nano-oxide templates. *Appl. Phys. Lett.*, 98:141112, 2011.

[44] S. Ohkouchi, Y. Nakamura, H. Nakamura, and K. Asakawa. Nano-probe-assisted technology of indium-nano-dot formation for site-controlled InAs/GaAs quantum dots. *Physica E*, 21:597–600, 2004.

[45] S. Ohkouchi, Y. Nakamura, H. Nakamura, and K. Asakawa. Indium nano-dot arrays formed by field-induced deposition with a Nano-Jet Probe for site-controlled InAs/GaAs quantum dots. *Thin Solid Films*, 464-465:233–236, 2004.

[46] S. Ohkouchi, Y. Sugimoto, N. Ozaki, H. Ishikawa, and K. Asakawa. Molecular beam epitaxial growth of site-controlled InAs quantum dot arrays using templates fabricated by the Nano-Jet Probe method. *Physica E*, 40:1794–1796, 2008.

[47] A. Urbańczyk, G. J. Hamhuis, and R. Nötzel. In islands and their conversion to InAs quantum dots on GaAs (100): Structural and optical properties. *J. Appl. Phys.*, 107:014312, 2010.

[48] H. Heidemeyer. *Konzepte zur gezielten lateralen Positionierung selbstordnender InAs Quantenpunkte.* PhD thesis, Max-Planck-Institut für Festkörperforschung, 2004.

[49] D. J. Srolovitz. On the stability of surfaces of stressed solids. *Acta metall.*, 37(2):621–625, 1989.

[50] H. Wang, Y. Zhang, and F. Liu. Enhanced growth instability of strained film on wavy substrate. *J. Appl. Phys.*, 104:054301, 2008.

[51] B. Yang, F. Liu, and M. G. Lagally. Local Strain-Mediated Chemical Potential Control of Quantum Dot Self-Organization in Heteroepitaxy. *Phys. Rev. Lett.*, 92(2):025502, 2004.

[52] D. Mailly and C. Vieu. *Nanoscience.* Springer, 2007.

[53] K. Norrman, A. Ghanbari-Siahkali, and N. B. Larsen. Studies of spin-coated polymer films. *Annual Reports on the Progress of Chemistry, Section C: Physical Chemistry*, 101:174 – 201, 2005.

[54] H. Hiraoka. Radiation Chemistry of Poly(methacrylates). *IBM Journal of Research and Development*, 21, 1977.

[55] C. Mayer. Optimization of site selective Quantum Dots. Diploma thesis, 2012.

[56] R. et al. Gauvin. CASINO - monte CArlo SImulation of electroN trajectory in sOlids. www.gel.usherbrooke.ca/casino, 2009.

[57] A. G. Baca and C. I. H. Ashby. *Fabrication of GaAs Devices.* Peter Peregrinus Ltd, 2005.

[58] S. Schneider and S. McClatchie. *Material Removing Techniques - Etching and Chemical Mechanical Polishing (Nanoelectronics and Information Technology).* Wiley-VCH, 2003.

[59] J. Hutchings. Presentation on the properties of the ICP180, 2011.

[60] E. C. Larkins and J. S. Harris Jr. *Molecular Beam Epitaxy. Applications to Key Materials.* Noyes Publications, 1995.

[61] A. Ichimiya and P. I. Cohen. *Reflection High Energy Electron Diffraction.* Cambridge University Press, 2004.

[62] K. A. Jackson. *Kinetic Processes.* WILEY-VCH, 2004.

[63] A. Madhukar. Far from equilibrium vapour phase growth of lattice matched III-V compound semiconductor interfaces: Some basic concepts and monte-carlo computer simulations. *Surface Science*, 132(1-3):344–374, 1983.

[64] J. A. Venables. Atomic processes in crystal growth. *Surface Science*, 299-300:798–817, 1994.

[65] H. J. Scheel. *Crystal Growth Technology.* John Wiley & Sons Ltd., 2004.

[66] K. Alavi. *Handbook of Compound Semiconductors. Growth, Processing, Characterization, and Devices.* Noyes Publications, 1995.

[67] J. R. Vig. *Handbook of Semicondutor Wafer Cleaning Technology. Science, Technology, and Applications.* Noyes Publications, 1993.

[68] D. A. Bolon and C. O. Kunz. Ultraviolet depolymerization of photoresist polymers. *Polym. Eng. Sci.*, 12(2):109–111, 1972.

[69] J. R. Vig. UV/Ozone Cleaning of Surfaces. *IEEE Transactions on Parts, Hybrids, and Packaging*, PHP-12(4):365–370, 1976.

[70] J. R. Vig. *Treatise on Clean Surface Technology.* Plenum, NY, 1987.

[71] Y. Asaoka. Desorption process of GaAs surface native oxide controlled by direct Ga-beam irradiation. *J. Cryst. Growth*, 251:40–45, 2003.

[72] P. Atkinson, O. G. Schmidt, S. P. Bremner, and D. A. Ritchie. Formation and ordering of epitaxial quantum dots. *C. R. Phys.*, 9(8):788–803, 2008.

[73] F. Lukes. Oxidation of Si and GaAs in air at room temperature. *Surf. Sc.*, 30:91, 1972.

[74] P. Atkinson, S. Kiravittaya, M. Benyoucef, A. Rastelli, and O. G. Schmidt. Site-controlled growth and luminescence of InAs quantum dots using *in situ* Ga-assisted deoxidation of patterned substrates. *Appl. Phys. Lett.*, 93:101908, 2008.

[75] J. H. Lee, Zh. M. Wang, and G. J. Salamo. Survival of atomic monolayer steps during oxide desorption on GaAs (100). *J. Appl. Phys.*, 100:114330–114333, 2006.

[76] W. S. Rasband. ImageJ. http://imagej.nih.gov/ij/, 1997-2012.

[77] T. Passow, S. Li, P. Feinäugle, T. Vallaitis, J. Leuthold, D. Litvinov, D. Gerthsen, and M. Hetterich. Systematic investigation into the influence of growth conditions on InAs/GaAs quantum dot properties. *J. Appl. Phys.*, 102:073511, 2007.

[78] N. Y. Jin-Phillipp and F. Phillipp. Defect formation in self-assembling quantum dots of InGaAs on GaAs: a case study of direct measurements of local strain from HREM. *J. Microsc.*, 194(1):161–170, 1999.

[79] T. H. Metzger, I. Kegel, R. Paniago, and J. Peisl. Grazing incidence x-ray scattering: an ideal tool to study the structure of quantum dots. *J. Phys. D: Appl. Phys.*, 32(A):202, 1999.

[80] D. M. Bruls, J. W. A. M. Vugs, P. M. Koenraad, H. W. M. Salemnik, M. Wolter, M. Hopkinson, M. S. Skolnik, F. Long, and S. P. A. Gill. Determination of the shape and indium distribution of low-growth-rate InAs quantum dots by cross-sectional scanning tunneling microscopy. *Appl. Phys. Lett.*, 81:1708, 2002.

[81] Y. Chen and J. Washburn. Structural Transition in Large-Lattice-Mismatch Heteroepitaxy. *Phys. Rev. Lett.*, 77:4046–4049, 1996.

[82] C. Schneider, A. Huggenberger, T. Sünner, T. Heindel, M. Strauß, S. Göpfert, P. Weinmann, S. Reitzenstein, L. Worschech, M. Kamp, S. Höfling, and A. Forchel. Single site-controlled In(Ga)As/GaAs quantum dots: growth, properties and device integration. *Nanotechnology*, 20:434012, 2009.

[83] W. Ostwald. *Z. Phys. Chem.*, 34:495, 1900.

[84] I. M. Lifshitz and V. V. Slezov. *J. Chem. Solids*, 19:35, 1959.

[85] C. Wagner. *Z. Elektrochem.*, 65:581, 1961.

[86] R. D. Vengrenovitch. *Acta metall.*, 65:1079, 1982.

[87] R. D. Vengrenovitch, Yu. V. Gudyma, and S. V. Yarema. *Semiconductors*, 35:1378, 2001.

[88] T. J. Krzyzewski and T. S. Jones. Ripening and annealing effects in inas/gaas(001) quantum dot formation. *J. Appl. Phys.*, 96:668, 2004.

[89] D. Z. Hu, D. M. Schaadt, and K. H. Ploog. Stress development during annealing of self-assembled InAs/GaAs quantum dots measured in situ with a cantilever beam setup. *Journal of Crystal Growth*, 293(2):546–549, 2006.

[90] M. Rosini, M. C. Righi, P. Kratzer, and R. Magri. Indium surface diffusion on InAs (2×4) reconstructed wetting layers on GaAs(001). *Phys. Rev. B*, 79:075302, 2009.

[91] M. Schmidbauer, Zh. M. Wang, Yu. I. Mazur, P. M. Lytvyn, G.J. Salamo, D. Grigoriev, P. Schäfer, R. Köhler, and M. Hanke. Initial stages of chain formation in a single layer of (In,Ga)As quantum dots grown on GaAs (100). *Appl. Phys. Lett.*, 91:093110, 2007.

[92] I. Kegel, T. H. Metzger, A. Lorke, J. Peisl, J. Stangl, G. Bauer, J. M. García, and P. M. Petroff. Nanometer-scale resolution of strain and interdiffusion in self-assembled InAs/GaAs quantum dots. *Phys. Rev. Lett.*, 85(8):1694, 2000.

[93] A. Prince, G. V. Raynor, and D. S. Evans. “As-Au-Ga”, Phase Diagrams Ternary Gold Alloys. *Inst. Met., London*, pages 123–132, 1990.

Acknowledgment

This last chapter is dedicated to the people who have contributed to the work on which this thesis is based. I would like to thank

- Prof. Dr. Heinz Kalt for undertaking the task of being the referee of this thesis and his continuous interest in the progress of this work.
- Prof. Dr. Daniel M. Schaadt for giving me the opportunity to work in his group, for his support throughout the whole period of this thesis, for always taking the time when necessary and for managing this project.
- Heinrich Reimer for maintaining the equipment in the laboratory with great care, for supporting with many small tasks and for his help in organizing the work.
- Stefan Kühn, Dr. Erich Müller and Patrice Brenner for their help with electron beam lithography, for preparing TEM lamellas of the site-selective QDs and for helping out with extra shifts at the SEM when needed.
- Dr. Dimitri Litvinov and Dr. habil. Reinhard Schneider for the TEM analysis of the samples.
- Daniel Rülke for his interest in my work, for helpful advice and for PL measurements.
- Prof. Dr. Galina Khitrova, Prof. Dr. Hyatt M. Gibbs and Dr. Joshua Hendrickson for the good collaboration and for AFM and PL measurements.
- Prof. Dr. Gernot Goll for managing the cleanroom facility, for the introduction to the ICP-RIE and for always being cooperative whenever a problem occurred.
- Philipp Ganz for his friendly and open way to interact with people, the very friendly atmosphere in our office, the good times we spent together at conferences and for proofreading this thesis.
- Christian Mayer for being a motivated diploma student, his support with the lab work and for proofreading this thesis.
- current and former members of the MBE group, in particular Dongzhi Hu, Omar Tanirah, Ralf Schuber, Yunhua Wu, Ruoli Wang, Raimund Vöhringer and Yu-Chi Hsu, for the creating a nice and welcoming atmosphere in the group and the good times spent together.
- Philipp Schroth, Dr. Daniil Grigoriev, Sergey Lazarev and Dr. Taras Slobodskyy for the very tiring but interesting experience at ESRF. Thank you for the good times at the synchrotron and in the mountains as well.
- Ferhat Aslan for being a good friend and for his ability to distract me from work once in a while.

- all colleagues at the CFN for organizing and participating in social events.
- the staff of the CFN for managing the CFN, for their continuous support with regard to paperwork and many other issues, for their friendliness and for being always very helpful.
- Martin Will for being a very kind and pleasant flatmate and for proofreading this thesis.
- my parents and my sister for their support, for their love, for always believing in me and for always being there for me.
- you, Isil, for the wonderful times that we spend together, for your love, for your support, for your patience with many things and for being always there for me. Proofreading this thesis was only one of the many things that you did for me. Thank you.